Oxygen incorporation in MAX phases and TiAlN and elastic properties of nanolaminates

Von der Fakultät für Georessourcen und Materialtechnik der Rheinisch -Westfälischen Technischen Hochschule Aachen

zur Erlangung des akademischen Grades eines

Doktors der Ingenieurwissenschaften

genehmigte Dissertation

vorgelegt von

Dipl.-Ing. Moritz to Baben

aus Eutin

Berichter: Univ.-Prof. Jochen M. Schneider, Ph.D.
Prof. Lars Hultman, Ph.D.

Tag der mündlichen Prüfung: 20.12.2012

Materials Chemistry Dissertation

No.: 18 (2013)

Moritz to Baben

Oxygen incorporation in MAX phases and TiAlN and elastic properties of nanolaminates

Shaker Verlag
Aachen 2013

Bibliographic information published by the Deutsche Nationalbibliothek
The Deutsche Nationalbibliothek lists this publication in the Deutsche Nationalbibliografie; detailed bibliographic data are available in the Internet at http://dnb.d-nb.de.

Zugl.: D 82 (Diss. RWTH Aachen University, 2012)

Printed in Germany.

ISBN 978-3-8440-1667-3
ISSN 1861-0595

Shaker Verlag GmbH • P.O. BOX 101818 • D-52018 Aachen
Phone: 0049/2407/9596-0 • Telefax: 0049/2407/9596-9
Internet: www.shaker.de • e-mail: info@shaker.de

Abstract

In this thesis, oxygen incorporation in M_2AlC phases and TiAlN was studied by ab initio calculations and experiments. It was shown that oxygen interstitials are important in both material systems since they are spontaneously formed when oxygen is present. The understanding of the effect of incorporated oxygen on phase stability, elastic properties and bond distribution allows for quantum mechanically guided design of materials with improved oxidation resistance and stability at elevated temperatures.

In the first part, oxygen incorporation in the MAX phases Ti_2AlC, V_2AlC and Cr_2AlC was studied by ab initio calculations. Comparing calculated energies of formation for oxygen incorporation indicates that oxygen substitutes carbon in Ti_2AlC and V_2AlC, but is incorporated interstitially in the Al layer of Cr_2AlC even for carbon deficient Cr_2AlC. To evaluate these predictions, combinatorial DC sputtering was used to deposit thin films with different oxygen concentrations. Two phase-regions of Cr_2AlC and Cr_2Al were investigated in order to study oxygen incorporation in carbon deficient Cr_2AlC. X-ray strain analysis data indicate that the *a* and *c* lattice parameters increase with oxygen content. These trends are in good agreement with the change of lattice parameters predicted by ab initio calculations and therefore corroborate the notion of interstitial oxygen incorporation in Cr_2AlC. A metastable solubility limit for oxygen of 3.5 at.% was determined experimentally. This is the first report on interstitial oxygen in a MAX phase and may be of relevance during the initial stages of oxidation.

In the second part, various point defect configurations were studied by ab initio calculations in terms of formation energies, equilibrium volume and elastic moduli to identify the origin of the experimentally observed nitrogen over- and understoichiometry and as a starting point for studying oxygen incorporation in TiAlN

thin films. From formation energies and comparison to existing experimental equilibrium volume and elasticity data, it was shown that nitrogen vacancies and metal vacancies are responsible for nitrogen understoichiometry and overstoichiometry, respectively. Irrespective of the type of vacancies, the bulk modulus is decreased by approximately 7 % as the nitrogen concentration is increased or decreased by 3 at.%.

The third part deals with the impact of oxygen additions on phase stability and elastic properties of TiAlN. Based on ab initio calculations, it was shown that fcc-$Ti_{0.5}Al_{0.5}N$ and fcc-$Ti_{0.5}Al_{0.5}O$ show a negative energy of mixing. The lattice parameter of $Ti_{0.5}Al_{0.5}N_{1-x}O_x$ increases with increasing x while the bulk modulus decreases by up to 35 %. The reason is the metallic bonding character which increases at the expense of the covalent character with increasing oxygen content. It was shown that the incorporation of oxygen in $Ti_{0.5}Al_{0.5}N_{1-x}O_x$ on interstitial sites is energetically favourable. This can be understood based on the compensation of metallic bonding as the population of metal-oxygen bonds that are similar to α-Al_2O_3 and rutile-TiO_2 is increased. Based on the oxygen incorporation induced stability increase of $Ti_{0.5}Al_{0.5}N_{1-x}O_{x+y}$, a new design concept for transition metal oxynitride based hard coatings was developed.

In order to test the theoretical predictions made regarding the non metal substitutions, a fast synthesis method was developed where reactive gas gradients are employed during combinatorial thin film deposition. This method is evaluated in the fourth part of this thesis. N_2 and O_2 partial pressure gradients over the target surface were used to deposit TiN_x, TiO_y, $TiAlN_x$ and $TiAlN_xO_y$ thin films with varying x and y in a single deposition. It is shown that reactive gas gradients can be used to synthesize films with lateral composition gradients and that such films are useful to study their composition-structure-properties relationship. A new amorphous or nanocrystalline

hard TiO_y ($y < 1$) phase is reported as well as an increase of the (200) lattice spacing of $TiAlN_xO_y$ that may indicate interstitial oxygen incorporation.

Additionally, in the fifth part, an extension to the rule of mixture (ROM) to the sub unit-cell level is reported, deriving how bulk moduli of single phases with layered crystal structure and solid solutions can be reliably estimated. This method was tested for MAX phases and $M_nAl_4C_{3+n}$ phases. Based on ROM, DFT combinatorics was developed, reducing calculation time for elastic properties by some orders of magnitude. This is a significant step towards knowledge-based materials design since elastic properties can be predicted based on an efficient high throughput methodology.

Zusammenfassung

Im Rahmen dieser Arbeit wurde durch ab initio-Berechnungen und Experimente ein fundamentales Verständnis der Sauerstoffeinlagerung in M_2AlC Phasen und TiAlN entwickelt. Es wurde gezeigt, dass interstitieller Sauerstoff eine wichtige Rolle in beiden Materialsystemen spielt, da dieser spontan gebildet wird, wenn Sauerstoff anwesend ist. Das Verständnis des Effektes von Sauerstoff auf Phasenstabilität, elastische Eigenschaften und Bindungsverteilung erlaubt quantenmechanisch geführtes Materialdesign von Materialien mit erhöhtem Oxidationswiderstand und Stabilität bei erhöhten Temperaturen.

Im ersten Teil wurde Sauerstoffeinlagerung in den MAX Phasen Ti_2AlC, V_2AlC und Cr_2AlC mit Hilfe von ab initio-Berechnungen untersucht. Der Vergleich von berechneten Bildungsenergien für Sauerstoffeinlagerung deutet darauf hin, dass Sauerstoff Kohlenstoff in Ti_2AlC und V_2AlC ersetzt, jedoch interstitiell in die Aluminium Lage von Cr_2AlC eingebaut wird, selbst für kohlenstoffarmes Cr_2AlC. Um diese Vorhersagen zu überprüfen, wurden mittels kombinatorischem DC-Sputtern Dünnschichten mit verschiedenen Sauerstoffgehalten hergestellt. Um die Sauerstoffeinlagerung in kohlenstoffarmes Cr_2AlC zu untersuchen, wurden Zweiphasen-Regionen mit Cr_2AlC und Cr_2Al untersucht. Daten aus röntgenbasierter Dehnungsanalyse deuten darauf hin, dass die *a* und *c* Gitterparameter mit dem Sauerstoffgehalt zunehmen. Diese Tendenzen stimmen gut mit der von ab initio-Berechnungen vorhergesagten Änderung überein und bekräftigen somit die These von interstitiellem Sauerstoffeinbau in Cr_2AlC. Eine metastabile Löslichkeit von 3,5 at.% Sauerstoff wurde experimentell bestimmt. Dies ist der erste Bericht über interstitiellen Sauerstoff in einer MAX Phase und könnte für die Anfangsphase der Oxidation relevant sein.

Im zweiten Teil wurden verschiedene Punktdefektkonfigurationen bezüglich Bildungsenergien, Gleichgewichtsvolumen und E-Modul mittels ab initio-Berechnungen untersucht, um den Ursprung der experimentell beobachteten Stickstoff-Unter- und Überstoichiometrie in TiAlN Dünnschichten zu bestimmen. Diese Studie diente auch als Ausgangspunkt für die Untersuchung von Sauerstoffeinbau in TiAlN. Basierend auf den Bildungsenergien und auf einem Vergleich mit existierenden experimentellen Gleichgewichts- und Elastizitätsdaten wurde gezeigt, dass Stickstoff-Leerstellen und Metall-Leerstellen für die Stickstoff-Unter- und Überstoichiometrie verantwortlich sind. Unabhängig von der Art der Leerstelle wird der Kompressionsmodul um etwa 7 % verringert, wenn der Sauerstoffgehalt um 3 at.% erhöht oder verringert wird.

Der dritte Teil beschäftigt sich mit dem Einfluss von Sauerstoffeinlagerung auf Phasenstabilität und elastische Eigenschaften von TiAlN. Mit ab initio-Berechnungen wird gezeigt, dass fcc-$Ti_{0.5}Al_{0.5}N$ und fcc-$Ti_{0.5}Al_{0.5}O$ eine negative Mischungsenergie aufweisen. Der Gitterparameter von $Ti_{0.5}Al_{0.5}N_{1-x}O_x$ nimmt mit steigendem x zu, während der Kompressionsmodul um bis zu 35 % abnimmt. Der Grund dafür ist der metallische Bindungscharakter, der auf Kosten des kovalenten Charakters mit steigendem Sauerstoffgehalt zunimmt. Es wurde gezeigt, dass interstitieller Sauerstoffeinbau in $Ti_{0.5}Al_{0.5}N_{1-x}O_x$ energetisch begünstigt ist. Dies kann aufgrund der Kompensation der metallischen Bindung verstanden werden, wenn der Anteil an Metall-Sauerstoff-Bindungen zunimmt, die denen in α-Al_2O_3 und Rutil-TiO_2 ähnlich sind. Basierend auf der durch Sauerstoff hervorgerufenen Stabilitätserhöhung von $Ti_{0.5}Al_{0.5}N_{1-x}O_{x+y}$ wird ein neues Designkonzept für Übergangsmetall-Oxynitride entwickelt.

Um die Vorhersagen aus den theoretischen Berechnungen bezüglich der Nichtmetall-Substitution zu überprüfen, wurde eine schnelle Synthesemethode

entwickelt, wurden Reaktivgasgradienten benutzt, um kombinatorische Dünnschichtabscheidungen durchzuführen. Diese Methode wird im vierten Teil dieser Dissertation bewertet. N_2 und O_2 Partialdruckgradienten entlang der Targetoberfläche wurden benutzt, um TiN_x, TiO_y, $TiAlN_x$ und $TiAlN_xO_y$ Dünnschichten mit variierendem x und y in einer einzigen Beschichtung abzuscheiden. Es wird gezeigt, dass Reaktivgasgradienten benutzt werden können, um Schichten mit lateralem Zusammensetzungsgradienten herzustellen und das diese Schichten benutzt werden können, um die Zusammensetzung-Struktur-Eigenschaften-Korrelation zu untersuchen. Die Existenz einer neuen amorphen oder nanokristallinen harten TiO_y-Phase ($y < 1$) wird berichtet sowie eine Vergrößerung des (200) Gitterabstandes von $TiAlN_xO_y$, welche auf den interstitiellen Einbau von Sauerstoff hinweisen könnte.

Zusätzlich wird im fünften Teil eine Erweiterung der Mischungsregel auf eine Ebene kleiner als die Einheitszelle berichtet, indem gezeigt wird, wie der Kompressionsmodul von Phasen mit geschichteter Kristallstruktur und von Mischungen zuverlässig abgeschätzt werden kann. Diese Methode wurde für MAX-Phasen und $M_nAl_4C_{3+n}$ Phasen getestet. Basierend auf der Mischungsregel wurde Dichtefunktionaltheorie-Kombinatork entwickelt, wodurch die Berechnungszeit für elastische Eigenschaften um mehrere Größenordnungen reduziert wird. Dies ist ein wichtiger Schritt in Richtung wissensbasiertes Werkstoffdesign, da elastische Eigenschaften durch eine Methodologie mit großem Durchsatz vorhergesagt werden können.

Preface

The following papers contributed to this thesis:

Paper I

Extending the rule of mixture to the sub unit-cell level

M. to Baben, D. Music, J. Emmerlich and J. M. Schneider

Scripta Materialia 65 (2011) 735–738

Paper II

Origin of the nitrogen over- and understoichiometry in $Ti_{0.5}Al_{0.5}N$ thin films

M. to Baben, L. Raumann, D. Music and J. M. Schneider

Journal of Physics: Condensed Matter 24 (2012) 155401

Paper III

Oxygen incorporation in M_2AlC (M = Ti, V, Cr)

M. to Baben, L. Shang, J. Emmerlich and J. M. Schneider

Acta Materialia 60 (2012) 4810–4818

Paper IV

Phase stability and elastic properties of titanium aluminium oxynitride studied by ab initio calculations

M. to Baben, L. Raumann and J. M. Schneider

accepted in: Journal of Physics D: Applied Physics

The calculations and theory development in paper I were done by MtB with the help of DM and JE. The calculations in paper II were done by LR and MtB. The samples for paper III were deposited by LS and MtB. LS did the strain analysis with the help of JE and MtB as well as the measurement of compositions. The calculations were done by MtB. The calculations in paper IV were done by LR and MtB. For all papers, goals were discussed and strategies were developed with JMS. All co-authors took part in discussion of the results and editing the manuscripts.

Publications related to the topics of this thesis:

Paper V

Intercalation of Al into MC (M= Ti, V, Cr)

D. Music, H. Koelpin, M. to Baben and J.M. Schneider

Journal of the European Ceramic Society 29 (2009) 2885–2891.

Paper VI

Experimental and Computational Study on the Phase Stability of Al-containing Cubic Transition Metal Nitrides

F. Rovere, D. Music, S. Ershov, M. to Baben, H.G. Fuss, P.H. Mayrhofer and J.M. Schneider

Journal of Physics D: Applied Physics 43 (2010) 035302

Paper VII

Fabrication and oxidation behavior of Cr_2AlC coating on Ti6242 alloy

Q.M. Wang, A. Flores Renteria, O. Schroeter, R. Mykhaylonka, C. Leyens, W. Garkas, M. to Baben

Surface & Coatings Technology 204 (2010) 2343–2352.

Paper VIII

On the phase formation of sputtered hafnium oxide and oxynitride films

K. Sarakinos, D. Music, S. Mráz, M. to Baben, K. Jiang, F. Nahif, A. Braun, C. Zilkens, S. Konstantinidis, F. Renaux, D. Cossement, F. Munnik and J.M. Schneider

Journal of Applied Physics 108 (2010) 014904.

Paper IX

Oxidation of Cr_2AlC coatings in the temperature range of 1230 to 1410 °C

D. E. Hajas, M. to Baben, B. Hallstedt, R. Iskandar, J. Mayer and J.M. Schneider

Surface & Coatings Technology 206 (2011) 591.

Paper X

Crystallization kinetics of amorphous Cr_2AlC thin films

A. Abdulkadhim, M. to Baben, T. Takahashi, V. Schnabel, M. Hans, C. Polzer, P. Polcik and J.M. Schneider

Surface & Coatings Technology 206 (2011) 599.

Paper XI

Crystallization kinetics of V_2AlC

A. Abdulkadhim, M. to Baben, V. Schnabel, M. Hans, N. Thieme, C. Polzer, P. Polcik and J.M. Schneider

Thin Solid Films 520 (2012) 1930.

Paper XII

Polypropylene-MAlN (M=Ti, Cr) interface interactions

D. Music, D. Lange, L. Raumann, M. to Baben, F. von Fragstein and J.M. Schneider

Surface Science 606 (2012) 986.

Paper XIII

Growth and thermal stability of $(V,Al)_2C_x$ thin films

A. Abdulkadhim, R. Iskandar, M. to Baben, T. Takahashi, J. Zhang, J. Emmerlich, J. Mayer, C. Polzer, P. Polcik and J.M. Schneider

Journal of Materials Research 27 (2012) 2511.

Paper XIV

Surface chemistry of TiAlN and TiAlNO coatings deposited by means of High Power Pulsed Magnetron Sputtering

C. Gnoth, C. Kunze, M. Hans, M. to Baben, J. Emmerlich, J. M. Schneider, G. Grundmeier

accepted in: Journal of Physics D: Applied Physics

Other publication:

Paper XV

Textured VN coatings with Ag_3VO_4 solid lubricant reservoirs

B. Luster, D. Stone, D. P. Singh, M. to Baben, J.M. Schneider, K. Polychronopoulou, C. Rebholz, P. Kohli and S. M. Aouadi

Surface & Coatings Technology 206 (2011) 1932.

Acknowledgements

Ich danke an erster Stelle meinem Betreuer Prof. Jochen Schneider. Vielen Dank für Deine Unterstützung und Dein Vertrauen. Ich habe in den fünf Jahren der Promotion viel gelernt und viel mit Dir diskutieren dürfen. Du hast mir viele Freiheiten gegeben und Dich dafür interessiert, was aus diesen Freiheiten entsteht, weshalb mir die Zeit am MCh sehr viel Spaß gemacht hat.

An zweiter Stelle möchte ich dem Zweitgutachter Prof. Lars Hultman danken. Tack så mycket! I am honoured that you make the way to Aachen for my defence talk!

Der nächste Dank geht an die wise guys, die mich während der Promotion begleitet haben, besonders an Jens, Denis, Stano und Tetsuya für Unterstützung, Diskussionen und die ständige Bereitschaft zu helfen!

Auch möchte ich mich bei meinen Studenten bedanken (in order of appearance): Danke Sergey, Hannes, Ben, Leo, Lin, Marcus, Christian, Ina, Volker und Fabian!

Den „Werkstätten“ in Personen von Herrn Horbach, Manfred, Bernd, Stefan und Herrn Bomke möchte ich für die hervorragende Unterstützung bei allen Umbauten danken! Besonderer Dank gilt hier Ihnen, Herr Horbach, dafür, dass Sie jede augenscheinlich verrückte Idee erstmal als Idee und nicht als verrückt ansehen und immer hervorragende Änderungsvorschläge haben!

Danach folgt mein Dank an alle anderen MCh’ler, die zu viele sind, um hier genannt zu werden. Vielen Dank für die wunderbare Atmosphäre, das gemeinsame Erkämpfen der Institutsolympiade-Trophäe und des 20. Platzes im Hallenfußballcup, die Mittagspausen und die vielen Diskussionen!

Sport nach der Mensa ist eine wunderbare Sache, weshalb ich mich bei den IMM’lern für die Meetings am Kickertisch bedanken möchte! Allen (un)regelmäßigen Mitstreitern auf dem echten Fußballplatz möchte ich ebenso danken für jedes Mal, dass wir die sechs Leute in der doodle-Liste vervollständigen konnten!

Im Leben neben dem MCh möchte ich vor allem „den Metallurgen“ danken: Vielen Dank an Bastian, Matze, Marko, Lutz und Bum-Ki und natürlich ein riesiges Dankeschön an Thiemo für die gemeinsame Zeit vom Mathe-Vorkurs in 2003 bis Heute und alle Unterstützung!

Ein großes Dankeschön möchte ich hier auch an meine Familie aussprechen, die mir immer Rückhalt gibt. Hier möchte ich aber einmal darauf hinweisen, dass Aussagen wie „Arbeit ist nicht das ganze Leben“ (dieser Spruch einer Postkarte vom ersten Arbeitstag am 15.11.2007 hat mich durch vier Büros begleitet) und „Gibst Du am Freitag endlich Deine Dissertation ab?“ (diese Frage hat mich mindestens seit dem 15.11.2009 begleitet) nicht kompatibel sind! Vielen Dank trotzdem für alle Unterstützung!

Abschließend bleibt es mir, den größten Dank an meine Frau Anja zu richten. Vielen Dank für Deine Unterstützung, Deine Lebensfreude, die Du mit mir teilst, und Deine Liebe! Ich bin darüber glücklich, dass Du mir immer wieder die richtigen Prioritäten zeigst!

Table of Contents

1 Introduction

Advances in theory of electronic structure calculation and computational power (during this thesis, the calculation power available at RWTH Aachen University increased from 1 TFlops in 2007 to 300 TFlops in 2011 [1]) enabled quantum mechanically guided materials design as a new method to develop materials solutions. Thus, a research strategy based purely on the trial-and-error approach is no longer the only option for discovery and optimization of materials. To enhance a specific property of a material, the addition of several elements can be studied by density functional theory (DFT) calculations and the most promising composition(s) can be synthesized experimentally. At Materials Chemistry, materials with enhanced phase stability [2-5], elastic properties [5-9] and most recently transport properties [10, 11] are designed. The design strategy is guided by quantum mechanical data. The phase stability can be studied by comparing the calculated energies of a compound with its constituents in the ground state (energy of formation) or even with other compounds. While trends in stability may be predicted as well as e.g. the energy of mixing or point defect energies, it should be noted that a purely theoretical prediction of a phase diagram or a chemical reaction is virtually impossible as this would include the calculation of all possible compositions in all crystal structures or all possible transient and metastable states, respectively. Elastic properties like bulk moduli and elastic constants can be obtained by tracing energy changes when deformations to the ground-state are applied.

As a first step in the design process of materials for cutting tools [2, 5], phase change memory devices [3], dielectrics [4], high strength metallic glasses [6], materials with (an)isotropic compressibility [7], steel with tuned deformation mechanisms [8, 9], mixed ionic and electronic conductors [10] and thermoelectrics [11] phases with

different chemical compositions but same crystal structure [5-7] or solid solutions [2-4, 8-11] were quantum mechanically described. In all of these works metals were substituted by other metal atoms, with the exception of [3] where N interstitials in $Ge_2Sb_2Te_5$ were studied and [4] where oxygen in HfO_2 was substituted by vacancies or nitrogen.

It is a well known fact that doping in oxides can lead to formation of vacancies, e.g. in the case of Y doping in ZrO_2, formation of oxygen vacancies is observed due to the lower valency of Y leading to ionic conductivity [12]. Similarly, it may be expected that oxygen doping in nitrides or carbides also leads to defects, i.e. metal vacancies or interstitial oxygen. While the formation of defects is often used speculatively to explain measured deviations from stoichiometry [13-15], fundamental studies proving or disproving the formation of defects were not reported. Therefore, the goal of this thesis is to contribute towards understanding how solid solutions of nitrides and carbides with oxides, i.e. the variation on the non-metal sublattice, affect energetics. Based on this understanding, design concepts for materials with improved oxidation resistance and stability at elevated temperatures are proposed.

The outline of the thesis is as follows: it is divided into two parts, where the first deals mostly with phase stability and the second with elastic properties. In chapters 3.1 to 3.3, phase stability of $M_2AlC_{1-x}O_x$ (M = Ti, V, Cr) and $Ti_{0.5}Al_{0.5}N_{1-x}O_y$ is studied. It is shown that oxygen interstitials play an important role in both material systems: While oxygen is incorporated on carbon vacancy sites in $M_2AlC_{1-x}O_x$ for M = Ti and V, interstitial oxygen incorporation in the Al layer is more stable for M = Cr, even in the presence of carbon vacancies. This result was unexpected especially when considering that the size of the interstitial site in the Al layer is smallest for Cr_2AlC. Hence, this theoretical result was validated experimentally utilizing the combinatorial approach [16]. A slight increase in *a* lattice parameter of the as deposited Cr-Al-C-O

films was observed with increasing oxygen content. This can be understood by considering the lattice expansion caused by oxygen that is incorporated interstitially. As oxygen incorporation on a carbon site results in a decrease of the *a* lattice parameter due to the smaller atomic radius of oxygen compared to carbon, this scenario is not compatible with the experimental data. Interstitial oxygen incorporation may be of relevance during the initial stages of oxidation of Cr_2AlC as it leads to formation of Al-O bonds which may act as nucleation sites for Al_2O_3. On the other hand, oxygen substituting carbon in Ti_2AlC and V_2AlC leads to Ti-O and V-O bonds, which may act as nucleation sites for titanium and vanadium oxides that are observed experimentally [17-21].

As a starting point for the oxynitride $TiAlN_{1-x}O_y$, nitrogen off-stoichiometry in TiAlN was studied by DFT calculations. Studying several types of defects to compensate for the nitrogen off-stoichiometry, it is shown that nitrogen and metal vacancies are energetically most favored in nitrogen under- and overstoichiometric TiAlN, respectively. Comparing calculated lattice parameters and elastic moduli to published experimental results for understoichiometric TiAlN corroborates the notion of nitrogen vacancies.

Keeping in mind that the most stable defects in off-stoichiometric TiAlN are vacancies, the impact of oxygen additions on phase stability and elastic properties of TiAlN was studied by DFT calculations. Fcc-$Ti_{0.5}Al_{0.5}N$ and hypothetical fcc-$Ti_{0.5}Al_{0.5}O$ show a negative energy of mixing. The lattice parameter of $Ti_{0.5}Al_{0.5}N_{1-x}O_x$ increases with increasing x while the bulk modulus decreases by 35%. The reason for this is the metallic bonding character which increases on the expense of covalent bonds with increasing oxygen content. In contrast to $Ti_{0.5}Al_{0.5}N$ it has been shown that the incorporation of oxygen in $Ti_{0.5}Al_{0.5}N_{1-x}O_x$ on interstitial sites is energetically favourable. This can be understood based on the compensation of metallic bonding

as the population of metal-oxygen bonds that are similar to α-Al_2O_3 and rutile-TiO_2 is increased. Based on the oxygen incorporation induced stability increase of $Ti_{0.5}Al_{0.5}N_{1-x}O_{x+y}$, a new design concept for transition metal oxynitride based hard coatings is developed.

In chapter 3.4, reactive gas gradients were used to deposit TiN_x, TiO_y, $TiAlN_x$ and $TiAlN_xO_y$ thin films with varying x and y in a single deposition. Using energy dispersive X-ray spectroscopy (EDX), X-ray diffraction (XRD) and Nanoindentation it was shown that reactive gas gradients can be used to synthesize films with lateral composition gradients and to study their composition-structure-properties relationship. A new amorphous or nanocrystalline hard TiO_y ($y < 1$) phase is reported as well as the observed increase of the (200) lattice spacing of $TiAlN_xO_y$ that may indicate interstitial oxygen incorporation.

In chapter 3.5, the rule of mixture has been extended to the sub unit-cell level for the estimation of bulk moduli. It is shown how the theoretical bulk modulus of a single phase with layered crystal structure is reliably estimated from calculated bulk moduli data of the constituents adopting the symmetry within the individual layers of the layered structure. This method was tested for the example of 16 MAX phases, 3 $M_nAl_4C_{3+n}$ phases and $KAg(CN)_2$ and excellent agreement with existing *ab initio* data is observed. Thus, a high throughput methodology based on a combination of DFT and combinatorial materials science was developed which allows for prediction of the elastic properties of “sub unit-cell” composite materials: a database containing a variety of hypothetical phases which are building blocks of the layered structure was created. Suitable combinations of these building blocks constitute the “sub unit-cell composite”, reducing calculation time by some orders of magnitude. This work is a significant step towards knowledge-based materials design since the elastic

properties of “sub unit-cell composite” materials can be predicted based on an efficient high throughput methodology.

Furthermore, this approach is evaluated for all elastic constants of $M_{n+1}AlC_n$ (M = Ti, V, Cr) and it is shown that C_{11} and C_{33} can be estimated based on the extended rule of mixture, while the other constants are prone to larger deviations. Finally, the rule of mixture is used to describe MAX phase solutions and titanium aluminum (oxy-)nitride solutions: varying the Ti:Al ratio ($Ti_{1-x}Al_xN$), the N:vacancy ratio ($Ti_{0.5}Al_{0.5}N_{1-x}$) and the O:N ratio ($Ti_{0.5}Al_{0.5}N_{1-x}O_x$). Based on the good agreement between the extended rule of mixture values and the bulk moduli directly calculated for the solutions, it is evident that the extended rule of mixture can also be used for knowledge based design of solid solutions, even if the boundary phases are hypothetical and extremely different in bonding and, hence, stiffness.

2 Methods

2.1 Ab initio calculations

In order to determine the electronic structure of a solid at 0 K, the time-independent Schrödinger equation (eq. 1) has to be solved.

(1) $$H\Psi = E\Psi$$

For a solid consisting of N electrons and M nuclei with atomic number Z, there are energetic contributions from kinetic energy of the electrons as well as electron-electron, electron-nuclei and nuclei-nuclei interactions and the Hamiltonian in eq. 1 has the following form:

(2) $$H = -\sum_{i=1}^{N}\frac{1}{2}\nabla_i^2 - \sum_{i=1}^{N}\sum_{A=1}^{M}\frac{Z_A}{|R_A - r_i|} + \sum_{i=1}^{N-1}\sum_{j>1}^{N}\frac{1}{|r_i - r_j|} + \sum_{A=1}^{M}\sum_{B>A}^{M}\frac{Z_A Z_B}{|R_A - R_B|}$$

To give an example: for TiN (where total number of electrons is 29), the electron-electron interaction sum consists of 406 terms all of which depend on each other. This shows that solving the Schrödinger equation for all electrons in a system significantly more complicated than a hydrogen atom is virtually impossible.

A different approach to obtain the electronic structure is based on the Thomas-Fermi method [22, 23], where the electron density is studied rather than individual electrons. However, this approach could only be used for simple metallic systems until Hohenberg and Kohn have shown that the ground state is a unique functional of the electron density and that the ground state electron density minimizes the electronic energy of a system with given external (atom core) potential.

Density functional theory calculations [24, 25] have been done using the Vienna Ab-initio Simulation Package (VASP). Generalized-gradient approximation (GGA PB91) [26] based projector augmented wave potentials [27] were used, as well as a Monkhorst-Pack scheme [28] for reciprocal-space integration and the tetrahedron

method with Blöchl-corrections for the total energy [29]. The electronic relaxation convergence was set to 0.01 meV and the energy cutoff to 500 eV. K-point grids and supercell sizes used are given in Table 1.

chapter	material system	supercell size	K-point grid	structural optimization
3.1	MAX phases + oxygen	2x2x2	5x5x3	every volume
3.2	$TiAlN_x$	2x2x2	6x6x6	every volume
3.3	$TiAlN_xO_y$	2x2x2	6x6x6	every volume
3.4	MAX phases, constituents	1x1x1	7x7x7	equilibrium volume
3.4	KAg(CN)2	1x1x1	5x5x5	equilibrium volume

Table 1: supercell sizes, K-point grids and method for structural optimization used in this thesis.

As can be seen in Table 1, structural optimization was done iteratively for all calculations presented in chapter 3.4. This means that structures were relaxed with respect to internal atomic positions, lattice parameter *a* and hexagonal aspect ratio *c/a* subsequently and the steps were repeated until convergence.

For the calculations in chapter 3.1, structural optimization was done by a least square fitting of the total energy obtained from at least nine calculations with three different *a* and *c/a* values with the following polynomial function:

(3) $$E(a,c) = x_1 \cdot \mathrm{a}^2 + x_2 \cdot \mathrm{c}^2 + x_3 \cdot \mathrm{a} \cdot \mathrm{c} + x_4 \cdot \mathrm{a} + x_5 \cdot \mathrm{c} + x_6 .$$

For these calculations, ions were allowed to relax. Thus, both lattice parameters and the internal free parameter were allowed to change simultaneously and the energetic minimum could be obtained, leading to the highest accuracy.

To calculate the equilibrium volumes in the TiAlNO system and to obtain the bulk moduli in chapter 3.4, energy-volume curves were fitted using the Birch-Murnaghan equation of states [30].

The energies of formation were calculated with respect to the elements. The total energy and lattice parameters obtained are given in Table 2.

element	structure	a [Å]	c/a	E_{total} [eV/atom]
Al	fcc	4.039	-----	-3.713
C	diamond	3.575	-----	-9.096
Cr	bcc	2.851	-----	-9.451
Hf	hcp	3.194	1.592	-9.824
Mo	bcc	3.174	-----	-10.770
N	N_2 molecule	10	-----	-8.336
Nb	bcc	3.297	-----	-10.251
O	O_2 molecule	10	-----	-4.361
Sc	hcp	3.300	1.574	-6.226
Si	diamond	5.470	-----	-5.424
Ta	bcc	3.313	-----	-11.767
Ti	hcp	2.936	1.589	-7.793
V	bcc	2.992	-----	-8.990
W	bcc	3.194	-----	-12.740
Y	hcp	3.652	1.552	-6.379
Zr	hcp	3.244	1.600	-8.421

Table 2: calculated data for pure reference elements.

The effective charge of each atom was obtained using the Bader analysis as implemented in the Henkelman code [31, 32]. This algorithm allows for decomposition of the charge density into atomic regions by dividing space along paths with minimum electron density. It is based on a steepest ascent path along grid points to allocate them to local charge density maxima [31]. The FFT grid density was tested for convergence.

2.1.1 MAX phases

To study oxygen incorporation, the energies of formation of carbon vacancies, oxygen interstitials and oxygen substitutions were calculated as shown in equations 4 to 6, respectively:

(4) $$\Delta E_{f,C-vac} = {}^{1}\!/_{x}(E_{M_2AlC_{1-x}} - E_{M_2AlC} + x \cdot E_C)$$

(5) $$\Delta E_{f,O-\mathrm{int}} = {}^{1}\!/_{x}(E_{M_2AlCO_x} - E_{M_2AlC} - x \cdot E_O)$$

(6) $$\Delta E_{f,C->O} = {}^{1}\!/_{x}(E_{M_2AlC_{1-x}O_x} - E_{M_2AlC} + x \cdot E_C - x \cdot E_O)$$

For carbon vacancies, oxygen substitutions on carbon sites and oxygen interstitials in an Al layer with same x,y-coordinates as M atoms in adjacent layers [33], supercell configurations with one and two defects per supercell were considered for Ti_2AlC, V_2AlC and Cr_2AlC. For Cr_2AlC, additionally, oxygen incorporation on other interstitial sites which were also tested by Liao et al. in Ti_2AlC [33], i.e. the center of an octahedron with Cr and Al on the vertices and in an Al layer with same x,y-coordinates as C atoms, were studied in the presence of carbon vacancies. The energy of the latter configurations were higher compared to oxygen substitution on carbon sites and oxygen interstitials in the Al layer with the same x,y-coordinates as Cr atoms in adjacent layers and are therefore not discussed further.

Recently, Ramzan et al. and Du et al. argued that electron correlation effects lead to an underestimation by 1.7 % of the volume of Cr_2AlC calculated with GGA potentials and proposed the usage of Hubbard corrections with the DFT+U method [34, 35]. Here, *U* is a measure of the energy by which filled d-states are shifted towards lower energies [36]. It should be noted that U is an empirical constant [25] used to overcome differences between DFT calculations and experiments. In the first implementation in the VASP program, for example, U was varied between 0 and 8 eV in order to fit experimental lattice parameter, band gap, magnetic moment and bulk modulus data of NiO. As experimental data is not existing for Cr_2AlC despite of lattice parameters and bulk moduli and for the latter large differences exist between different reports (see [37] and references therein), a DFT+U approach can only be based on a comparison with experimental lattice parameters. For Cr_2AlC, Ramzan et al. tested different magnetic ordering but considered only two values for U and concluded that Cr_2AlC is a ferromagnet and that U = 1 eV is a proper value to describe the electronic structure of Cr_2AlC [35]. Du et al., however, considered six different values for U between 0 and 2.5 assuming only antiferromagnetic ordering and determined U to be 2 eV [34]. It is confusing to note that Ramzan et al. reported a unit cell volume which is 13 % larger than the experimentally determined volume with U = 2 eV and antiferromagnetic ordering [35]. Due to the non-conclusive results U was not included as a fitting parameter in calculations here. Furthermore, it is suggested that the unit cell volume alone is not sufficient information to determine the empirical constant U. Based on the lower total energy of paramagnetic Cr_2AlC and the comparatively small local magnetic moment of Cr in ferromagnetic and antiferromagnetic states of Cr_2AlC [38] the paramagnetic state is used here.

2.1.2 TiAlN and TiAlNO

By fitting the energy-volume curve using the Birch-Murnaghan equation of states [30], equilibrium volume, bulk modulus B and its pressure derivative B' were obtained. In order to determine the trend in elastic moduli when off-stoichiometry in $TiAlN_x$ is considered, the Poisson's ratio v was estimated from B' according to v = 2/3-5/(3B') [39]. For $Ti_{0.5}Al_{0.5}N$ the elastic constants were calculated from distortions according to reference [40] and a value of 0.214 was obtained which is different from the value obtained from B', which is 0.270. To avoid calculations of all elastic constants, the Poisson's ratios were only obtained from B' and corrected by the factor 0.214/0.270 to be consistent with the more accurate calculation of elastic constants of $Ti_{0.5}Al_{0.5}N$.

For all calculations in the TiAlN and TiAlNO systems, the 2x2x2 supercell containing 64 atoms as proposed by Mayrhofer et al. [41] was adopted. This supercell (named C#3 in the original paper) minimizes the number of Ti-Al bonds and therefore shows highest stability [41]. Using this description, every nitrogen site is equivalent in terms of its metal nearest neighbors. $Ti_{0.5}Al_{0.5}N_{1-x}$ and $Ti_{0.5}Al_{0.5}N_{1-x}O_x$ cells were constructed using special quasirandom structures (SQS) [42] for the distribution of nitrogen and vacancies on the non-metal sublattice. For this, the Warren-Cowley short-range order parameter [43] within three coordination shells was used in order to account for randomness in the non-metal sublattice as implemented in the locally self-consistent Green's function software package [44, 45]. The energy of formation E_f was calculated by the following formula:

$$E_f = \frac{1}{\sum n_i}\left(E_{tot} - \sum n_i \cdot E_i\right) \quad (7)$$

where E_{tot} is the total energy of the compound, n_i is the number of atoms of species i in the compound and E_i is the total energy of the species in its reference state.

Methods

The energy needed to form a vacancy was calculated as shown in the following formula for a Ti vacancy in $Ti_{0.5}Al_{0.5}N$:

(8) $$E_f^{Ti-vac} = E_{tot}(Ti_{15}Al_{16}N_{32}) + E_{Ti} - E_{tot}(Ti_{16}Al_{16}N_{32}).$$

The energy needed to incorporate an atom on an interstitial site is calculated as illustrated for interstitial oxygen in $Ti_{0.5}Al_{0.5}N$ in the following formula:

(9) $$E_f^{O-\mathrm{int}} = E_{tot}(Ti_{16}Al_{16}N_{32}O_1^{\mathrm{int}}) - E_{tot}(Ti_{16}Al_{16}N_{32}) - \frac{1}{2}E_{O_2}.$$

The energy of mixing in the $Ti_{0.5}Al_{0.5}N_{1-x}O_x$ system is calculated by evaluating the energy difference between $Ti_{0.5}Al_{0.5}N_{1-x}O_x$ and the unmixed components $Ti_{0.5}Al_{0.5}N$ and $Ti_{0.5}Al_{0.5}O$:

(10) $$\Delta E_{mix} = E_f(Ti_{0.5}Al_{0.5}N_{1-x}O_x) - (1-x)E_f(Ti_{0.5}Al_{0.5}N) - xE_f(Ti_{0.5}Al_{0.5}O)$$

It should be kept in mind that the $Ti_{0.5}Al_{0.5}N$ phase itself is metastable as fcc-TiN and wurtzite-AlN are the thermodynamically stable phases. Therefore, these calculations will probably not show which phase forms during vapor phase condensation but it will allow comparing different defect energies and may serve as guide for future experiments in the $Ti_{0.5}Al_{0.5}N_x$ and $Ti_{0.5}Al_{0.5}N_xO_y$ systems.

2.2 Experimental methods

To study oxygen incorporation in Cr_2AlC, combinatorial thin film deposition [16] of Cr, Al and C by DC magnetron sputtering was employed. The oxygen partial pressure was varied in three depositions and each sample was characterized by EDX and X-ray strain analysis (XSA).

In order to test the theoretical predictions made regarding the non metal substitutions, a fast synthesis method was developed where reactive gas gradients are employed during combinatorial thin film deposition. This method is evaluated for TiN_x and TiO_y. Characterization of these films was done by EDX, XRD and Nanoindentation. Additionally, $TiAlN_x$ and $TiAlN_xO_y$ were deposited using nitrogen and oxygen gas phase gradients, respectively, and analyzed by means of EDX and XRD.

2.2.1 Magnetron Sputtering

2.2.1.1 Cr_2AlC + O

As it was expected that small additions of oxygen in the gas phase may change the sputtering process in a compound target heterogeneously (inhomogeneous oxygen coverage and/or sputtering yield) and thus may lead to composition variations in the growing film, combinatorial DC magnetron sputtering from Cr, Al and C targets 40 mm in diameter was applied. This experimental strategy ensures areas with similar Cr:Al:C ratios as the oxygen concentration was varied by the O_2-partial pressure supplied during deposition. Sapphire wafers (50 mm in diameter) were used as substrates and heated to 615 °C before deposition. During 20 min deposition, the substrate temperature stayed between 615 °C and 625 °C, determined with a thermocouple clamped onto the substrate surface. The base pressure was below 10^{-5} mbar, during the depositions the Ar pressure was 750 mPa and the O_2-flow was

varied from 0 to 1 and 2 sccm, resulting in an O_2 pressure of 10 and 20 mPa, respectively. The power densities at the Cr, Al and C targets were 7.2, 6.4 and 11.1 W/cm², respectively. In the regions with composition close to the MAX phase composition the films exhibit a thickness of 1 to 1.2 µm corresponding to a deposition rate of 0.05 to 0.06 µm/min. The ratio between condensing residual water vapor and the flux of deposited Cr_2AlC is therefore smaller than 10^{-2} which implies that oxygen incorporation in the range of few at.% can be studied with the deposition setup used.

2.2.1.2 Gas phase gradients

The experiments were conducted in an industrial scale deposition system (CemeCon CC800/9) using a rectangular 500 x 88 x 10 mm³ Ti and TiAl target, respectively. As shown in the schematic Figure 1, a gas inlet was installed at the top of the long end of the magnetron, which was used to introduce N_2 or O_2 while Ar was introduced homogeneously.

Figure 1: Experimental setup for combinatorial reactive magnetron sputtering using gas phase gradients.

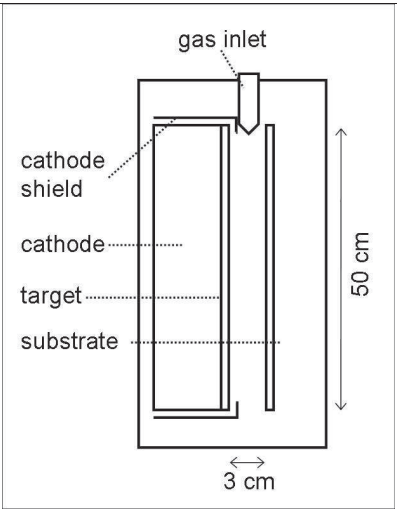

A 500 x 120 x 3 mm³ substrate holder was chosen with a target-to-substrate distance of 30 mm. Float glass substrates were used covering an area of 300 x 25 mm². The substrates were electrically floating at a potential of -25 V to -35 V. A Chemfilt Ionsputtering AB Sinex 3 High Power Pulsed Magnetron Sputtering (HPPMS) generator was used with a pulse width of 70 µs, a frequency of 400 Hz and a set voltage of -700 V. For TiN_x, $TiAlN_x$ and $TiAlN_xO_y$, the substrates were heated to 260 °C before deposition and the temperature increased to approx. 370 °C during 10 min deposition. No intentional heating was used during deposition of TiO_y. The Ar background pressure was 535 mPa for deposition of TiN_x and $TiAlN_x$ and 1 Pa for TiO_y, leading to mean free path lengths of ~20 mm and ~10 mm, respectively. For deposition of $TiAlN_xO_y$, the background gas consisted of Ar and N_2 with partial

pressures of 410 mPa and 125 mPa, respectively, thus keeping the mean free path at ~20 mm.

2.2.2 Characterization

EDX measurements were carried out in a scanning electron microscope Jeol JSM-6480 with attached EDAX Genesis 2000 EDX detector using an acceleration voltage of 12 kV. Each sample was measured by XRD using a Bruker AXS D8 Discover General Area Detection Diffraction System with Cu-Kα radiation. Nanoindentation was done with a Hysitron Triboindenter using the Oliver-Pharr method [46] and maximum forces of 500 µN and 1 mN. The reduced modulus and hardness were determined from the average of nine indents with constant force.

Characterization of the combinatorially deposited Cr-Al-C-O film was done with a 7x7 mm grid, resulting in 37 samples to be measured per wafer. The composition of one sample of each wafer was measured with wavelength dispersive X-ray spectroscopy and subsequently used as a standard for EDX to determine the chemical composition of the other points of the sample. No evidence for texture was observed in the deposited samples. Therefore, X-ray strain analysis (XSA) could be performed using the $\sin^2\psi$ method [47-49], where ψ is the tilt angle, assuming a biaxial stress state and macroscopically elastic isotropy (shear anisotropic factor of Cr_2AlC is between 1.06 and 1.48 [50-52]). The tilt angle ψ* under which the strain-free lattice spacing can be obtained is calculated according to the following equation:

$$\sin\psi^* = [2v/(1+v)]^{0.5}$$

where v is the Poisson's ratio (between 0.192 and 0.236 [50-52]). Here, v = 0.2 was used. The strain was determined from a fit to 21 measurements of the 103 diffraction peak under different ψ angles between -90° and +90° at a detector to sample distance of ~16 cm. In order to increase the resolution from 31 pixels/° to 47 pixels/°

in the 2Θ range, the detector to sample distance was increased to 26 cm for the measurement of the peak positions at ψ = 0°. Thus, together with the previously determined strain, the strain-free plane spacings $d_{(hkl)}$ of the (100), (101), (103), (106) and (110) planes could be determined. Using a least square fitting procedure of the inverse squares of the 5 lattice spacings $1/d_{(hkl)}^2$, the inverse lattice parameters $1/a^2$ and $1/c^2$ were determined. The grain size was calculated from the peak broadening using the Scherrer equation, where a shape factor of 0.9 was used [53].

3 Results and Discussion

3.1 Oxygen incorporation in M_2AlC (M = Ti, V, Cr)

3.1.1 Introduction

$M_{n+1}AX_n$ phases (M = transition metal; A = A-group element; X = C or N) are nanolaminates that combine metallic and ceramic properties as they consist of alternating layers with metallic (MA) and covalent/ionic bonding (MX) [54, 55]. As the combination of properties such as resistance against thermal shock [54, 56], high stiffness [37, 57], good oxidation resistance [17-20, 58-63] and self-healing behavior [64-66] qualify MAX phases for high temperature applications, interaction with oxygen -especially incorporation of oxygen in the initial stages of oxidation- is essential for understanding and improving the performance of these materials. Yet, systematic studies on oxygen incorporation in MAX phases are missing in the literature. Additionally, oxygen stemming from residual gas [67] is often incorporated during vapour phase condensation of $M_{n+1}AX_n$ phases [58, 68] and the effect thereof has not been investigated to date.

Recently, it has been shown that oxygen can replace carbon in Ti_2AlC [68, 69]. Additionally, it has been proposed based on ab initio calculations that oxygen incorporation on carbon sites is energetically favoured over interstitial sites [33] and that the formation of $Ti_2AlC_{1-x}O_x$ is stable compared to competing phases up to $x = 0.75$ [70]. This is of particular relevance in physical vapor deposition due to oxygen incorporation from residual gas which is primarily H_2O in high vacuum [67]. While it is known that the amount of incorporated H can be reduced by ion bombardment [71], the oxygen stemming from H_2O is most likely incorporated during growth.

The goal of this work is to explore phase stability of oxygen-containing M_2AlC (M = Ti, V, Cr) phases. In particular, the incorporation of oxygen in M_2AlC was studied to determine whether (metastable) oxygen dissolution in M_2AlC may affect oxide formation in the initial stage of oxidation. This is of relevance for the high-temperature performance of MAX phases as oxygen dissolution may affect the nucleation of metastable oxides during oxidation. Additionally, the oxygen dissolution is of importance for the design of self-healing MAX phases [64-66].

It is shown by ab initio calculations that oxygen populates carbon vacancies in Ti_2AlC and V_2AlC, while oxygen is incorporated interstitially in Cr_2AlC. The latter result is rather surprising as this is the first claim of stable interstitials in MAX phases. Therefore, combinatorial thin film deposition was used to evaluate this prediction. The comparison between theory and experiment shows that oxygen is in fact incorporated as interstitial in the aluminium layer of Cr_2AlC up to a metastable solubility limit of 3.5 at.% under the deposition conditions studied.

3.1.2 Ab initio Calculations

M_2AlC_{1-x} (M = Ti, V, Cr) phases were quantum mechanically described and the energies of formation of carbon vacancies and substitutional as well as interstitial incorporation of oxygen in M_2AlC_{1-x} were calculated. Figs. 1a and 1b illustrate the corresponding defects in the M_2AlC_{1-x} supercell.

Figure 1: Super cell configurations considered for incorporation of oxygen in M_2AlC. Medium-sized blue spheres correspond to M atoms, large red to Al, small brown to C and small yellow to oxygen. The small white sphere indicates a carbon vacancy. For calculations, the super cells shown were additionally doubled in c-direction.

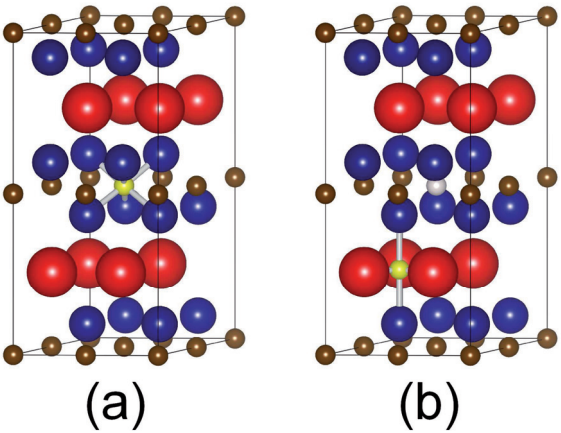

The defect energies as well as the resulting lattice parameters for x = 0.125 (this corresponds to two defects per supercell) are listed in Table 1, together with the energy of formation and the lattice parameters of the defect-free M_2AlC phases. The defect energies are plotted in Figure 2 together with the energy of formation of carbon vacancies in binary MC carbides from Ref [72] .

		Ti_2AlC	V_2AlC	Cr_2AlC
defect-free	ΔE_f [eV/atom]	-0.693	-0.498	-0.230
	a [Å]	3.071	2.911	2.847
	c [Å]	13.720	13.100	12.688
carbon vacancies	$\Delta E_{f,C\text{-}vac}$ [eV/defect]	3.0	2.5	0.9
	a [Å]	3.059	2.887	2.830
	c [Å]	13.757	13.152	12.657
Oxygen replacing carbon	$\Delta E_{f,C\text{->}O}$ [eV/defect]	-4.1	-2.5	-1.4
	a [Å]	3.063	2.904	2.841
	c [Å]	13.672	13.107	12.759
Oxygen interstitial	$\Delta E_{f,O\text{-}int}$ [eV/defect]	-4.4	-3.6	-3.2
	a [Å]	3.083	2.935	2.872
	c [Å]	13.679	13.068	12.719
Oxygen interstitial + carbon vacancy	$\Delta E_{f,C\text{->}O\text{-}int}$ [eV/defect]	-1.5	-1.1	-2.1
	a [Å]	3.062	2.918	2.855
	c [Å]	13.712	13.088	12.678

Table 1 - Energy of formation and lattice parameters for defect-free M_2AlC (M: Ti, V, Cr) phases and energy of formation of defects in these phases obtained from ab initio calculations.

Dahlqvist et al. calculated a decrease in *a* and *c* lattice parameters of 0.65 % and 0.36 %, respectively, when increasing the oxygen content from Ti_2AlC to $Ti_2AlC_{0.75}O_{0.25}$ [70]. The decrease observed here for $Ti_2AlC_{0.875}O_{0.125}$ is 0.26 % and 0.34 % and therefore in good agreement assuming Vegard's law [73]. Additionally, the results are in agreement with Liao et al. showing that oxygen incorporation on C sites in Ti_2AlC is energetically favoured over oxygen incorporation on interstitial sites [33].

Figure 2: Point defect energies for M_2AlC phases: energy of formation for carbon vacancy $\Delta E_{f,C\text{-}vac}$, for oxygen incorporation on carbon sites $\Delta E_{f,C\text{->}O}$, oxygen interstitials $\Delta E_{f,O\text{-}int}$ and oxygen interstitials in the presence of carbon vacancies $\Delta E_{f,C\text{->}O\text{-}int}$.

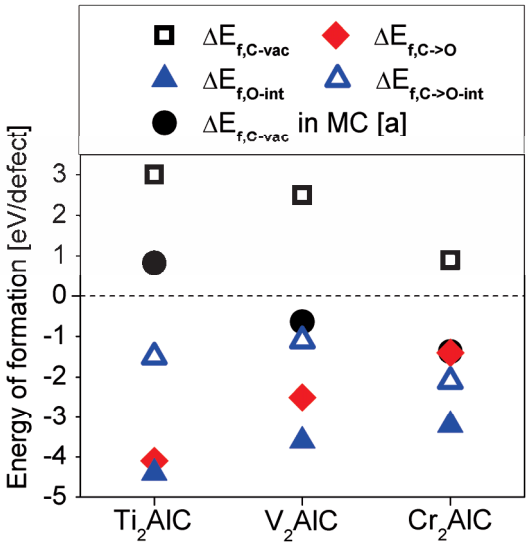

[a]: [72]

In Figure 2, it is shown that the defect energies of carbon vacancies $\Delta E_{f,C\text{-}vac}$, substitutional $\Delta E_{f,C\text{->}O}$ as well as interstitial oxygen $\Delta E_{f,O\text{-}int}$ follow the same trend, respectively, when the valance electron concentration (VEC) in M_2AlC_{1-x} is increased, i.e. Ti is replaced by V and subsequently by Cr. $\Delta E_{f,C\text{-}vac}$ is positive and decreasing from 3.0 to 0.9, which is in agreement with the trend calculated by Music et al. for the binary MC transition metal carbides [72] added for comparison to Figure 2. The carbon vacancy energies calculated here for MAX phases are by 2 to 3 eV/defect higher than for the binary MC phases which may be understood based on the fact

that TiC and VC show a broad solubility range while MAX phases are normally assumed to be stoichiometric phases. It is worth noting that the decrease in $\Delta E_{f,C\text{-}vac}$, when changing from Ti to V, is much smaller compared to the decrease when changing from V to Cr. Both the defect energies for oxygen replacing carbon as well as interstitial oxygen incorporation are negative and decreasing in value for increasing VEC. The energy for oxygen interstitials in the presence of carbon vacancies, however, is increasing when Ti is replaced by V and decreasing again when V is replaced by Cr.

Interestingly, the energy for oxygen interstitials in the presence of carbon vacancies is more negative than the energy of oxygen substituting carbon in $Cr_2AlC_{1-x}O_x$. This indicates that oxygen is not incorporated on carbon sites in Cr_2AlC, as it was observed for Ti_2AlC [33, 68-70], but in interstitial sites in the Al layer. In fact, this is the first claim of interstitial oxygen incorporation in MAX phases. In the following section, the electronic origin of the different oxygen incorporation behaviors of the M_2AlC (M = Ti, V, Cr) phases is investigated.

The magnitude of the formation energy of oxygen interstitials in the presence of carbon vacancies $\Delta E_{f,C\text{->}O\text{-}int}$ is close to the superposition of the energy of formation of carbon vacancies and oxygen interstitials which lead in sum to -1.4, -1.1 and -2.3 eV/atom for M = Ti, V and Cr, respectively, indicating that these defects do not interact strongly. Therefore, both defects are discussed separately in terms of charge transfer and relaxation of the atoms in the following to show differences between Ti_2AlC, V_2AlC and Cr_2AlC. No systematic change in density of states or charge distribution (not shown here for brevity) could be observed due to interstitial oxygen incorporation when changing the VEC. However, carbon vacancies induce different changes in atomic and electronic relaxation for Cr_2AlC compared to Ti_2AlC and V_2AlC which may explain the significantly smaller energy of formation of carbon vacancies.

Figure 3: effective charge of the atoms as function of distance from the carbon vacancy position in M_2AlC and $M_2AlC_{0.875}$.

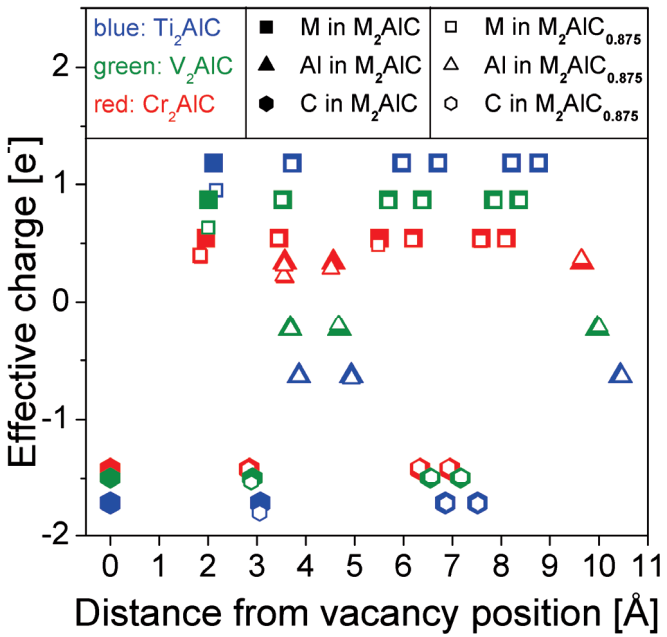

In Figure 3, the effective charges of the M, Al and C atoms in M_2AlC and $M_2AlC_{0.875}$ are plotted as a function of the distance from the carbon vacancy positions used for the calculations of energy of formation of carbon vacancies. From the distance between open and filled symbols in x-direction the relaxation of the atoms to and from the vacancies may be deduced and the distance in y-direction indicates the change in charge state. When carbon vacancies are created, the effective charge per carbon atom (between 1.4 and 1.7 electrons for all three M_2AlC phases) has to rearrange. For Ti_2AlC and V_2AlC, this charge rearrangement is accommodated only by the six nearest neighbors of Ti/V atoms, exhibiting a distance of ~2 Å. The effective charges of the nearest carbon neighbors (~3 Å) as well as next nearest Ti/V atoms (~3.6 Å) and the adjacent layers of Al atoms (~3.8 Å) do not change

significantly. In the case of Cr_2AlC, on the other hand, a notable charge transfer even to the adjacent Al layers (~3.6 Å) and the next layer of Cr atoms (~5.5 Å) can be observed. Only in the case of Cr_2AlC, relaxation of the adjacent Cr atoms into the vacancy site can be observed, decreasing the distance by 7%, while V atoms stay at the same distance and Ti atoms even move further away from the carbon vacancy position (+2.5%). The change in *c*-lattice parameter is reflected by the change in distances of atoms further away (>5 Å): For $Cr_2AlC_{0.875}$, *c* is decreasing by 0.2% whereas it is increasing by 0.3% and 0.4% for $Ti_2AlC_{0.875}$ and $V_2AlC_{0.875}$, respectively. These results indicate that the ability for larger atomic and electronic relaxation is responsible for the lower energy of formation of carbon vacancies in Cr_2AlC compared to Ti_2AlC and V_2AlC.

Since the energy of oxygen replacing carbon is lower compared to the energy for incorporating oxygen interstitials while generating carbon vacancies, it is likely that oxygen replaces carbon in Ti_2AlC_{1-x} and V_2AlC_{1-x} while oxygen is incorporated interstitially in the Al-layer in Cr_2AlC_{1-x}. The notion of oxygen incorporation on substitutional sites in Ti_2AlC was presented before by Liao et al. [33] and is in agreement with Rosén et al. [68] and Persson et al.[69].

The prediction of oxygen interstitials in the Al layer of Cr_2AlC is the first claim for interstitial incorporation of atoms in a MAX phase. As can be seen in Table 1, interstitial and substitutional oxygen incorporation lead to characteristic changes of the lattice parameters *a* and *c*, which will be used to experimentally evaluate the prediction.

3.1.3 Experiments

The oxygen contents measured in the three combinatorial samples are in the range of 1 at.%, 2-5 at.% and 9-11 at.% for oxygen partial pressures of 0, 10 and 20 mPa,

respectively. In order to determine the change in lattice parameter due to oxygen incorporation, several contributions to the measured lattice spacing data have to be considered: Contributions from variation of Cr-, Al-, and C-contents in the MAX phase as well as contributions due to stresses induced during thin film growth and cooling of the film-substrate-composite. The different contributions to the lattice parameters are discussed separately in the following sections.

3.1.3.1 The Cr-, Al-, and C-contents in the MAX phase

As different samples on each wafer are analyzed, which exhibit different compositions and phases, the composition of the MAX phase may change due to defects such as Al substituting Cr [74] or C vacancies. These defects may lead to changes in lattice parameters in the same order of magnitude as the changes by oxygen incorporation. The effect of carbon off-stoichiometry in the MAX phase is minimized here by only studying carbon deficient samples where Cr_2AlC and Cr_2Al are present. Therefore, the same research question is addressed theoretically and experimentally, i.e. whether oxygen is incorporated on a carbon vacancy site or interstitially besides carbon vacancies. The effect of variation in the Cr:Al ratio will be discussed later.

3.1.3.2 Stresses induced during growth and cooling

Thin films often exhibit growth-induced stresses as well as stresses due to thermal mismatch between film and substrates, both of which are acting in-plane. These stresses lead to strain which is dependent on the orientation: For compressive (tensile) in-plane stresses, lattice planes which are parallel to the sample surface exhibit larger (smaller) lattice spacings while lattice planes which are perpendicular to the surface exhibit smaller (larger) lattice spacings. In XSA, the lattice spacing is measured as function of the tilt angle ψ allowing the determination of the strain-free

lattice spacing. Results of XSA are shown in Figure 4 for samples on the three wafers where only Cr_2AlC and Cr_2Al are present.

Figure 4: Lattice spacing of the (103) peak $d_{(103)}$ as a function of sample tilting $\sin^2\psi$ for the positions of the samples where only Cr_2AlC and Cr_2Al are present. The oxygen content of each sample is included in the figure. For simplicity, only results for positive angles ψ are included.

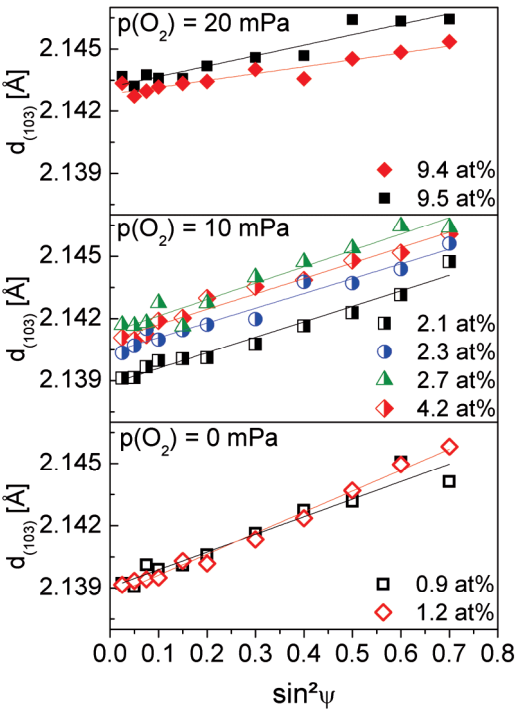

It can be seen that the stresses are on the same order of magnitude for samples deposited with an oxygen partial pressure of 0 and 10 mPa, respectively. The stresses are decreased significantly upon increasing the oxygen pressure to 20 mPa, as can be seen from the decrease in slope of the linear fit functions in the upper array of Figure 4. Additionally, the lattice spacings at $\sin^2\psi = 0$ are significantly (up to

0.2 %) increased upon increasing the oxygen pressure to 20 mPa. This may be interpreted as a significant increase of the lattice spacing and thus lead to the wrong conclusion, since the strain-free lattice spacing can only be determined from the lattice spacing at $\sin^2\psi^* = 0.333$. Here, only minor differences in $d_{(103)}$ (up to 0.09%) can be observed as the oxygen flow is increased, underlining the importance of XSA.

oxygen pressure [mPa]	oxygen content [at.%]	$d_{(100)}$ [Å]	$d_{(101)}$ [Å]	$d_{(103)}$ [Å]	$d_{(106)}$ [Å]	$d_{(110)}$ [Å]	a [Å]	c [Å]
0	0.9	2.4771	2.4282	2.1438	1.6164	1.4290	2.8583	12.8084
0	1.2	2.4776	2.4317	2.1429	1.6178	1.4302	2.8604	12.8172
10	2.1	2.4778	2.4331	2.1428	1.6191	1.4300	2.8602	12.8356
10	2.3	2.4793	2.4339	2.144	1.6179	1.4305	2.8613	12.8174
10	2.7	2.4791	2.4350	2.1447	1.6197	1.4317	2.8632	12.8334
10	4.2	2.4795	2.4317	2.1446	1.6204	1.4314	2.8624	12.8452
20	9.4	2.4795	2.4384	2.1444	1.6199	1.4312	2.8628	12.8387
20	9.5	2.4802	2.4365	2.1442	1.6213	1.4312	2.8627	12.8570

Table 2 - Strain-free lattice spacings and lattice parameters at the sample positions considered as a function of the oxygen content.

The strain-free interplanar spacings of the Cr_2AlC (100), (101), (103), (106) and (110) planes are listed in Table 2, together with the fitted *a* and *c* lattice parameters as well as the measured oxygen contents. The lattice parameters obtained at the lowest oxygen contents are in good agreement (differences smaller 0.2%) to the *a* (*c*) values determined by Jeitschko et al. and Tian et al., which are 2.86 Å (12.82 Å) [75] and 2.863 Å (12.814 Å) [76], respectively.

3.1.3.3 Oxygen incorporation in Cr_2AlC

Figure 5: Comparison of experimental and calculated *a* lattice parameter data. The lines serve as guide to the eyes.

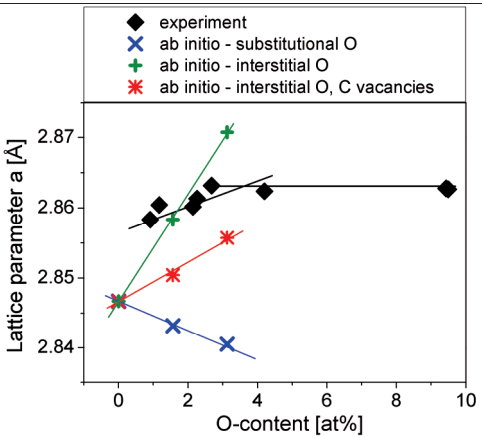

Figure 6: Comparison of experimental and calculated *c* lattice parameter data. The lines serve as guide to the eyes.

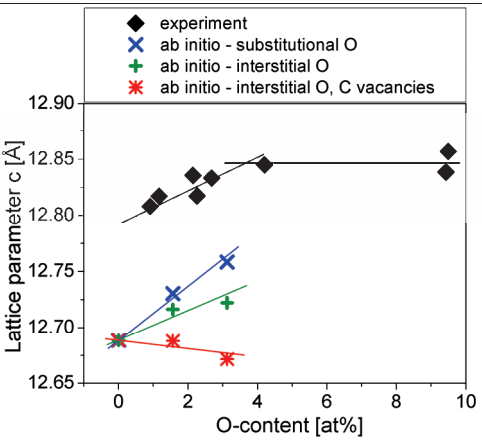

The *a* and *c* lattice parameters are plotted in Figure 5 and 6, respectively, as a function of the oxygen content. For comparison, the results from ab initio calculations

are added. Here, substitutional oxygen incorporation as well as oxygen interstitials in the Al layer are considered. The latter was predicted by ab initio calculations to be more stable (cf section 3.2.2). As carbon deficient Cr_2AlC is analyzed experimentally in this work, the change of lattice parameters with oxygen interstitials is included both in the presence and absence of carbon vacancies. Experimentally, an increase of the lattice parameters *a* and *c* is observed when the oxygen content is increased up to 3.5 at.%. The lattice parameters do not correlate with the variation of the Cr:Al ratio of the samples measured by EDX (not shown for brevity) which indicates that the Cr and Al content of the MAX phase is constant at all points. At constant Cr and Al content, only the variation in carbon or oxygen content can be responsible for the changes in lattice parameters observed. If the increase in *a* lattice parameter in Figure 5 would be due to a change in carbon content, based on ab initio calculations (c.f. Table 1) the fraction of carbon vacancies x in Cr_2AlC_{1-x} has to decrease. Quantitatively, the increase in *a* lattice parameter of 0.17% upon increase of oxygen concentration from ~1 to ~3 at.% would correspond to a decrease of the fraction of carbon vacancies x in Cr_2AlC_{1-x} by 0.035 (based on the ab initio data in Table 1) which corresponds to nearly 1 at.% as the carbon fraction in Cr_2AlC is 25 at.%. It should be mentioned that carbon vacancies in Cr_2AlC have not been reported experimentally to the best of the authors' knowledge. It is not reasonable to assume that 2 at.% oxygen incorporation in the film consisting of Cr_2AlC and Cr_2Al would affect the carbon content in Cr_2AlC by 1 at.% without incorporation of oxygen into the MAX phase. Therefore, the change of lattice parameters indicates the incorporation of oxygen in Cr_2AlC. The lattice parameters do not increase further for oxygen contents larger than 3.5 at.% which indicates a solubility limit of oxygen in Cr_2AlC of 3.5 at.% under the deposition conditions studied.

The experimentally observed increase of *a* is reproduced well by the ab initio calculations assuming interstitial oxygen in the presence of carbon vacancies. Accordingly, the trend of *c* is between the ab initio calculations assuming interstitial oxygen in the presence and in the absence of carbon vacancies. Thus, the changes of both lattice parameters with oxygen content are in good agreement with the prediction from ab initio calculations indicating that oxygen is incorporated interstitially in the Al layer. As discussed for the calculation details in section 2.1, the reason for the generally smaller values of the calculated lattice parameters of Cr_2AlC could be the GGA exchange functional used in this work which is known to overestimate the stability of delocalized states [25, 34-36]. While this leads to an error in the absolute value for the lattice parameters, the trend is expected to depend on geometry. As can be seen in Table 1, the lattice parameter *a* of the three MAX phases studied increases between 0.4 and 0.8 % if oxygen is incorporated interstitially, leading to $M_2AlCO_{0.125}$. This may be understood by considering the geometry shown in Figure 1b: The interstitial oxygen widens the lattice in the basal plane as the interstitial site is not large enough to accommodate the oxygen atom. On the other hand, *a* decreases by 0.2 % if oxygen is incorporated substitutionally, forming $M_2AlC_{0.875}O_{0.125}$, due to the smaller covalent radius of oxygen (0.66 Å) compared to carbon (0.77 Å). Hence, geometric considerations are sufficient for explaining the oxygen-induced change in *a* (see Figure 5) while the change in *c* may be significantly affected by the GGA functional leading to higher uncertainty in the *c* values shown in Figure 6.

As mentioned above, the experimental observation that the lattice parameters do not change when the oxygen content is increased above 3.5 at.% indicates that this is the solubility limit of oxygen in Cr_2AlC under the deposition conditions studied. As

oxygen contents as high as 9.5 at.% were measured in the sample, a discussion on where the additional oxygen may be located is appropriate.

3.1.3.4 Additional oxygen in the samples

Figure 7: Average grain size (squares) and the area under the Cr_2AlC XRD peaks (circles) as a function of the oxygen content.

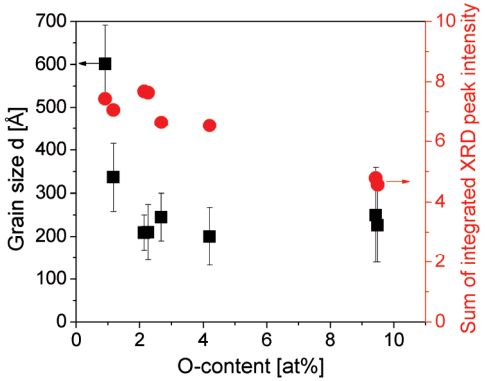

In Figure 7 the average grain size as determined from the broadening of the 100, 101, 106 and 110 XRD peaks is shown where the error bars indicates the standard deviation. When the oxygen content is increased from 1 to 2 at.% the grain size decreases from 600 to 200 Å which could be due to oxygen-induced renucleation [77, 78]. For higher oxygen contents, the grain size appears to be unaffected within the error bars. The decrease of the grain size leads to a larger grain boundary area, which could accommodate oxygen. As a measure of crystallinity, the sum of the integrated peak intensities of the MAX phase peaks is shown on the second axis in Figure 7. It can be seen that the crystallinity decreases with increasing oxygen content, while no systematic change of the area under the Cr_2Al peaks has been observed (not shown for brevity) which -together with the constant grain size for oxygen contents larger than 2 at.% and constant thickness of the samples- indicates

an increase of grain boundary thickness or the formation of an X-ray amorphous (grain boundary) phase. Therefore, it is proposed that the additional oxygen is located at the grain boundary or in an additional amorphous phase.

3.1.4 Implication: Oxidation of M_2AlC

In equilibrium it is expected that high temperature oxidation of M_2AlC (M = Ti, V, Cr) results in the formation of Al_2O_3 due to the more negative standard Gibbs energy of formation of Al_2O_3 (-564 kJ/mol) compared to TiO_2 (-480 kJ/mol), VO_2 (-364 kJ/mol), V_2O_5 (-318 kJ/mol) or Cr_2O_3 (-388 kJ/mol) [79], where all energy values refer to oxidation by one mole of oxygen. Yet, during oxidation of these M_2AlC phases different oxides are observed: Additionally to Al_2O_3, the formation of TiO_2 + $TiAl_2O_5$ [17-20] and VO_2 + V_2O_5 [21] are reported for Ti_2AlC and V_2AlC, respectively. Similar behaviour is reported for Ti_3AlC_2 [17, 60]. It should be noted that formation of TiO_2 was observed already after 3 min of oxidation at 1200 °C [18], indicating that TiO_2 does not form due to depletion of Al. For Cr_2AlC, on the other hand, the oxide scale consists only of Al_2O_3 with very small amounts of dissolved Cr_2O_3 [58, 59, 61, 62]. The occurrence of Cr_2O_3 during cyclic oxidation at 1200 °C - 1300 °C was argued to be due to spallation of the initially formed Al_2O_3 and subsequent oxidation of the Cr_7C_3 interlayer forming between the scale and the Cr_2AlC matrix [63] which indicates that Cr_2O_3 does not form due to oxidation of Cr_2AlC.

As Al_2O_3 is thermodynamically the most stable oxide for all three previously discussed M_2AlC phases, the formation of Ti and V oxides has to originate in a non-equilibrium mechanism. It has been shown on the one hand that oxygen substitutes carbon in Ti_2AlC (c.f. [33, 68-70] and section 3.2.2) and V_2AlC (c.f. section 3.2.2). This leads to formation of Ti-O and V-O bonds (cf. Figure 1a), which may act as nucleation sites for titanium and vanadium oxides. On the other hand the here

presented data suggest that in Cr_2AlC oxygen is incorporated interstitially in the Al layer (cf. Figure 1b). This leads to formation of Al-O bonds, which may facilitate the nucleation of aluminum oxides. Hence, it is suggested that the here identified different oxygen incorporation sites may be significant for the initial stages of oxidation and may therefore enable different oxide formation mechanisms, i.e. preferential nucleation of titanium and vanadium oxides in Ti_2AlC and V_2AlC, respectively, and nucleation of aluminium oxide in Cr_2AlC. Furthermore, this notion may explain the differences in oxidation behaviour observed for Ti_2AlC and V_2AlC (non-equilibrium) as opposed to Cr_2AlC (equilibrium).

3.1.5 Summary

The energies of formation of carbon vacancies and oxygen incorporation into the MAX phases Ti_2AlC, V_2AlC and Cr_2AlC were studied by ab initio calculations. The energy of formation of carbon vacancies is much smaller in Cr_2AlC than in Ti_2AlC and V_2AlC due to a larger ability of atomic and electronic relaxation. The comparison of energies of oxygen incorporation for several configurations indicates that oxygen replaces carbon in Ti_2AlC and V_2AlC, but is incorporated interstitially in the Al layer of Cr_2AlC even for carbon deficient Cr_2AlC. To evaluate these predictions, combinatorial DC sputtering at oxygen partial pressures of 0, 10 and 20 mPa was used to deposit thin films with different oxygen concentrations. Two phase-regions of Cr_2AlC and Cr_2Al were investigated in order to study oxygen incorporation in carbon deficient Cr_2AlC. X-ray strain data indicates that the *a* and *c* lattice parameters increase with oxygen content. These trends are in good agreement with the change of lattice parameters predicted by ab initio calculations and therefore corroborate the notion of interstitial oxygen incorporation in Cr_2AlC. A metastable solubility limit for oxygen of 3.5 at.% was determined while it is suggested that additional oxygen is incorporated

in the grain boundary or as an X-ray amorphous phase. This is the first report on interstitial oxygen incorporation into a MAX phase and may be of relevance during the initial stages of oxidation of Cr_2AlC: interstitial oxygen incorporation leads to formation of Al-O bonds which may act as nucleation sites for Al_2O_3. Further implications for oxidation of M_2AlC were discussed.

3.2 Phase stability and elastic properties of $Ti_{0.5}Al_{0.5}N_x$

3.2.1 Introduction

Hard titanium nitride (space group $Fm\bar{3}m$) based coatings are commonly used for metal cutting applications. A significant improvement of oxidation and wear resistance and hardness was observed due to alloying TiN with Al forming $Ti_{1-x}Al_xN$ [80, 81]. Recently, Rachbauer et al. measured the composition of TiAlN films by atom probe tomography and reported it to be slightly overstoichiometric with respect to nitrogen [82]. However, it is unclear at this point whether this is due to interstitial nitrogen or metal vacancies. Based on residual stress data obtained by X-ray diffraction, Oettel et al. suggested interstitial nitrogen to be responsible for nitrogen overstoichiometry that was measured for reactive magnetron sputtered TiN and TiAlN films by glow discharge optical spectroscopy [83]. Bujak et al. and Zhou et al. reported the influence of nitrogen flow during deposition on composition and elastic modulus of TiAlN using cathodic arc and reactive magnetron sputtering, respectively [84, 85]. In both reports, a decrease in elastic modulus was observed when the nitrogen content in the film increased above 50 at.%, however, reasons for this behavior were not discussed. Additionally, the elastic modulus was reported to decrease by ~15% as the nitrogen content is decreased from 50 to 44 at.% [84, 85]. Larger roughness [84] or changing texture [85] were proposed as possible causes for this. Composition induced changes in defect structure were not considered [5,6]. Recently, Alling et al. reported the calculated decomposition pattern for TiAlN with N vacancies and proposed that small amounts of nitrogen vacancies enhance the isostructural decomposition through Ti clustering around the vacancies [86]. Hence, the origin of N over- and understoichiometry in TiAlN although experimentally clearly established is unknown. Furthermore, the cause of the N concentration induced

changes in elastic properties is not understood. Therefore, ab initio calculations of several point defect concentrations were carried out to shed light on the energetics of vacancies, interstitials and anti-sites as well as their influence on the elastic behavior of over- and understoichiometric TiAlN. Additionally, it will be shown in chapter 3.3, that defects become stable in TiAlNO, so understanding defects in TiAlN is an important prerequisite for studying the oxynitride.

3.2.2 Ab initio Calculations

First, it was investigated whether metal or nitrogen vacancies interact by introducing them close to each other or maximizing their distance in the unit cell. No significant differences in terms of energy of formation, lattice parameter and elastic properties were observed, therefore, only the data for two vacancies with maximized distance are reported and discussed here.

Figure 1: Energy of formation of $Ti_{0.5}Al_{0.5}N_x$ as a function of the nitrogen content for different point defects.

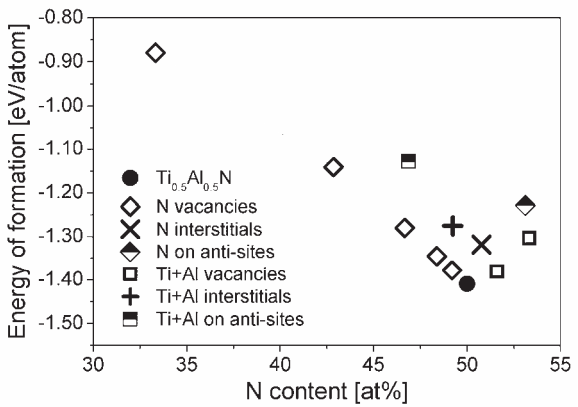

In Figure 1, the energy of formation of $Ti_{0.5}Al_{0.5}N_x$ is shown as a function of nitrogen content for different types of defect. For all point defects, the Ti:Al ratio was kept constant at 0.5. The points with minimum energy of formation for each composition are connected by a line. It can be seen that for $Ti_{0.5}Al_{0.5}N_x$ with x<1 a lower energy of formation is obtained with nitrogen vacancies rather than titanium and aluminium interstitials or titanium and aluminium on anti-sites. From the negative curvature it can be concluded that the decomposition into nitrogen-rich and nitrogen-deficient regions is energetically favoured which is in good agreement with the decomposition pattern calculated by Alling et al. [86]. On the other hand, nitrogen overstoichiometric $Ti_{0.5}Al_{0.5}N_x$ (x>1) is energetically most stable if metal vacancies are created rather than interstitial nitrogen as previously proposed in reference [83] or nitrogen on metal sites.

Figure 2: Lattice parameter of $Ti_{0.5}Al_{0.5}N_x$ as a function of nitrogen content. Deviations in nitrogen content from 50 at.% are accommodated by nitrogen and metal vacancies.

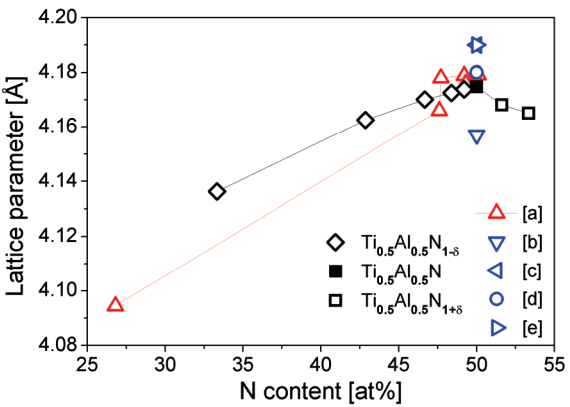

[a]: [87] [b]: [88] [c]: [89] [d]: [90] [e]: [91]

The effect of vacancies on the lattice parameter of $Ti_{0.5}Al_{0.5}N_x$ is shown in Figure 2. For comparison, experimental data was added [87-91]. The lattice parameter

decreases linearly with decreasing nitrogen content. It should be noted that the experimental data from reference [87-90] in Figure 2 was determined without stress analysis, although it is known that stresses evolve during thin film deposition and may change with nitrogen content [83, 88, 89]. Nevertheless, good agreement (deviations smaller 0.5%) is obtained between theoretical and experimental data. Comparing the same deviation from stoichiometry, the decrease of the lattice parameter is with 0.23 % for x = 0.533 larger for nitrogen overstoichiometric $Ti_{0.5}Al_{0.5}N_x$ compared to 0.11 % for x = 0.467. This may be understood based on the fact that titanium and aluminum atoms have larger radii than nitrogen and hence titanium and aluminum vacancies lead to larger decrease in the lattice parameter. To the best of the authors knowledge no experimental study is published to date where lattice parameters are reported for $Ti_{0.5}Al_{0.5}N_x$ with x>1.

Figure 3: Elastic modulus of $Ti_{0.5}Al_{0.5}N_x$ as a function of nitrogen content. Deviations in nitrogen content from 50 at.% are accommodated by nitrogen and metal vacancies.

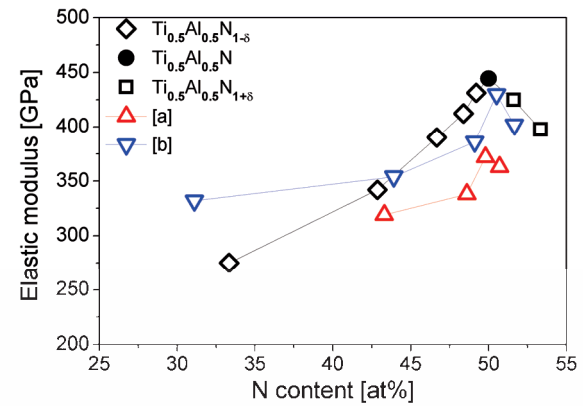

[a]: [84] [b]: [85]

The influence of nitrogen and metal vacancies on the elastic modulus is illustrated in Figure 3, together with experimental data [84, 85]. Good agreement is obtained between calculated and experimental data. Irrespective of the type of vacancy, the bulk modulus is decreased by approximately 7 % when x in $Ti_{0.5}Al_{0.5}N_x$ is 1.067 or 0.9375, corresponding to an increase or decrease of nitrogen content by 3 at.% or one vacancy per 16 formula units. This may be understood based on the fact that six bonds are broken when a vacancy is formed irrespective of the type of vacancy. Due to a decreasing Poisson's ratio, the elastic modulus decreases only by 4% for x=1.067 in $Ti_{0.5}Al_{0.5}N_x$ while the elastic modulus decreases by 7% for x=0.9375. The reported experimental elastic modulus [84, 85] decreases for overstoichiometric (x>1) $Ti_{0.5}Al_{0.5}N_x$ which corroborates the notion of metal vacancies in deposited TiAlN films. Considering also the calculated energies of formation, it may be inferred that nitrogen overstoichiometry observed in thin films [82, 84, 85] is due to metal vacancies rather than nitrogen interstitials or nitrogen atoms on anti-sites.

3.2.3 Summary

In conclusion, the origin of nitrogen over- and understoichiometry in TiAlN observed experimentally was studied. To this end, energies of formation, lattice parameters and elastic moduli of $Ti_{0.5}Al_{0.5}N_x$ (x = 0.5 - 1.14) were determined by ab initio calculations. For nitrogen as well as titanium and aluminium, vacancies, interstitials and anti-sites were considered. Based on energies of formation and a comparison of lattice parameter and elastic moduli to existing experimental data, it is shown that nitrogen understoichiometry in TiAlN is due to nitrogen vacancies while nitrogen overstoichiometry is due to metal vacancies and neither interstitials nor anti-sites are stable in TiAlN. Vacancies lead to a decrease in bulk modulus: irrespective of the type of vacancies, the bulk modulus is decreased by approximately 7% when x in

$Ti_{0.5}Al_{0.5}N_x$ is 1.067 or 0.9375 as the nitrogen concentration is increased or decreased by 3 at.%.

3.3 Phase stability and elastic properties $Ti_{0.5}Al_{0.5}N_xO_y$

3.3.1 Introduction

The chemical stability and cutting performance of TiN hard coatings was improved considerably by alloying with Al forming $Ti_{1-x}Al_xN$ [80, 81]. Significant improvements with respect to the tribological behaviour of $Ti_{1-x}Al_xN$ based coatings has been reported due to alloying with oxidation and wear resistance and hardness was observed due to alloying with V [92], Mo [93] or W [93] as suggested by Erdemir [94]. To date, there are only few reports on titanium aluminium oxynitrides: Luthier and Lévy deposited TiAlNO coatings using radio frequency magnetron sputtering of a Al_2O_3 + 1.5 TiN compound target [95]. They show that the as deposited TiAlNO exhibits a microstructure consisting of $(Ti,Al)N_x$ nanocrystallites embedded in an amorphous oxide matrix [95]. Tönshoff et al. reported that multilayer TiAlN/TiAlON coatings synthesized by magnetron sputter ion plating and high ion sputtering exhibit superior wear behaviour during dry drilling of tempered steel compared to conventional TiAlN coatings with the same microhardness [96]. This is proposed to be due to an improved oxidation resistance of TiAlNO compared to TiAlN [96]. Kawata et al. showed that TiAlON coatings exhibit smaller corrosion loss in contact with molten JIS ADC 12 aluminium alloy than TiN or TiAlN coatings [97]. Improvement in wear resistance caused by up to ~7 at.% additions of oxygen to TiAlN was reported by Sjölen et al. who synthesized TiAlNO by arc evaporation with varying nitrogen and oxygen contents [14]. Additionally, they show that TiAlNO grows epitaxially on TiAlN which served as a buffer layer up to an oxygen content of 35 at.% (O+N = 100 at.%) [14]. As the oxygen concentration is increased, a decrease of the ratio between metals and non-metals is observed [14]. Vacancy formation or the formation of oxides (which could not be detected by XRD) was proposed as

explanation for the change in stoichiometry [14]. The proposal of metal vacancies was also employed by Fabreguette et al. and Guillot et al. in order to explain the composition of TiN_xO_y films with x+y = 1.2 as measured by XPS and RBS [98, 99]. To the best of the author's knowledge, the effect of oxygen on phase stability of TiAlNO is not understood, including the reason for the increase in non-metal to metal ratio with increasing oxygen content [14, 98, 99]. The aim of this work is to contribute towards understanding the effect of oxygen additions on structure, phase stability and elastic properties of TiAlNO. Thus, it is implicitly intended to identify the origin of the non-metal overstoichiometry reported experimentally for oxynitrides [14, 98, 99] as well as the influence of oxygen on elastic properties.

3.3.2 Ab initio Calculations

3.3.2.1 Defect energies in TiAlN

The lattice parameter, energy of formation per defect and bulk modulus of $Ti_{0.5}Al_{0.5}N$ and $Ti_{0.5}Al_{0.5}N$ with one and two Ti, Al or N vacancies studied in chapter 3.2 are provided in Table 1 together with the data for one N or O interstitial in $Ti_{0.5}Al_{0.5}N$. These data will serve as reference for defects in $Ti_{0.5}Al_{0.5}N_{1-x}O_x$.

defect	a [Å]	E_f^{defect} [eV/defect]	B [GPa]
none	4.175	---	261
1 Ti vacancy	4.169	2.47	247
2 Ti vacancies	4.160	2.71	243
1 Al vacancy	4.172	1.99	251
2 Al vacancies	4.169	2.19	243
1 Ti and 1 Al vacancy	4.165	2.31	241
1 N vacancy	4.174	3.41	248
2 N vacancies	4.173	3.44	241
1 N interstitial tetrahedron gap	4.213	4.52	245
1 O interstitial tetrahedron gap	4.209	0.69	248

Table 1 - Results of calculations of one and two defects in $Ti_{0.5}Al_{0.5}N$: Lattice parameter *a*, energy of formation per defect E_f^{defect}, bulk modulus *B*.

It has been investigated whether vacancies interact by introducing them close to each other or maximizing the distance in the unit cell. No significant differences in terms of energy of formation, lattice parameter and elastic properties were observed, therefore, only the data for two vacancies with maximized distance are reported and discussed here. The energies of formation of a Ti, Al or N vacancy are 2.5, 2.0 and 3.4 eV/vacancy, respectively. The energy of formation for a second vacancy increases slightly (up to ~0.25 eV/vacancy). The energy needed to incorporate one nitrogen atom interstitially in a tetrahedron gap was determined to be 4.5 eV.

3.3.2.2 Phase stability of $TiAlN_{1-x}O_x$

The energy of mixing in $TiAlN_{1-x}O_x$ with x = 0, 1/32, 1/16, 1/8, 1/4, 1/2 and 1 was investigated. For x = 1/16, where two nitrogen atoms replaced by oxygen in the 2x2x2 supercell, the interaction of oxygen atoms with each other was analyzed. Configurations were tested with the two oxygen atoms placed as far from each other as possible; next to each other with two Ti atoms as common neighbours; next to each other with two aluminium atoms as common neighbours; next to each other with one Al and one Ti atom as common neighbour. The energy of mixing ΔE_{mix} for these

configurations is -23.7, -24.0, -23.0 and -22.8 meV/atom, respectively. ΔE_{mix} obtained from the SQS configuration with the same amount of oxygen is -24.0 meV/atom, hence no indication for ordering on the non-metal sublattice is observed. Therefore, random distribution of nitrogen and oxygen on the non-metal sublattice was assumed for the following calculations.

Figure 1: energy of mixing as a function of x in $Ti_{0.5}Al_{0.5}N_{1-x}O_x$. For comparison, the data reported by Graciani et al. [100] for titanium oxynitride $TiN_{1-x}O_x$ is added.

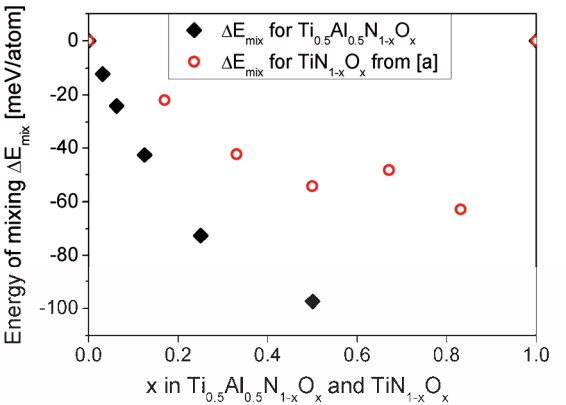

[a]: [100]

The energy of mixing for $TiAlN_{1-x}O_x$ is shown in Figure 1. The negative values of ΔE_{mix} indicate full miscibility of TiAlN and the hypothetical phase TiAlO with an interaction parameter Ω_{TiAlNO} [101] of -0.390 eV/atom (-37.6 kJ/mol). For comparison, the data reported by Graciani et al. for $TiN_{1-x}O_x$ [100] is added to the figure. It should be noted here that the data from Graciani includes entropic contributions to energy, where a temperature of 10K was considered [100]. However, it was reported that the entropic contribution is rather small ($-T\Delta S$ in the range of 1 meV) and can therefore be neglected [100]. Comparing Ω_{TiAlNO} to the interaction parameter Ω_{TiNO} in the $TiN_{1-x}O_x$ system (-0.210 eV/atom or 20.26 kJ/mol, neglecting the value for $x \approx 0.83$)

[100] shows that aluminium leads to a more exothermic mixture and therefore should facilitate the formation of $TiAlN_{1-x}O_x$ solid solution. One possible reason could be a higher oxygen affinity of aluminium compared to titanium: The energies of formation per oxygen molecule are -1055 kJ/mol for Al_2O_3 and -890 kJ/mol for TiO_2 [79]. The higher affinity of oxygen to aluminum is also reflected in the by a factor of 40 higher oxygen content in AlN precipitates than in TiN after decomposition of TiAlN [82].

Figure 2: interatomic distances and lattice parameter of $Ti_{0.5}Al_{0.5}N_{1-x}O_x$ as a function of x.

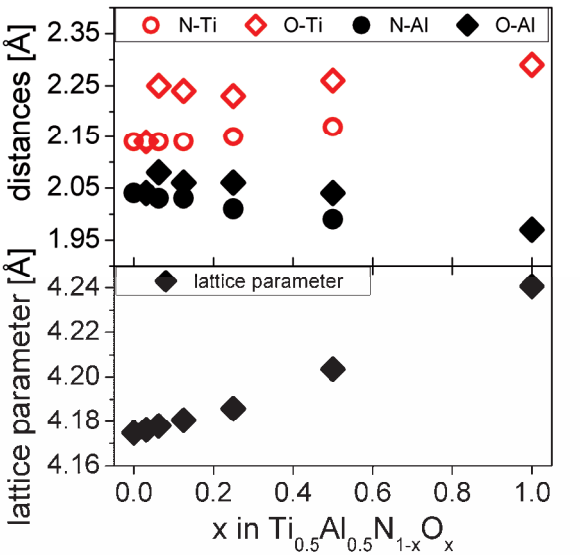

This notion is also consistent with the changes in non-metal-titanium and non-metal-aluminium bond distances as the oxygen population on the non-metal sublattice is varied. Generally, the N-Al and O-Al distances are shorter than the N-Ti and O-Ti distances, as shown in Figure 2. If the oxygen content is increased, the N-Ti bonds are enlarged while the N-Al bonds shorten. As the oxygen content x in $TiAlN_{1-x}O_x$ is increased past 0.25, the O-Ti and O-Al bond lengths increase and decrease,

respectively. The decrease in non-metal-Al bond length is not enough to compensate for the larger distance between non-metals and Ti, therefore, the lattice parameter increases from 4.175 Å to 4.241 Å with increasing x from 0 to 1. A slight negative deviation from Vegard's law [73] is observed in Figure 2 which may be due to the negative energy of mixing (cf. Figure 1).

Figure 3: total and partial density of states (DOS) of a) $Ti_{0.5}Al_{0.5}N$, b) $Ti_{0.5}Al_{0.5}N_{0.875}O_{0.125}$, c) $Ti_{0.5}Al_{0.5}N_{0.5}O_{0.5}$, d) $Ti_{0.5}Al_{0.5}N_{0.875}O_{0.219}$. Partial DOS were enlarged by a factor of 4/3 for clearer representation.

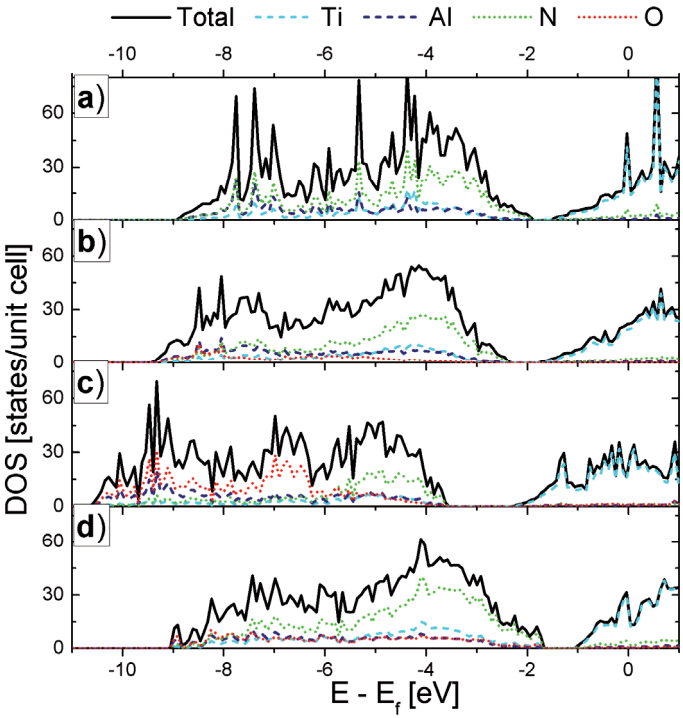

The higher affinity of aluminium to oxygen and nitrogen is also reflected in the calculated density of states (DOS). The DOS is plotted in Figure 3 for $Ti_{0.5}Al_{0.5}N$ (a), $Ti_{0.5}Al_{0.5}N_{0.875}O_{0.125}$ (b) and $Ti_{0.5}Al_{0.5}N_{0.5}O_{0.5}$ (c). For $Ti_{0.5}Al_{0.5}N$, an energy interval

between the Fermi level and -1.8 eV belonging to metallic states may be distinguished from a region belonging to covalent/ionic bonds between N and Al and Ti located between -1.9 eV and -9 eV (all energies given here and in the following text are referring to the Fermi level). The decomposition of DOS into partial density of states shows that the metallic states almost exclusively belong to Ti atoms. The integrated density of states between -1.9 eV and the Fermi level is 16 states per supercell which means that one electron per Ti atom is forming a metallic bond. This indicates that the other three valance electrons of Ti contribute to covalent bonding to nitrogen. When oxygen is introduced on the non-metal sublattice, an increase in energy difference between the hybridized states and the Fermi energy is observed, shifting the hybridized states to energies between -2.2 and -9.4 eV for $Ti_{0.5}Al_{0.5}N_{0.875}O_{0.125}$ (Figure 3b) and -3.6 and -10.6 eV for $Ti_{0.5}Al_{0.5}N_{0.5}O_{0.5}$ (Figure 3c). The metallic character due to Ti-d states increases to 20 and 32 states per supercell, respectively. Hence, two of four valance electrons of Ti are contributing to metallic bonds rather than to covalent/ionic bonds in $Ti_{0.5}Al_{0.5}N_{0.5}O_{0.5}$. This may be understood based on the fact that oxygen has six valance electrons while nitrogen has five which results in a transfer of only two valance electrons to oxygen and three valance electrons to nitrogen when covalent/ionic bonds are formed. Therefore, the substitution of nitrogen by oxygen results in a smaller number of metal valance electrons which form covalent or ionic bonds which increases the metallic character of the oxynitride. Based on the atomic radii of covalently bound O and N, which are 0.66 and 0.70 Å [102], respectively, a decrease of atomic volume would have been expected when substituting N by O. The increase in volume observed (Figure 2), can be explained by the increase in metallic character by increasing the oxygen content.

As already indicated by the smaller distance between Al and O compared to Ti and O, oxygen preferably bonds to aluminium as can be inferred from the hybridized states

between -8 and -10.6 eV in $Ti_{0.5}Al_{0.5}N_{0.5}O_{0.5}$ (Figure 3c) that belong both to O and Al. This notion is also consistent with the more negative energy of mixing (cf. Figure 1) of $Ti_{0.5}Al_{0.5}N_{1-x}O_x$ compared to $TiN_{1-x}O_x$ [100] and explains why Al does not form metallic bonds.

Figure 4: bulk modulus B as a function of x in $Ti_{0.5}Al_{0.5}N_{1-x}O_x$ and $Ti_{0.5}Al_{0.5}N_{1-x}O_{x+y}$. For comparison, the bulk modulus data reported by Graciani et al. [100] for titanium oxynitride $TiN_{1-x}O_x$ is added.

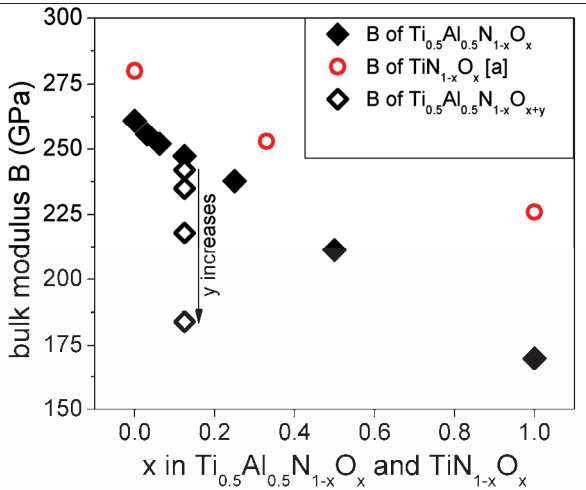

[a]: [100]

In Figure 4, the bulk modulus is shown for $TiAlN_{1-x}O_x$ together with the bulk modulus data for $TiN_{1-x}O_x$ [100]. The bulk modulus of $TiAlN_{1-x}O_x$ decreases with increasing x, showing a similar behaviour as $TiN_{1-x}O_x$. The smaller bulk modulus of TiAlO compared to TiAlN may be understood based on the increase in metallic bond character at the expense of covalent bonding with increasing x, as was deduced from the DOS (Figure 3).

3.3.2.3 Defects in $Ti_{0.5}Al_{0.5}N_{0.875}O_{0.125}$

By studying defects in $Ti_{0.5}Al_{0.5}N_{0.875}O_{0.125}$, the origin of the experimentally reported non-metal overstoichiometry [14, 98, 99] is investigated. Different configurations had to be considered here because of the complexity of the task: one Ti (Al) atom surrounded by 6 N atoms was removed, forming a Ti (Al) vacancy distant from oxygen. This was compared to a configuration where one Ti (Al) atom surrounded by 4 N atoms and 2 O atoms was removed, forming a Ti (Al) vacancy close to oxygen. Non-metal overstoichiometry may also be due to the formation of interstitials. Therefore, configurations were studied where one O atom was introduced in a tetrahedron gap with 2 Ti, 2 Al and 4 N atoms as nearest neighbours, with 2 Ti, 2 Al, 2 N and 2 O as nearest neighbours, with 4 Ti, 2 N and 2 O as nearest neighbours or with 4 Al, 2 N and 2 O as nearest neighbours, respectively. Additionally, one configuration was studied where 1 N atom was moved from a normal lattice site into a tetrahedron gap with 2 Ti, 2 Al, 2 N and 2 O nearest neighbours and one O atom simultaneously filled the N vacancy, which allows for comparison of energetics of N and O interstitials without referring to N_2 and O_2 molecules. The lattice parameter and bulk modulus of configurations containing these defects and energy of formation of these defects are listed in Table 2.

defect	a [Å]	E_f^{defect} [eV/defect]	B [GPa]
none	4.181	0	247
1 Ti vacancy close to O	4.171	0.83	241
1 Ti vacancy distant from O	4.175	1.97	240
1 Al vacancy close to O	4.175	0.65	241
1 Al vacancy distant from O	4.179	1.52	239
1 N interstitial tetrahedron gap close to 2 Ti, 2Al, 2N, 2O and 1 more O on N site	4.220	0.61	231
1 O interstitial tetrahedron gap close to 2 Ti, 2 Al, 4 N	4.216	0.73	233
1 O interstitial tetrahedron gap close to 2 Ti, 2 Al, 2 N, 2O	4.212	-0.63	239
1 O interstitial tetrahedron gap close to 4 Ti, 2 N, 2 O	4.210	-1.33	242
1 O interstitial tetrahedron gap close to 4 Al, 2 N, 2 O	4.210	-1.33	243

Table 2 - Results of calculations of one and two defects in $Ti_{0.5}Al_{0.5}N_{0.875}O_{0.125}$: Lattice parameter *a*, energy of formation per defect E_f^{defect} and bulk modulus *B*.

The energy of formation of a Ti vacancy is reduced from 2.5 eV/vacancy in $Ti_{0.5}Al_{0.5}N$ to 0.8 and 2.0 eV/vacancy in $Ti_{0.5}Al_{0.5}N_{0.875}O_{0.125}$, depending on whether the vacancy is close to or distant from oxygen. The same trend is observed for Al vacancies, indicating that oxygen significantly reduces the energy penalty for forming metal vacancies. The energy needed to incorporate oxygen into a tetrahedron gap surrounded by nitrogen is the same for $Ti_{0.5}Al_{0.5}N$ and $Ti_{0.5}Al_{0.5}N_{0.875}O_{0.125}$, 0.7 eV. There is, however, an important change if oxygen is incorporated into a tetrahedron gap with 2 N and 2 O nearest neighbours: There is no energy penalty but energy is gained, -0.6 eV if oxygen is surrounded both by Ti and Al atoms and -1.3 eV if oxygen is surrounded by only Ti or Al atoms. This is a clear indication for oxygen being spontaneously incorporated interstitially in $Ti_{0.5}Al_{0.5}N_{0.875}O_{0.125}$. Comparing the latter energies with the energy of the configuration where a nitrogen atom is moved to an interstitial site and the vacant lattice site is filled by oxygen (+0.6 eV), it is expected that only oxygen is incorporated interstitially in $Ti_{0.5}Al_{0.5}N_{0.875}O_{0.125}$. Hence,

it is proposed here that the reason for the non-metal overstoichiometry observed experimentally [14, 98, 99] is the formation of oxygen interstitials, rather than formation of metal vacancies which was proposed in [14].

An interesting question remaining to be answered is how much oxygen may be incorporated interstitially. While the solubility limit is probably a function of oxygen population on the non-metal sublattice, here, only the energetics of oxygen interstitials in $Ti_{0.5}Al_{0.5}N_{0.875}O_{0.125}$ was investigated.

Figure 5: energy of incorporation of oxygen interstitials as function of y in $Ti_{0.5}Al_{0.5}N_{0.875}O_{0.125+y}$. For comparison, energy of formation of oxygen interstitials in $Ti_{0.5}Al_{0.5}NO_y$ and $TiNO_y$ [103] was added.

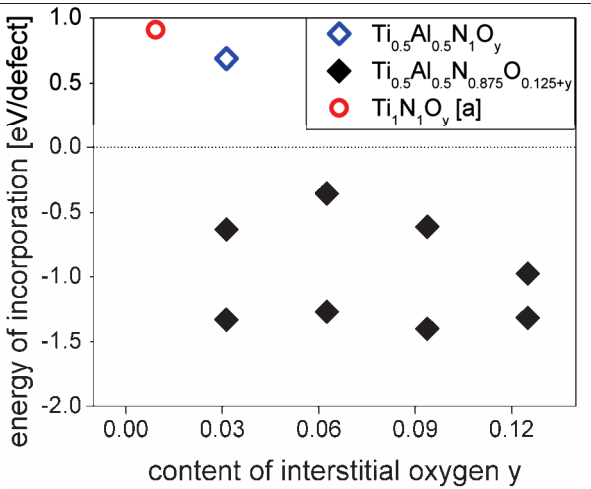

[a]: [103]

Figure 5 shows the energy of incorporation per oxygen interstitial in $Ti_{0.5}Al_{0.5}N_{0.875}O_{0.125}$ together with the data for TiAlN (cf. Table 1) and for TiN taken from Tsetseris et al. [103]. The configurations for $Ti_{0.5}Al_{0.5}N_{0.875}O_{0.125+y}$ were designed as follows: for y = 0.0625, one O atom was introduced into the configuration with lowest energy for y = 0.03125. The position of the additional oxygen atom was

chosen ad hoc in the vicinity of other oxygen atoms, where two configurations were tested. This procedure was repeated up to y = 0.125. As can be seen in Figure 5, the energy of incorporation is constant up to $Ti_{0.5}Al_{0.5}N_{0.875}O_{0.25}$. This indicates that at least the same number of oxygen atoms can be incorporated interstitially as oxygen atoms populate non-metal sublattice sites. Whether or not this is a general rule as well as the magnitude of the solubility limit of interstitial oxygen will be addressed in future work.

Interstitially incorporated oxygen reduces the bulk modulus as also shown in Figure 4. As y in $Ti_{0.5}Al_{0.5}N_{0.875}O_{0.125+y}$ increases from 0 to 0.125, B decreases from 247 GPa to 184 GPa. This is probably due to the increased unit cell volume (+10% for that change in y) which leads to bond elongation. This change in unit cell volume could also be a direct way to provide experimental evidence for the interstitially incorporation of oxygen as it can be directly measured by X-ray diffraction.

The increased stability of $Ti_{0.5}Al_{0.5}N_{0.875}O_{0.125+y}$ over $Ti_{0.5}Al_{0.5}N_{0.875}O_{0.125}$ + y/2 O_2 may be understood based on the DOS of $Ti_{0.5}Al_{0.5}N_{0.875}O_{0.219}$ shown in Figure 3d. Compared to $Ti_{0.5}Al_{0.5}N_{0.875}O_{0.125}$, the interstitial oxygen leads to a significant reduction of the metallic character (14 states per supercell compared to 20) combined with an increase in Ti states corresponding to covalent Ti-N bonds between -3 and -5 eV. Additionally, the average distances between O and both Al and Ti in $Ti_{0.5}Al_{0.5}N_{0.875}O_{0.125+y}$ are reduced from 2.06 Å and 2.24 Å (y=0) to 1.97 Å and 2.02 Å (y=0.094), respectively. These values are very similar to the ones observed in α-Al_2O_3 and rutile-TiO_2, which are 1.87 Å (1.98 Å) [2] and 1.95 Å (1.98 Å) [104] for the first (second) nearest neighbours, respectively. This may also contribute to the high stability of interstitially incorporated oxygen.

3.3.3 Implication: Design of Hard Coatings

Based on the oxygen incorporation induced stability increase of $Ti_{0.5}Al_{0.5}N_{1-x}O_{x+y}$, a new design concept for transition metal oxynitride based hard coatings is proposed in the following. Efficient hard coatings for e.g. cutting applications have to be stable even at high temperatures that evolve during service. Here, TiAlN is attractive even though it is not energetically stable due to kinetic limitation of the decomposition. Additionally, the decomposition of fcc-TiAlN into fcc-TiN and w-AlN is spinodally in the beginning, leading to high hardness of TiAlN coatings due to formation of fcc-TiN and fcc-AlN rich domains that act as obstacles for dislocation movement [91, 105]. One way to increase the kinetic limitation of decomposition could be to introduce oxygen into the system causing the formation of $TiAlN_{1-x}O_y$. While it was shown that there is no energetic limitation for the oxygen incorporation, an indication for the impact of oxygen on the decomposition kinetics can be found in [82], where after annealing of TiAlN at 900°C only a slight segregation of oxygen impurities into AlN rich regions was observed. Only after annealing to 1350°C, i.e. after the cubic to hexagonal transformation of AlN, oxygen mobility is high enough to lead to significantly different oxygen contents in TiN and AlN of 0.004 at.% and 0.16 at.%, respectively [82]. This shows that the solubility limit of oxygen in TiN is extremely small, therefore, it is feasible that oxygen and nitrogen will diffuse simultaneously with the metals, forming TiN-rich and AlO-rich regions. Thus, oxygen may act on aluminum similar to the solute drag effect [106]: As the mobility of oxygen is smaller than that of the metals, substantial incorporation of oxygen may decrease the diffusivity of aluminum and therefore lead to an increase in decomposition temperature. This would be technologically important as it would lead to a sustained high hardness at temperatures above the h-AlN formation temperature during the

decomposition of TiAlN. This design concept will in the future be evaluated experimentally.

3.3.4 Summary

The impact of oxygen additions on phase stability and elastic properties of titanium aluminium nitride was studied by ab initio calculations. Fcc-$Ti_{0.5}Al_{0.5}N$ and fcc-$Ti_{0.5}Al_{0.5}O$ shows a negative energy of mixing with an interaction parameter Ω_{TiAlNO} of -37.6 kJ/mol. The lattice parameter of $Ti_{0.5}Al_{0.5}N_{1-x}O_x$ increases with increasing x while the bulk modulus decreases by 35%. The reason for this is the metallic bonding character which increases on the expense of covalent bonds with increasing oxygen content. In contrast to $Ti_{0.5}Al_{0.5}N$ it has been shown that the incorporation of oxygen in $Ti_{0.5}Al_{0.5}N_{1-x}O_x$ on interstitial sites is energetically favourable. This can be understood based on the compensation of metallic bonding as the population of metal-oxygen bonds that are similar to α-Al_2O_3 and rutile-TiO_2 is increased. Based on the oxygen incorporation induced stability increase of $Ti_{0.5}Al_{0.5}N_{1-x}O_{x+y}$, a new design concept for transition metal oxynitride based hard coatings is developed.

3.4 Reactive gas gradients

3.4.1 Introduction

Reactive magnetron sputtering is often used to synthesize stable as well as metastable phases by sputtering of a metal target in reactive gas atmosphere (e.g. N_2 or O_2). Using two or more metal targets, lateral metal concentration gradients can be achieved and the influence of metal composition on properties of e.g. oxides or nitrides can be studied by spatially resolved methods. This method is called combinatorial magnetron sputtering [16]. To date, a method where lateral non-metal concentration gradients can be achieved by magnetron sputtering has not been reported. However, it is known that gas phase gradients can be used in atmospheric pressure chemical vapor deposition (CVD) [107]. Combinatorial CVD has been used in few cases to study TiO_xN_y [108], VO_xN_y [109] and $Ti_xW_yO_2$ [110]. Combinatorial CVD uses localized gas inlets where a gas is introduced into the reactor at the vicinity of one end of a substrate while other reactive gases are homogeneously distributed [107]. To the best of the author's knowledge, a similar approach has not been reported to date for reactive magnetron sputtering besides some experiments in the late 1980s and early 1990s: van Zon et al. pointed out that gas gradients exist during reactive magnetron sputtering and can be substantial: a 4.5 times larger O_2 partial pressure was measured 20 cm away from the substrate center than in the substrate centre [111]. Vossen et al. applied a gas inlet localized on the substrate to study the efficiencies of different oxygen containing gases to produce oxides [112]. A similar experimental setup was used by Niwa et al. to estimate the flux ratio of oxygen molecules to tantalum atoms needed to form Ta_2O_5 [113]. Here, it is shown that reactive gas gradients can be used for combinatorial reactive magnetron sputtering to study the effect of off-stoichiometry in nitrides or oxides. As study

systems, TiN_x and TiO_y have been analyzed by EDX, XRD and Nanoindentation. For $TiAlN_x$ and $TiAlN_xO_y$, only initial EDX and XRD results are reported and discussed here. In the following text, the reported distance always refers to the distance from the gas inlet along the target surface.

3.4.2 Experiments

3.4.2.1 Deposition of TiN_x

Optical inspection of the deposited film (a photograph is provided in Figure 1) showed golden colour close to the N_2 gas inlet changing to grey at a distance of ~15 cm. This can be understood by considering the EDX data shown in Figure 1.

Figure 1: Photograph of the TiN_x samples and the corresponding EDX results.

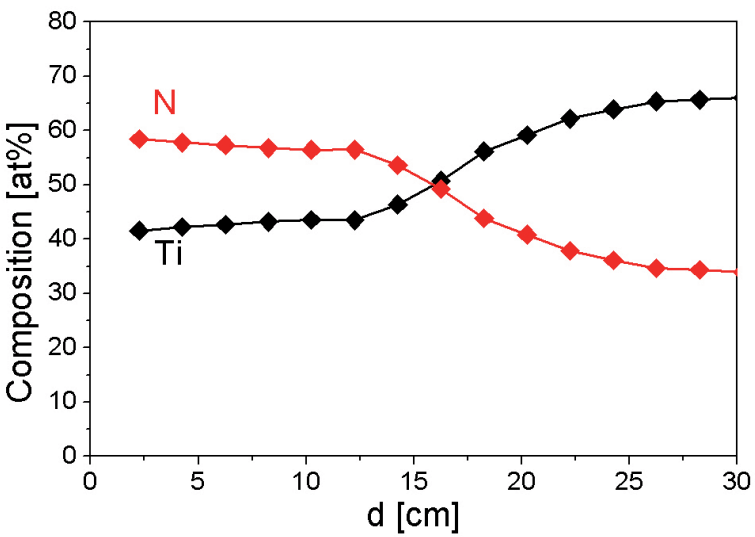

The nitrogen content in the film measured by EDX decreases slightly up to a distance of ~12 cm and strongly between 12 and 24 cm from the gas inlet. The relation between nitrogen content and colour has been described before and optical results of the films deposited in this work are in good agreement with the data shown in [114]. It should be noted that Si, Na, O and other glass additives were detected in varying concentrations in the EDX spectra due to low film thickness. Therefore and because of limited reliability of EDX for light elements, the Ti and N contents shown in Figure 1 can only be discussed qualitatively. It may be that the decrease in N:Ti ratio between 0 and 12 cm does only reflect a thickness gradient leading to different information depths (the intensity of the Si signal decreases from 790 counts to 146 counts between 0 and 12 cm, indicating larger film thickness), hence this decrease is not discussed further. Between 12 and 24 cm, however, the change in N:Ti ratio can be correlated to large changes in thin film composition (the intensity of the Si signal decreases only from 146 counts to 27 counts between 12 and 24 cm, indicating rather constant film thickness). This indicates that reactive gas gradients can be used for combinatorial reactive magnetron sputtering. The diffractograms taken at selected distances are shown in Figure 2. Due to the incidence angle of 15° and the integration width of +10 ° and -10 ° in tilting, the (111) planes detected are tilted by 3.3 ° to 10.5 ° from the surface normal and the (200) planes detected are tilted by 6.3 ° to 11.8 °. Even for fibre textured samples, a significant fraction of grains is commonly misaligned by 5-10 ° from the surface normal [115, 116], therefore, the intensities of the (111) and (200) planes are a good indication of the texture of the film. It can be observed that a (111) fibre texture is dominant at all distances but ~14 cm from the gas inlet. Here, the (200) peak becomes dominant. It is interesting to note that the transition from an (over-)stoichiometric to an understoichiometric nitride is also at this distance. This could indicate that the stoichiometry of the

growing film is another decisive factor for texture evolution. It may be argued that (111) terminated nuclei are energetically favoured if the Ti:N ratio is different from unity as then closed packed planes of Ti (Ti:N > 1) or N (Ti:N < 1) can be formed while a (100) plane would include surface vacancies.

Figure 2: XRD results of TiN_x samples taken at selected distances from the N_2 inlet.

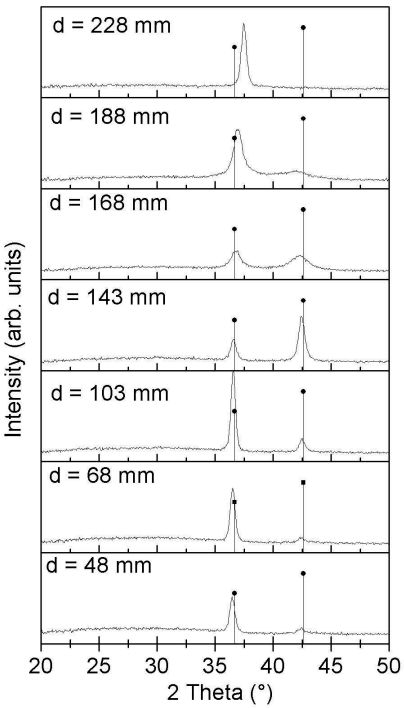

A slight peak shift can be observed in Figure 2 as well that can be related to a decreasing lattice parameter with increasing distance from the N_2 gas outlet. As stresses may evolve in the film and change with composition, the lattice parameter was not determined. Only small changes in reduced modulus and hardness were determined by nanoindentation and the influence of changing film thickness on these

could not be determined. Therefore, the nanoindentation results are not shown here for brevity.

3.4.2.2 Deposition of TiO_y

A photograph of the Ti target after sputtering is shown in Figure 3. In the enlarged part with increased contrast, arc spots can be distinguished. The arc spot density exhibits a maximum at around 17 cm.

Figure 3: Photograph of the Ti target after sputtering with O_2 gas phase gradient (up) and the same photograph enlarged and with decreased brightness and increased contrast (down). The numbers indicate the distance from the O_2 gas inlet in [cm].

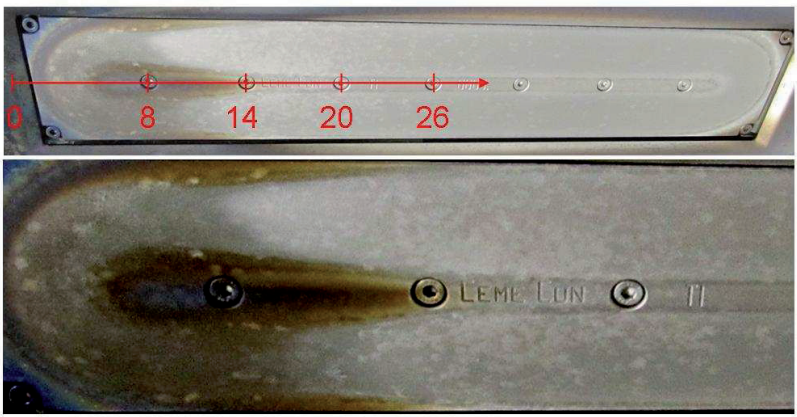

The EDX results and a photo of the TiO_y samples are shown in Figure 4. At distances smaller 7 cm, the film was too thin to analyze by EDX and the data points are omitted. At distances larger 23 cm the sample is essentially Ti with small amounts of oxygen that could not be quantified by EDX.

Figure 4: Photograph of the TiO_y samples and the corresponding EDX results.

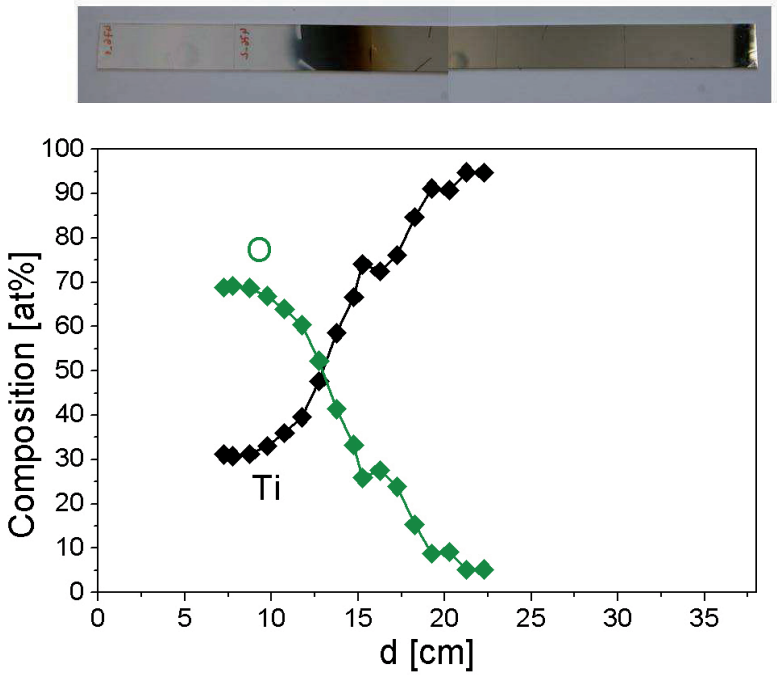

It can be seen that the film is transparent up to a distance of ~10 cm. At this distance, the O:Ti ratio concurrently drops to values smaller than 2 and a transition from dark grey to metallic appearance can be observed at the target shown in Figure 3 indicating the transition from a poisoned to a metallic target. The gradient in composition is significantly steeper than for TiN_x which can be explained based on (I) the by a factor of 2 larger Ar partial pressure, resulting in a factor of 2 smaller mean free path, (II) a higher reactivity of oxygen compared to nitrogen and (III) the fact that two oxygen are bonded to one Ti atom in TiO_2 while only one nitrogen atom is bonded to one Ti atom for TiN.

The XRD data is shown in Figure 5 as a contour plot.

Figure 5: Contour plot of XRD intensities of TiO_y samples taken at spacings of 10 mm.

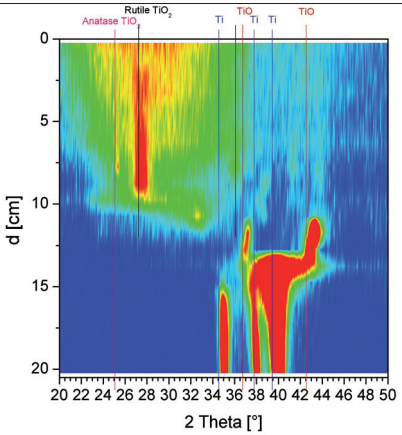

In Figure 5, five regions can be distinguished: From 0 to 9 cm from the O_2 inlet, Rutile and Anatase TiO_2 can be observed (the amorphous hump that is seen between 22 ° and 34 ° at 0 to 7 cm results from the glass substrate). At 11 cm from the O_2 outlet, peaks are observed at 2Θ of 32.6 ° and 38.7 °. These could stem from Ti_2O_3 (104) and (006) planes, for which the diffraction angles are 33.0 ° and 39.5 ° according to JCPDS card No. 10-0063. Textured growth of isostructural Cr_2O_3 with the basal plane parallel to the surface was reported when floating bias potential was used [117, 118] which could explain the sole occurrence of (104) and (006) peaks for Ti_2O_3 observed here. Between 12 cm and 13 cm from the O_2 outlet, cubic TiO is observed with a peak shift towards smaller 2Θ angles with increasing distance. Between 13 cm and 15 cm, a broad hump is observed between 38 ° and 43 ° 2Θ which indicates an amorphous or nanocrystalline TiO_y phase with $y < 1$. With decreasing oxygen content, the hump sharpens and hexagonal Ti is detected. The results from Nanoindentation

measurements of hardness and reduced modulus with loads of 500 μN and 1000 μN are shown in Figure 6, where the stability regions of the phases are also marked.

Figure 6: Hardness and reduced modulus of the TiO_y films. The phases formed are included for clearer representation.

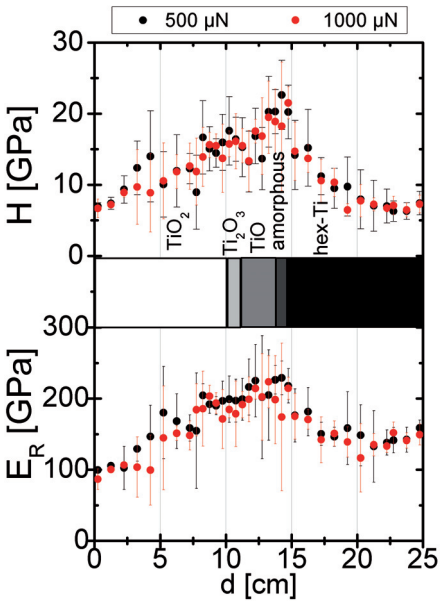

Close to the O_2 gas outlet, the film is too thin leading to smaller hardness and modulus values at a force of 1000 μN compared to 500 μN. The largest hardness of 20 GPa is observed for the amorphous TiO_y phase qualifying it as a hard phase [119]. For the hexagonal Ti with dissolved oxygen, hardness and reduced modulus decrease with increasing distance from the gas inlet. This may be due to larger grain size -as can be speculated from the decrease in XRD peak broadening between 15 cm and 17 cm- combined with a decreasing solute hardening effect of interstitial oxygen.

These results show the power of reactive gas gradients as a combinatorial approach for exploring the phase space of oxides or nitrides. In principle, it is expected that the approach can be transferred to other reactive gases. In the proof-of-concept reported here, a new hard amorphous phase with composition TiO_y ($y < 1$) was observed. Additionally, this new combinatorial approach can be expanded easily from binary to ternary and quaternary systems as is shown in the next two sections.

3.4.2.3 Deposition of $TiAlN_x$

Experiments were conducted similar to those reported in section 3.4.2.1 using a TiAl target. The EDX results are shown in Figure 7.

Figure 7: Composition of $TiAlN_x$ films as function of the distance from the N_2 inlet measured by EDX.

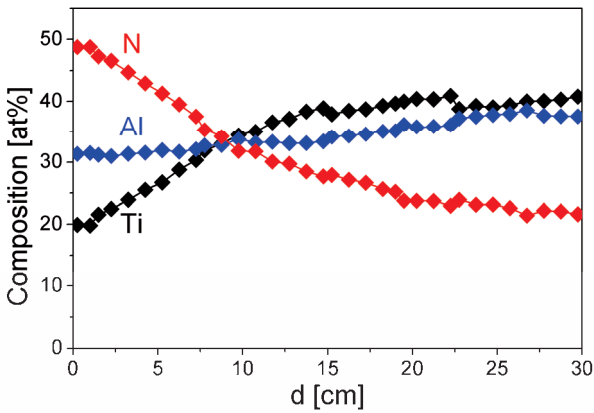

In contrast to TiN_x, the nitrogen content in the film decreases constantly which could be either due to increased power at the target when working with the same set voltage or a larger sputter rate of aluminum and hence faster consumption of N_2. Unfortunately, the peak current and voltages at the target were not measured. Additionally, it can be observed that the Ti:Al ratio changes with distance. This

indicates different poisoning behavior of Ti and Al. Different poisoning (and -to be more precise- sputtering, scattering, sticking) behavior will limit the applicability of gas phase gradients for combinatorial deposition of ternary phases when using compound targets.

In Figure 8, XRD results are shown for selected $TiAlN_x$ films with decreasing nitrogen content.

Figure 8: XRD results of selected $TiAlN_x$ films. On the right, the 2Θ range of the (111) peak is enlarged for clearer visibility of the peak shift observed.

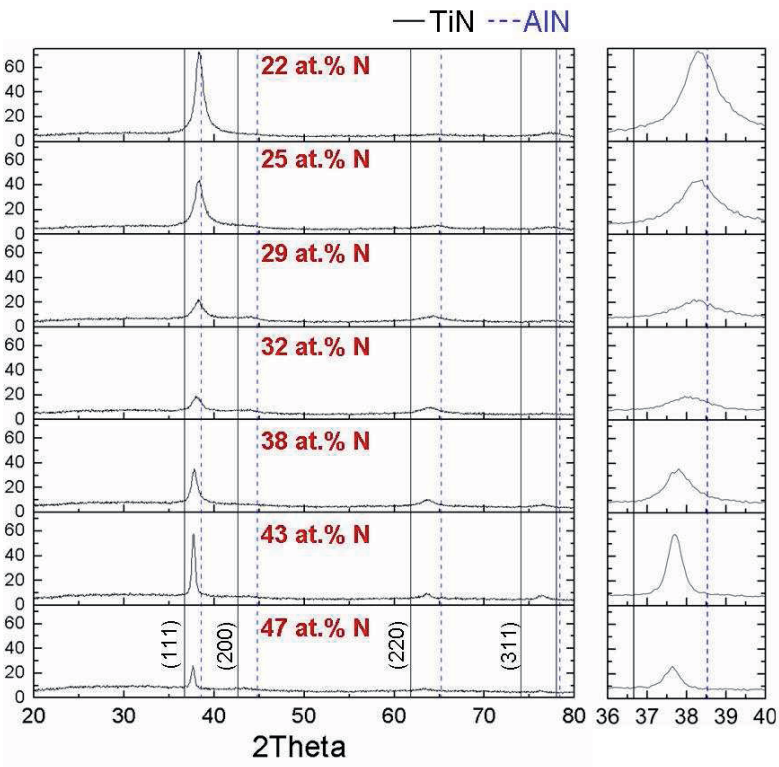

It is interesting to note that the all peaks detected can be attributed to a NaCl structure, indicating a high metastable solubility limit for N vacancies of the already metastable phase TiAlN. In the enlarged 2Θ range shown on the right of Figure 8, a peak shift to larger 2Θ angles and an increase of the peak width can be seen that may be interpreted as smaller lattice spacings and smaller grains or non-uniform strains, respectively.

In the following, the lattice parameter is obtained from the peak position in Figure 8, thus assuming that the stress does not change significantly with changing N content. A more precise analysis should include strain correction as well as N content determination by a method with higher accuracy than EDX. The lattice parameters obtained are shown in Figure 9.

Figure 9: Lattice parameters obtained from the (111), (220) and (311) XRD peak position as a function of N content.

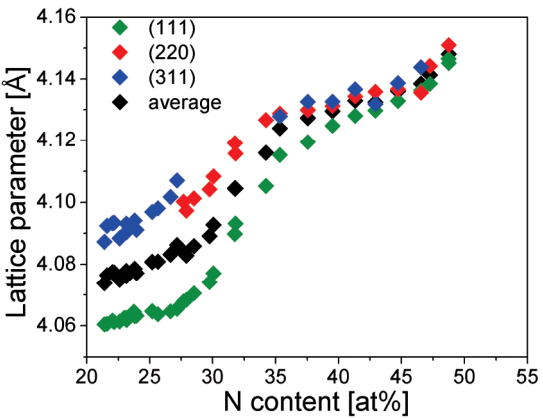

The lattice parameters obtained from the (111), (220) and (311) peaks show a similar change with nitrogen content. Therefore, the average lattice parameter was calculated and used for comparison with ab initio data. As shown in Figure 7, the

Ti:Al ratio changes with N content. As this will affect the lattice parameter [41], the change of the Ti:Al ratio was compensated for by using a second order polynomial fit through the data shown in Figure 2 of [41]. The resulting lattice parameters are shown in Figure 10 together with the data from Figure 2 in section 3.2.2.

Figure 10: Lattice parameters obtained experimentally using a N_2 gradient in comparison to the experimental data reported by Shew et al. [87] and the ab initio data reported in section 3.2.2.

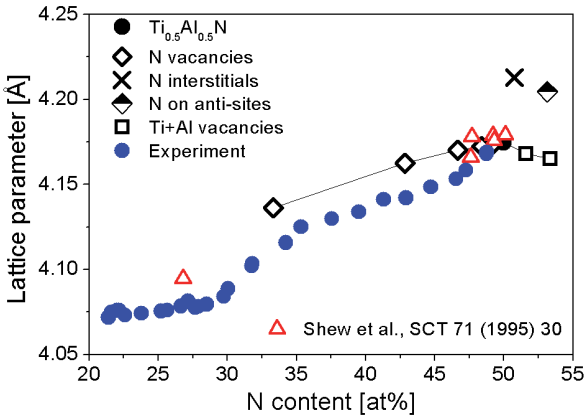

Good agreement is observed between the experimental and the calculated lattice parameter of $TiAlN_x$ for the whole composition range calculated with deviations smaller 0.5 %. At nitrogen contents of 35 at.% and 30 at.% changes in slope are observed which may be due to lattice distortion, stresses or phase transformations. An advantage of combinatorics by gas phase gradients over individual experiments is immediately visible in Figure 10: In the report by Shew et al., six growth experiments were conducted to determine the relationship between lattice parameter and N content [87] while only one growth experiment was required using a N_2 gradient. Furthermore, the data point density is clearly higher using the combinatorial setup.

3.4.2.4 Deposition of $TiAlN_xO_y$

The variation of Ti:Al ratio with nitrogen due to different poisoning behavior indicated already one limitation for the combinatorial setup. To explore whether two reactive gases could be used in the same setup and what would be the resulting composition gradient, N_2 was introduced in the deposition chamber together with Ar homogeneously and O_2 was let in through the gas inlet located on top of the elongate target. EDX results of the films are shown in Figure 11.

Figure 11: Composition of $TiAlN_xO_y$ films as function of the distance from the O_2 inlet measured by EDX.

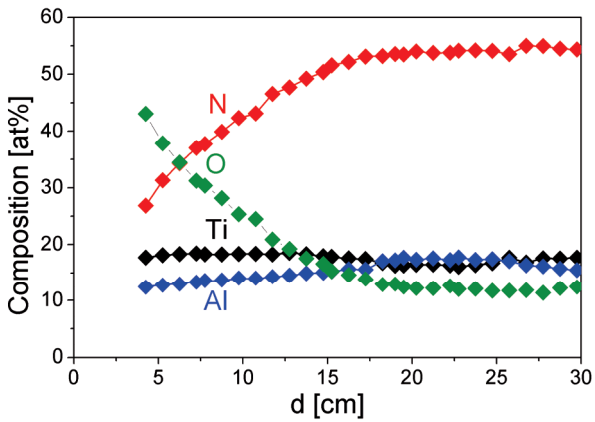

As expected the O content in the film decreases with distance from the O_2 inlet. At distances below 3 cm, the film was too thin for a meaningful analysis by EDX. With decreasing O content the N content as well as the Al:Ti ratio increase due to a transition from an oxidic to a nitridic poisoned target. It is interesting to note that the O content is slightly increasing at a distance of 27 cm from the gas inlet with concurrently decreasing N content and Al:Ti ratio. Selected diffractograms of $TiAlN_xO_y$ are shown in Figure 12.

Figure 12: XRD results of selected $TiAlN_xO_y$ films. On the right, the 2Θ range of the (200) peak is enlarged for clearer visibility of the peak shift observed.

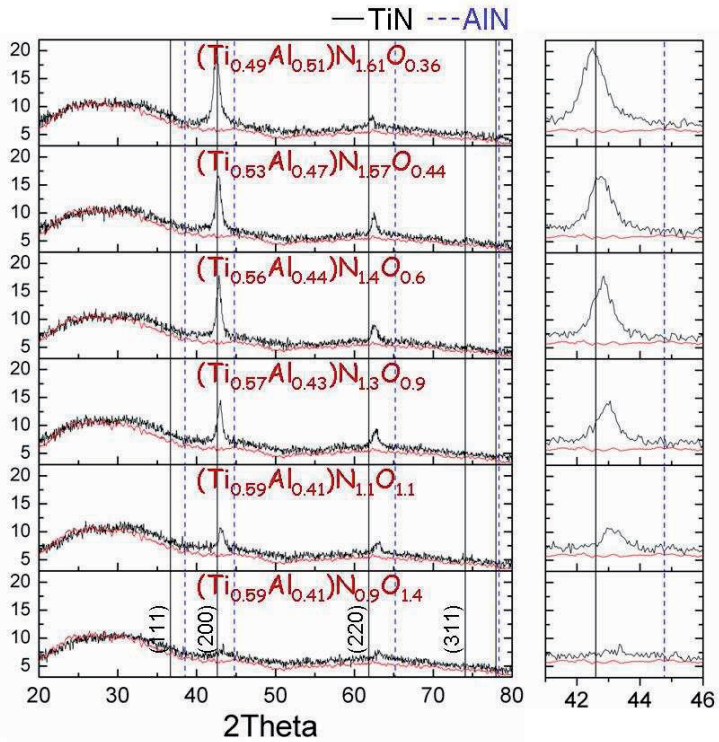

The O-rich films show poor crystallinity while with larger N content the (200) peak intensity of a NaCl structured phase is increased, indicating textured growth. In the enlarged 2Θ range shown on the right of Figure 12, a peak shift to smaller 2Θ angles -even lower than the peak position for TiN- is observed. This may be an indication of increasing lattice parameter to values larger than 4.24 Å. Decomposition of TiAlN during deposition was reported at substrate temperatures larger 540 °C, which is significantly larger than the 370 °C maximum substrate temperature used here. Therefore, decomposition into Ti- and Al-rich regions is not likely during deposition

and the reason for the increased lattice parameter is probably oxygen incorporation. As shown in Figure 2 of section 3.3.2.2, the lattice parameter increases when oxygen substitutes nitrogen in TiAlN. However, for an O:(O+N) ratio of 0.18 (upmost diffractogram in Figure 11), a lattice parameter of only 4.18 Å is expected based on the ab initio data for substitutional oxygen incorporation, which is significantly smaller than the value derived from the lattice spacing of the (200) peak of 4.246 Å. The difference may be due to stresses or interstitial oxygen incorporation as suggested in section 3.3.2.3. For clarification, further experiments are needed.

3.4.3 Implication: Gas phase combinatorics

The results shown above indicate that gas phase combinatorics can be used for several purposes:

1. Binary composition spread: The metal to gas ratio arriving at the substrate and thus the composition can be varied continuously to study the composition-structure-property relationship.
2. Multinary composition spread: Using a binary target or several reactive gases the composition can be varied continuously, however, the cut through the multinary phase space is not a straight one due to changing poisoning behavior.
3. Arc control: Counting the number of arc spots on the target after deposition, the connection between reactive gas partial pressure and arcing behaviour could be studied in a single deposition.

3.4.4 Summary

Reactive gas gradients were used to deposit TiN_x, TiO_y, $TiAlN_x$ and $TiAlN_xO_y$ thin films with varying x and y in a single deposition. Using EDX, XRD and Nanoindentation it was shown that reactive gas gradients can be used to synthesize films with lateral composition gradients and to study their composition-structure-properties relationship. A new amorphous or nanocrystalline hard TiO_y ($y < 1$) phase was observed as well as an increase of the (200) lattice spacing of $TiAlN_xO_y$ that may indicate interstitial oxygen incorporation.

3.5 Elastic properties of nanolaminates

3.5.1 Introduction

Of all the material characteristics, the bulk modulus is one of the most fundamental, reflecting the mean bond strength. The bulk modulus is therefore not only a measure of the elastic properties but can also be correlated, for example, to hardness [120], the activation energy for self diffusion [121] and thermal properties, e.g. melting temperature [122] or Debye temperature [123]. Experimental bulk moduli are measured with a diamond anvil cell, a nanoindenter or instruments for velocity-of-sound analysis. Much effort has been invested in compiling simple models for fast and efficient determination of bulk moduli, allowing for the estimation of bulk moduli based on atomic distances [124], lattice energy densities [125] or plasmon energy [126] for simple phases. Also, bulk modulus data is readily available from *ab initio* calculations using DFT [24, 30] within an accuracy of ~20% [127]. Although calculation speed increased considerably in the last years and will increase further, the calculation of crystals with large unit cells or supercells is still a challenging task since computational time scales with the number of electrons to the power of three.

Phases with layered crystal structure -here referred to as nanolaminates [55]- generally exhibit large unit cells. One example for nanolaminates systematically studied in this work are the $M_{n+1}AX_n$ phases (M designates transition metal, A is IIIA or IVA group element, X stands for C or N, and n =1-3). They may be described as phases consisting of n MX layers interleaved with one MA layer [55]. $M_{n+1}AX_n$ (henceforth MAX) phases exhibit both metallic and ceramic properties such as large elastic moduli [50, 54, 128], oxidation resistance [59], thermal and electrical conductivity [54] as well as damage tolerance [129]. As previously reported, the bulk

moduli of MAX phases can be correlated to the one of the corresponding MX binary in NaCl structure [128, 130, 131].

Further investigations have been performed on $M_nAl_4C_{n+3}$ phases (where M is Hf or Si and n = 1-3) using solely data published by others [132, 133] and on the cyanide $KAg(CN)_2$. The latter was chosen as an extreme case to test the validity of the methodology proposed here. $KAg(CN)_2$ is known to dissociate into $Ag(CN)_2^-$ and K^+ in aqueous solutions [134] and exhibits a significant ionic contribution to bonding, that is expected to cause errors in Madelung energy when long-range interactions are omitted [102].

3.5.2 Theory

Based on the properties of the constituting phases the rule of mixture (ROM) allows for estimating a variety of composite properties ranging from the heat capacity of ivory [135] to effective Young's modulus of concrete [136]. For the calculation of the bulk modulus, for example, the only input data needed are the bulk moduli of the constituting phases and their volume fractions. This approach is commonly adopted to describe macroscopic composites [137] as well as multilayers, with layer thicknesses of a few nanometers [138]. The applicability of the rule of mixture on smaller length scales, i.e. on the atomic level has not been considered. In the following section, the to the sub unit-cell level extended rule of mixture for the calculation of the bulk modulus *B* of nanolaminates is derived. The elastic energy $E^{elastic}$ is a quadratic function of the strains [102] at the equilibrium volume V^0. Therefore, assuming uniform deformation, the total energy of a crystal can be written as follows:

$$E^{total} = E^{elastic} + E^0 = k \cdot \left(\frac{dV}{V^0} \right)^2 + E^0, \qquad (1)$$

where E^0 is the ground state energy of the undeformed crystal, and k is a measure for the energy needed for deformation, i.e. the elastic response of the crystal. This means, knowing the second derivative *k* of the total energy with respect to relative volume change $\frac{dV}{V^0}$ yields important information on the elastic properties, e.g. the bulk modulus, which may be seen in Eq. (2):

$$B = V^0 \frac{d^2E^{total}}{dV^2} = \frac{1}{V^0}\frac{d^2E^{total}}{\left(\frac{dV}{V^0}\right)^2} = \frac{2k}{V^0} \quad (2)$$

Given a laminate made of two binary phases AB and AC with a one to one stoichiometry and the repeating period *λ*, the total energy of the compound may be calculated from:

$$E_{comp}^{total} = E_{AB}^{total} + E_{AC}^{total} + E^{interact}(\lambda), \quad (3)$$

where $E^{interact}(\lambda)$ is the interaction energy between AB and AC in the compound as a function of *λ*.

While long-range interactions are crucial for the crystal stability - as can be seen by the stability difference between the hexagonal closed packed and face centered cubic crystal structures - the elastic properties may be described on the basis of short-range interactions, as can be seen from the independence of Young's moduli of carbon nanotubes on tube radius and chirality [139, 140] or from the possibility to estimate bulk moduli on the basis of nearest neighbor distances [124]. Therefore, the contribution of interaction energy to elastic energy may be considered negligible and the elastic energy of the compound may be estimated from a superposition of the elastic energies of its constituents. Thus, the bulk modulus of the compound may be calculated using an extended rule of mixture (EROM):

$$B_{comp} = \frac{1}{V_{comp}^0}\frac{d^2E_{comp}^{total}}{\left(\frac{dV}{V^0}\right)^2} = \frac{1}{V_{comp}^0}\left(\frac{d^2E_{AB}^{total}}{\left(\frac{dV}{V^0}\right)^2} + \frac{d^2E_{AC}^{total}}{\left(\frac{dV}{V^0}\right)^2}\right) = \frac{1}{V_{comp}^0}\left(V_{AB}^0 B_{AB} + V_{AC}^0 B_{AC}\right) \quad (4)$$

Using the approximation, that the volume of the compound is the sum of the volumes of its constituents, what is true for compounds on the macroscopic scale, Eq. (4) results in the classical rule of mixture (ROM):

$$B_{ROM} = \frac{\sum V_i^0 B_i}{\sum V_i^0} \quad (5)$$

The most important requirement for dividing nanolaminates into smaller constituents is that the coordination number of nearest neighbors has to be conserved, in order to take all nearest-neighbor interactions into account. Therefore, the $M_{n+1}AX_n$ phase unit cell (see Figure 1 *(b)* for n= 1) can be divided into two binary phases MX and MA in such a way that the coordination number and arrangement of neighboring atoms for X and A is conserved, as can be seen in Figure 1 *(a)* and 1 *(c)*, respectively.

Figure 1: Unit cells used for calculation: binary carbide MX in TiAs-structure *(a)*, ternary phase M_2AX *(b)* and binary MA in WC-structure *(c)*. The MX octahedron is marked in light green, the MA trigonal prism in purple.

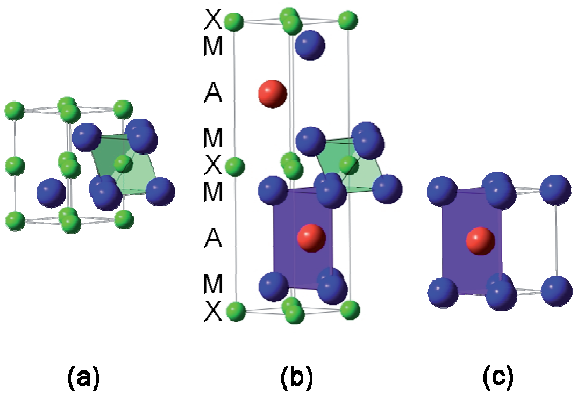

This procedure results in the TiAs structure for MX and WC structure for MA. Using this description, M-X and M-A interactions are considered as well as all interactions within M, A and X layers. The methodology is evaluated by comparing to data obtained by *ab initio* for the whole cell in the following sections.

3.5.3 Evaluation: Bulk moduli of Nanolaminates

In Figure 2, the elastic energy per formula unit (f.u.) of CrAl (WC structure), CrC (TiAs structure) and Cr_2AlC is plotted versus relative volume change in the interval of ±1%. The dashed, dotted and solid lines in Figure 2 are parabolic fits using Eq. (1) for CrAl, CrC and Cr_2AlC with k being 12.96, 17.71 and 31.34 eV/f.u., respectively. The dotted-dashed line is a superposition (i.e. $k_{superpos} = k_{CrAl} + k_{CrC}$) of the elastic-energy-fits for CrAl and CrC.

Figure 2: The elastic energy per formula unit of CrAl, CrC and Cr_2AlC plotted versus relative volume change. The solid line and the dotted-dashed line coincide.

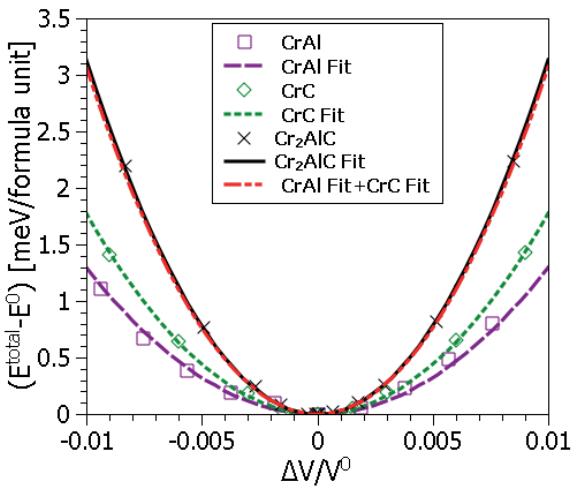

This line coincides well with the fit function of Cr_2AlC (solid line). The bulk moduli calculated from k using Eq. (2) are 156, 340 and 225 GPa for CrAl, CrC and Cr_2AlC,

respectively. Using the superposition of CrAl and CrC, the bulk modulus of Cr_2AlC is 220 GPa, which is with a 2% difference in excellent agreement. Hence, the methodology appears valid for Cr_2AlC. The computational time per calculated elastic energy per formula unit using one processor was 34 s, 130 s and 931 s for CrAl, CrC and Cr_2AlC, respectively. Thus, the computational time was reduced by over 80% using the here proposed methodology.

The lattice parameter, hexagonal aspect ratio, volume per formula unit *V* and bulk modulus *B* of the binary phases calculated in this work are given in Table 1.

Phase	a (Å)	c/a	V (Å³/f.u.)	B (GPa)
ScC	3.444	1.451	25.7	157
ScAl	3.236	1.427	41.9	67
TiC	3.156	1.501	20.4	245
TiAl	2.891	1.599	33.5	106
TiSi	2.924	1.406	30.4	136
VC	2.962	1.612	18.1	296
VAl	2.771	1.581	29.1	141
CrC	2.782	1.791	16.7	330
CrAl	2.694	1.565	26.5	162
CrSi	2.705	1.415	24.3	200
YC	3.730	1.468	33.0	123
YAl	3.592	1.388	51.0	53
ZrC	3.464	1.461	26.3	218
ZrAl	3.148	1.507	40.7	93
NbC	3.186	1.615	22.6	293
NbAl	2.931	1.599	34.9	140
MoC	3.011	1.758	20.8	340
MoAl	2.875	1.527	31.4	174
HfC	3.314	1.593	25.1	236
HfAl	3.127	1.498	39.7	102
TaC	3.153	1.661	22.5	317
TaAl	2.926	1.597	34.7	153

WC	2.996	1.798	20.9	371
WAl	2.824	1.619	31.6	192
Al4C3	---	---	---	165 [132]
HfC	---	---	---	267 [132]
α-SiC	3.036 [133]	9.936 [133]	19.8 [133]	226 [133]

Table 1: Lattice parameter a and aspect ratio c/a of the unit cell, volume per formula unit V and bulk modulus B of binary phases MC, MA and SiC [133] and bulk moduli of Al_4C_3 [132] and HfC [132].

The volume per formula unit and theoretical bulk modulus values of the MAX phases studied are provided in Table 2, as well as the bulk modulus calculated with Eq. (4) using the bulk moduli of the binary phases.

MAX phase	V_{MAX} (Å³/f.u.)	V_{ROM} (Å³/f.u.)	B_{MAX} (GPa)	B_{ROM} (GPa)	B_{EROM} (GPa)
Sc_2AlC	71.6 [141]	67.6	99 [141]	101	95
Ti_2AlC	55.8 [7]	53.9	160 [7]	159	153
Ti_3AlC_2	74.3	74.3	182	182	176
Ti_3SiC_2	73.4 [131]	71.2	187 [131]	198	193
V_2AlC	48.4 [7]	47.2	202 [7]	200	196
Cr_2AlC	44.7 [7]	43.2	221 [7]	227	220
Cr_3AlC_2	59.9	59.9	246	256	245
Cr_4AlC_3	79.6	76.6	263	272	262
Cr_2SiC	42.7	41	243	253	243
Y_2AlC	177.6	84	80	81	77
Zr_2AlC	70.1 [7]	67	144 [7]	142	136
Nb_2AlC	58.8 [7]	57.5	203 [7]	200	197
Mo_2AlC	54.3 [7]	52.2	232 [7]	240	231
Hf_2AlC	67.0 [7]	64.8	159 [7]	154	149
Ta_2AlC	57.8 [7]	57.2	222 [7]	218	215
W_2AlC	53.5 [7]	52.5	262 [7]	263	259

Table 2: Volume per formula unit V_{MAX} and bulk modulus B_{MAX} of MAX phases as obtained directly from energy-volume curves and volume per formula unit V_{ROM} and bulk modulus B_{ROM} calculated from rule of mixture and B_{EROM} calculated from the extended rule of mixture.

Figure 3 shows the linear dependence between B_{EROM} as well as B_{ROM} and B_{MAX} for all MAX phases investigated here. The maximum deviation of values calculated via extended rule of mixture as well as via the classical rule of mixture from the ones obtained directly from DFT is 6 %. This indicates that the bulk modulus of $M_{n+1}AX_n$ phases can be obtained from the values for the binary MA and MX phases alone using both the extended rule of mixture and the rule of mixture.

Figure 3: The bulk moduli of different MAX phases calculated from corresponding binaries MC and MA via the extended rule of mixture B_{EROM} and from the rule of mixture B_{ROM} plotted versus the bulk moduli calculated directly by DFT B_{MAX}. The straight line is a guide to the eye with $B_{ROM} = B_{MAX}$.

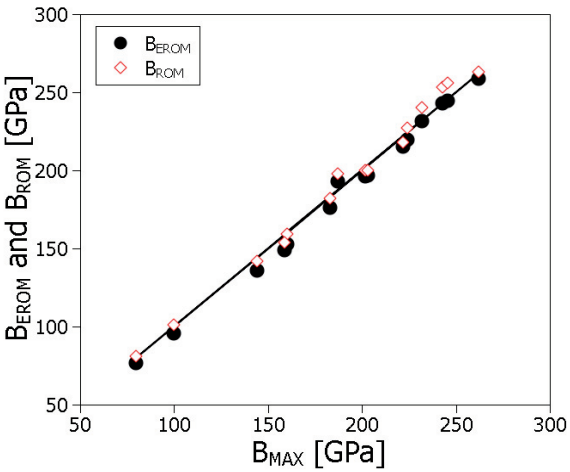

As from one combination of MA and MX bulk moduli of three different $M_{n+1}AX_n$ phases can be calculated, the reduction on computational time is even larger than the above mentioned 80%. Considering again the calculation time in the $Cr_{n+1}AlC_n$ system, the computational time per calculated elastic energy per formula unit using one processor was 3623 s and 7667 s for Cr_3AlC_2 and Cr_4AlC_3, respectively, which accounts to a 99% time reduction for bulk modulus calculation of $Cr_{n+1}AlC_n$ phases

using the methodology proposed here. Furthermore, nanolaminated phases usually possess internal free parameters that have to be relaxed, which also is not necessary using this methodology.

The methodology was tested further on the nanolaminated carbides $Hf_3Al_4C_6$, $Hf_2Al_4C_5$ and Al_4SiC_4 consisting of Al_4C_3 and HfC or SiC slabs, respectively, using already published data [132, 133]. Table 3 gives the bulk moduli and constituent's volume fractions for these compounds.

Phase	B (GPa)	$V_f^{Al_4C_3}$	V_f^{HfC} / V_f^{SiC}	B_{ROM} (GPa)
$Hf_3Al_4C_6$	213 [132]	0.506	0.494	215
$Hf_2Al_4C_5$	206 [132]	0.605	0.395	205
Al_4SiC_4	179 [133]	0.793	0.207	178

Table 3: Bulk moduli *B* of $Hf_3Al_4C_6$, $Hf_2Al_4C_5$ and Al_4SiC_4 as well as volume fractions of Al_4C_3 ($V_f^{Al_4C_3}$) and HfC/SiC (V_f^{HfC} / V_f^{SiC}) in the ternary carbides.

The bulk moduli reported in references [132, 133] are 213, 206 and 179 GPa, respectively. Using the data given in Tables 1 and 3, the bulk moduli calculated from ROM are 215, 205 and 178 GPa, respectively, and therefore within 1% deviation of the ones directly obtained from *ab initio* calculations [132, 133]. This indicates that for these three phases the rule of mixture is also sufficient to calculate the bulk modulus.

The applicability of the rule of mixture may be limited by the properties of the boundary layer between the constituents. By dividing the unit cell in such a way that an atomic layer, which is part of both constituents, forms the boundary between them, all nearest neighbor interactions are included. In the MAX phase system, the boundary layer is the M element, while carbon forms the boundary layer in the ternary carbides studied in the previous section. The rule of mixture is expected to result in larger deviations when charge transfer becomes important, i.e. for compounds containing ionic bonds. To identify a limiting case, the nanolayered

cyanide $KAg(CN)_2$ was investigated using *ab initio* calculations. The crystal structure of $KAg(CN)_2$ is shown in Figure 4.

Figure 4: Unit cell of $KAg(CN)_2$. Three ways of dividing into building blocks are marked: $AgC+KN_2C$ (left), $KN+AgC_2N$ (middle) and KN+NC+AgC (right).

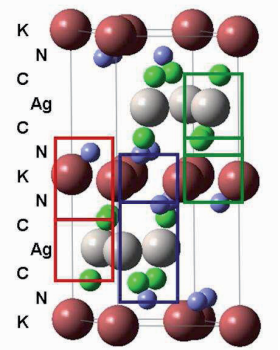

Due to the layer sequence K-N-C-Ag-C-N-K, $KAg(CN)_2$ may be divided into constituting building blocks in three different ways, as marked in Figure 4 in red, blue and green, respectively: AgC and KN_2C; KN and AgC_2N; KN, NC and AgC. Hence, the atoms in the boundary layers are carbon, nitrogen and nitrogen as well as carbon, respectively. Table 4 gives the calculated data for $KAg(CN)_2$ and the phases which may be considered constituents, i.e. KN_2C, AgC_2N, KN, NC and AgC.

Phase	V (Å³/f.u.)	B (GPa)	effective charge per atom			
			K	Ag	C	N
$KAg(CN)_2$	440.9	56	+0.88	+0.40	+0.74	-1.38
KN_2C	229.1	69	+0.87	---	+1.43	-1.15
AgC_2N	359.8	57	---	+0.51	+0.52	-1.55
KN	135.8	28	+0.78	---	---	-0.78
NC	142.9	79	---	---	+1.23	-1.23
AgC	131.6	56	---	+0.37	-0.37	---

Table 4: Volume per formula unit *V*, bulk modulus *B* and effective charges of each atom for $KAg(CN)_2$, KN_2C, AgC_2N, KN, NC and AgC.

$KAg(CN)_2$ is known to dissociate into $Ag(CN)_2^-$ and K^+ [134], so an ionic bond is expected between potassium and the cyanide. According to Bader decomposition[31, 32], the effective charge of potassium is between +0.8 and +0.9 -depending on the phases considered-, which is close to +1, being the formal charge expected. The sum of the constituents' volumes V_{ROM} is 410 Å³/f.u. (KN+NC+AgC), 361 Å³/f.u. (KN_2C+AgC) and 496 Å³/f.u. (AgC_2N+KN), respectively. For comparison, the values V_{ROM} are included in Figure 5.

Figure 5: Sum of constituents volumes V_{ROM} for MAX phases as well as $KAg(CN)_2$ plotted versus the volume of the compound. For $KAg(CN)_2$, the volume was divided by 5 in order to compare the relative changes in volume with the MAX phases.

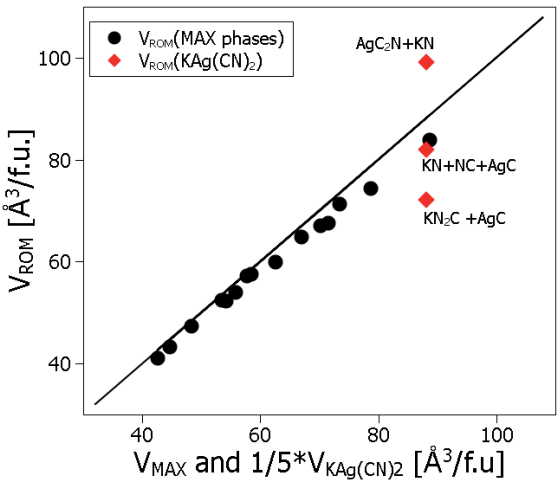

It can be seen that the difference between V_{ROM} and the volume of the compound is larger than in the case of the MAX phases, with deviations of -18% to +12%, so using the classical rule of mixture would result in larger deviations because of volume differences.

Using the extended rule of mixture yields the following values for the quaternary's bulk modulus, depending on the constituting building blocks considered: 51 GPa (KN+NC+AgC), 53 GPa (KN_2C+AgC) and 56 GPa (AgC_2N+KN), while the values from the rule of mixture are 54 GPa, 64 GPa and 49 GPa, respectively. The values from the extended rule of mixture are within 9% deviation of the bulk modulus for $KAg(CN)_2$ of 56 GPa and therefore in excellent agreement, while the rule of mixture leads to deviations up to 14% due to the large volume differences.

3.5.4 Implementation: DFT combinatorics

These results are significant because they enable the prediction of elastic properties of "sub unit-cell composite" materials based on a combination of DFT and combinatorial materials science. This approach may be useful to guide the design process of materials with tailor-made properties. Thus, this knowledge-based approach may replace the trial-and-error methods designing nanolaminates, reducing the computational time requirement by some orders of magnitude.

As an example for DFT combinatorics, bulk moduli of 78 $M_{n+1}AX_n$ phases have been estimated based on the binary constituents for n = 1-3; M = Sc, Ti, V, Cr, Y, Zr, Nb, Mo, Hf, Ta, W; A= Al, Si (for M = Ti and Cr); X = C, N and are shown in Table 5. Where available, comparison from *ab initio* calculations of the whole cell has been given, as well as bulk moduli calculated from published data for MX in NaCl structure (where M has the same coordination number as in TiAs structure) [142].

M-A elements	calculation method	B (M_2AC)	B (M_3AC_2)	B (M_4AC_3)	B (M_2AN)	B (M_3AN_2)	B (M_4AN_3)
Sc-Al	B_{ROM}-this work B_{ROM}-NaCl B_{MAX}	101 100 100, 88 [143], 99 [141]	117 114	125 123	113 107[143]	135	148
Ti-Al	B_{ROM}-this work B_{ROM}-NaCl B_{MAX}	158 158 138 [143], 160 [7]	182 181 182, 159 [144]	196 194 172 [144]	164 155 [143], 181 [130]	191 177 [144]	206 199 [144]
V-Al	B_{ROM}-this work B_{ROM}-NaCl B_{MAX}	201 203 175 [143], 202 [7]	227 231	242 247 255 [145]	205 180[143], 215[130]	235	251
Cr-Al	B_{ROM}-this work B_{ROM}-NaCl B_{MAX}	227 225 224, 186 [143], 221 [7]	256 252 246	272 268 263	225 184[143], 249[130]	252	267
Y-Al	B_{ROM}-this work B_{ROM}-NaCl B_{MAX}	81 83 80, 78 [146]	93 95	100 103	92	110	120
Zr-Al	B_{ROM}-this work B_{ROM}-NaCl B_{MAX}	142 143 125 [143], 144 [7]	164 165	176 178	151 141 [143], 155 [130]	178	193
Nb-Al	B_{ROM}-this work B_{ROM}-NaCl B_{MAX}	200 203 173 [143], 203 [7]	226 231	241 246 247 [145]	205 194 [143], 209 [130]	233	250
Mo-Al	B_{ROM}-this work B_{ROM}-NaCl B_{MAX}	241 239 196 [143], 232 [7]	269 267	285 283	234 229 [130]	260	275
Hf-Al	B_{ROM}-this work B_{ROM}-NaCl B_{MAX}	154 155 138[143], 159[7]	177 178	190 191	164 158 [143], 171 [130]	192	209
Ta-Al	B_{ROM}-this work B_{ROM}-NaCl B_{MAX}	217 220 193	245 249 250	261 266 264	220 217	250	267

		[143], 222 [7]	[147]	[147]	[143], 234 [130]		
W-Al	B_{ROM}-this work B_{ROM}-NaCl B_{MAX}	263 261 214 [143], 262 [7]	294 291	311 307	256 251 [143], 273 [130]	284	299
Ti-Si	B_{ROM}-this work B_{ROM}-NaCl B_{MAX}	180 179 179, 167 [148]	199 197 197, 187 [131]	209 207 209, 245 [149]	186	208	220
Cr-Si	B_{ROM}-this work B_{ROM}-NaCl B_{MAX}	253 251 243	276 272 234 [131]	288 283	250	271	283

Table 5: Bulk moduli of $M_{n+1}AC_n$ and $M_{n+1}AN_n$ phases calculated in different ways: Using the rule of mixture approach as proposed in this work with MA and MX data input from Table 1 (*B_{ROM}-this work*); using the rule of mixture approach as proposed in this work with MA data input from Table 1 and MX data input from calculations of MX in cubic NaCl structure taken from Isaev et al. [142] (*B_{ROM}-NaCl*); *ab initio* calculations of the whole cell (*B_{MAX}*).

The results from rule of mixture calculations of bulk moduli show very good agreement with the existing *ab initio* data for the whole cell for both approaches: In Figure 6, the bulk moduli data from ROM are compared with the data from references [7, 130, 131, 141, 143-149]. Larger deviations up to 19% are observed when comparing with Cover et al. [143]. This may be explained by the fact that in [143] the bulk modulus was obtained by a fit through stress-volume data obtained from relaxation calculations, whereas in the other references included in Figure 6 as well as in this work energy-volume data from static calculations have been considered.

Figure 6: The bulk moduli B_{MAX} of 34 different MAX phases calculated directly by DFT plotted versus the corresponding bulk moduli B_{ROM} calculated by DFT combinatorics from binaries MX [142] and MA via the rule of mixture. The straight line is a guide to the eye with $B_{ROM} = B_{MAX}$.

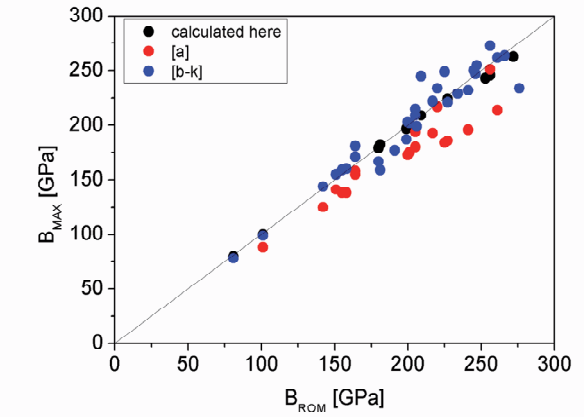

[a]: [143] [b-k]: [7, 130, 131, 141, 144-149]

3.5.5 Evaluation: Elastic Constants of Nanolaminates

As it was shown above, the average of the nearest-neighbor interactions determines the resistance against isotropic elastic deformation. However, it was proposed that shear resistance of some MAX phases is determined by MC-MC coupling [51, 128, 150, 151]. The applicability of the extended rule of mixture for calculation of the bulk modulus indicates that this coupling does not contribute to the stiffness of MAX phases or is simply another description of the M-A interaction which is consistent with [128, 150]. To evaluate the influence of coupling on shear resistance, the elastic constants were calculated based on lattice distortions [40] for Ti_2AlC, V_2AlC and Cr_2AlC and for the binary constituents. The values for the MAX phases are compared to the values calculated by the extended rule of mixture. It should be noted that CrAl was metastable in the WC structure so that it was not possible to obtain values for

C_{11}, C_{12} and C_{66}. Additionally, elastic constants of other $M_{n+1}AlC_n$ phases with M = Ti, V, Cr and n = 1-3 are compared to values obtained from the extended rule of mixture. All the data is plotted in Figure 7 for the different elastic constants. The dashed lines indicate a 30 % deviation from the extended rule of mixture values, which is the accuracy of elastic constant calculations [40].

Figure 7: Elastic moduli of $M_{n+1}AlC_n$ phases with M = Ti, V, Cr and n = 1-3 calculated based on lattice distortions [40] as a function of the extended rule of mixture value from elastic constants of MAl and MC. The solid line is a guide to the eye with C_{ij} = ROM value and the dashed line marks the deviation of +/- 30 % which is reported as accuracy of elastic constant calculations [40].

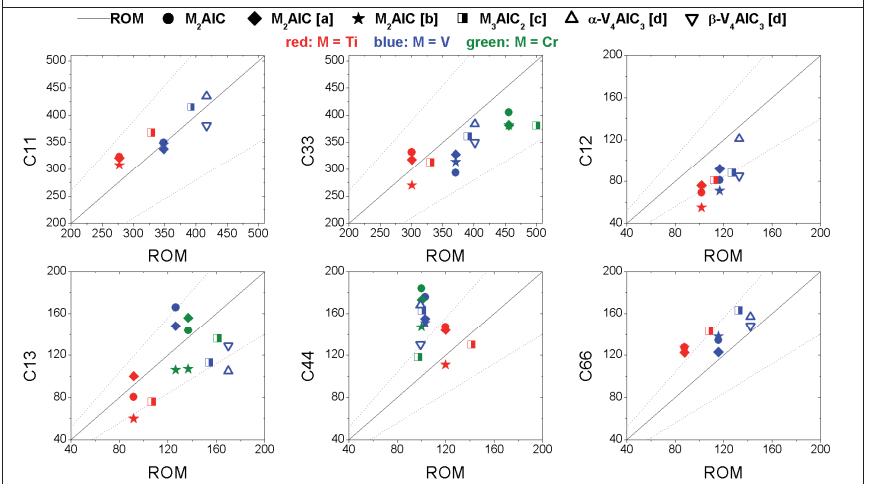

[a]: [51] [b]: [50] [c]: [152] [d]: [153]

First, it should be noted from Figure 7 that the accuracy of +/- 30 % [40] is a reasonable number considering the ratios of highest to lowest value of individual elastic constants of Ti_2AlC calculated here and in [50, 51] which are 1.3, 1.4 and as large as 1.7 for C_{44}, C_{12} and C_{13}, respectively.

As can be seen in Figure 7, the extended rule of mixture-values for C_{11} and C_{33} are within the 30 % accuracy of ab initio calculations. This can be understood based on the fact that the related deformations are symmetry conserving and volume changing and thus similar to the calculation of bulk moduli.

For the elastic constants related to shear in the basal plane, C_{12} and C_{66} (which is defined as $(C_{11}-C_{12})/2$), systematic deviations -but still within or close to the 30 % accuracy- are observed: C_{66} is underestimated by the extended rule of mixture while C_{12} is overestimated (which is a consequence of C_{66} being underestimated and C_{11} showing reasonable agreement). This could be due instability of the hypothetical phases as it was observed for the binary CrAl in the WC phase.

For C_{44} and C_{13}, which are the elastic constants related to shear perpendicular to the basal plane, larger deviations can be observed. Considering C_{44} it can be seen that the extended rule of mixture leads to a reasonable estimation for Ti_2AlC but large underestimation (50 to 80%) for V_2AlC and Cr_2AlC. By analysis of the electronic structure shear resistant bands coupling the MC layers across the MAl layer have been identified which are empty for Ti_2AlC but filled for V_2AlC and Cr_2AlC [151]. Regarding the otherwise reasonable agreement of estimations from extended rule of mixture, it can be argued that the boost in shear resistance of V_2AlC and Cr_2AlC is due to MC-MC coupling and hence in good agreement with references [51, 128, 150, 151].

When increasing n in $M_{n+1}AlC_n$ from 1 to 2, it is interesting to note that C_{44} is strongly reduced for $Cr_{n+1}AlC_n$ (approaching the extended rule of mixture value) while it is conserved for $V_{n+1}AlC_n$, indicating that VC-VC coupling is still active in V_3AlC_2. For V_4AlC_3, the α and β phases have to be considered. Based on the comparison to the extended rule of mixture values VC-VC coupling is only observed in α-V_4AlC_3, which is the more stable configuration. The reason for this is not understood to date.

In summary, the elastic constants C_{11} and C_{33} can be described by the extended rule of mixture for $M_{n+1}AlC_n$ phases with M = Ti, V, Cr and n = 1-3. However, the predictive power for the other elastic constants is rather weak. Especially, when considering that the formation of shear resistant bands [151] is disregarded when using the extended rule of mixture, which may lead to strong underestimation of elastic constants. It should also be kept in mind that the constituting phases may be unstable with respect to a lattice distortion, thus making it impossible to obtain the elastic constants. Additional elastic constant calculations for MAX phase constituents and other nanolaminates, e.g. the $M_nAl_4C_{n+3}$ phases, may be needed for a more conclusive evaluation of the extended rule of mixture.

3.5.6 Evaluation: Bulk Moduli of Solid Solutions

Alloying pure phases is a routine concept for materials design [2-4, 8-11]. Alloying can lead to formation of a second phase, in which case the classical extended rule of mixture is commonly applied for prediction of the elastic properties. If the alloying agent is soluble, a solid solution is formed, where the applicability of the extended rule of mixture is not known. Therefore, the applicability of the extended rule of mixture is tested for the phases of interest to this thesis in the following.

In Figure 8, the bulk moduli for solid binary solutions of M_2AlC phases for the transition metals Ti, V and Cr taken from [154] are plotted against the values calculated via extended rule of mixture from the boundary phases. The same was done for $Ti_{1-x}Al_xN$, $TiAlN_{1-x}$ and $TiAlN_{1-x}O_x$. In the case of $Ti_{1-x}Al_xN$ the lattice parameters and bulk moduli reported in [41] were used as input for the extended rule of mixture. For $TiAlN_{1-x}$, the extended rule of mixture was used with TiAlN and hypothetical fcc-TiAl (V = 66.8 Å³, B = 100 GPa) as boundary phases and for $TiAlN_{1-x}O_x$ TiAlN and TiAlO.

Figure 8: The bulk moduli B_{calc} of solutions calculated directly by DFT plotted versus the corresponding bulk moduli B_{ROM} calculated from the boundary phases via the extended rule of mixture. The straight line is a guide to the eye with $B_{calc} = B_{ROM}$.

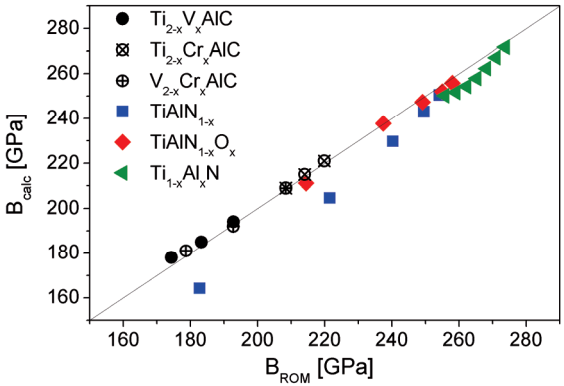

For the MAX phase solutions, excellent agreement between bulk modulus calculated by DFT [154] and extended rule of mixture is observed with deviations smaller than 2%. Similarly small differences of up to 3% are present for the mixtures $Ti_{1-x}Al_xN$ [41] and $TiAlN_{1-x}O_x$. Even if the bulk modulus is interpolated between TiAlN and fcc-TiAl, i.e. a mixture on the non-metal sublattice between nitrogen and vacancies, is considered, the maximum deviation is 11% for a mixture of each 50% nitrogen atoms and vacancies and hence still in reasonable agreement. It should also be noted that the bulk moduli of TiAlN and TiAl are with 259 and 100 GPa different by a factor of 2.6 which is a large number for a solid solution. The pure phases for the other solid solutions plotted in Figure 8 exhibit bulk moduli that are different by factors between 1.1 and 1.5. Additionally, the boundary phases of the $TiAlN_x$ solid solution exhibit completely different bonding: metal-nitrogen bonds in TiAlN and metallic bonding in TiAl. Thus, the reasonable agreement for this extreme case of solid solutions renders

the extended rule of mixture useful for knowledge based design of solid solutions, even if the boundary phases are hypothetical and extremely different in bonding and, hence, stiffness.

3.5.7 Summary

In summary, the rule of mixture has been extended to the sub unit-cell level for the estimation of the bulk modulus. It is shown how the theoretical bulk modulus of a single phase with layered crystal structure is reliably estimated from calculated bulk moduli data of the constituents adopting the symmetry within the individual layers of the layered structure. This is method was tested for the example of 16 MAX phases, 3 $M_nAl_4C_{3+n}$ phases and $KAg(CN)_2$ and excellent agreement with existing *ab initio* data is observed. Thus, a high throughput methodology based on a combination of DFT and combinatorial materials science was developed which allows for prediction of the elastic properties of “sub unit-cell” composite materials: a database containing a variety of hypothetical phases which are building blocks of the layered structure was created. Suitable combinations of these building blocks constitute the “sub unit-cell composite”, reducing calculation time by some orders of magnitude. This work is a significant step towards knowledge-based materials design since the elastic properties of “sub unit-cell composite” materials can be predicted based on an efficient high throughput methodology. Additionally, the applicability of the extended rule of mixture for estimation of bulk moduli of solid solutions was shown. For elastic constants of $M_{n+1}AlC_n$ with M = Ti, V, Cr and n = 1-3, the extended rule of mixture values are in good agreement for C_{11} and C_{33} and overestimate C_{12}. The elastic constants related with shearing out of the basal plane are in good agreement for M = Ti, however, MC-MC coupling leads to increased shear resistance of V and Cr containing $M_{n+1}AlC_n$ phases.

4 Conclusions

In this thesis, oxygen incorporation in M_2AlC phases and TiAlN was studied. It is shown that oxygen interstitials play an important role for both material systems since they are spontaneously formed when oxygen is present. While oxygen is incorporated substitutionally in Ti_2AlC and V_2AlC, it is argued that oxygen is incorporated interstitially in Cr_2AlC due to the larger ability of atomic and electronic relaxation upon carbon vacancy formation. The different oxygen incorporation sites may be significant for the initial stages of oxidation and may therefore enable different oxide formation mechanisms, i.e. preferential nucleation of titanium and vanadium oxides in Ti_2AlC and V_2AlC, respectively, and nucleation of aluminium oxide in Cr_2AlC.

When oxygen substitutes nitrogen in TiAlN, the additional formation of oxygen interstitials becomes energetically favoured. The reason for interstitial oxygen incorporation in TiAlNO is the increase of metallic bonding character when nitrogen is replaced by oxygen. The latter may be understood based on the fact that oxygen has six valance electrons while nitrogen has five which results in a transfer of only two valance electrons to oxygen and three valance electrons to nitrogen when covalent/ionic bonds are formed. Therefore, the substitution of nitrogen by oxygen results in a smaller number of metal valance electrons which form covalent or ionic bonds which increases the metallic character of the oxynitride. Experimental validation of the presence of oxygen interstitials in TiAlNO is missing to date and is thus one of the most important tasks for future work. Initial results from sputtering TiAl in Ar-N_2-O_2 atmosphere with gas gradients indicate the formation of a phase in NaCl structure with a (200) lattice spacing measured under Bragg-Brentano condition larger than that of TiN. Whether this is due to formation of oxygen interstitials or

stresses remains an open question. The possible process window in which TiAlNO with oxygen interstitials could be formed is probably narrow, as increasing the temperature too much will lead to de-mixing. TiAlNO may be technologically interesting as diffusion processes will be heavily altered due to chemistry change upon substitutional and interstitial incorporation of oxygen as well as the large increase in lattice parameter upon significant incorporation of oxygen interstitials. Therefore, oxygen incorporation may be a new variable to affect the technologically important decomposition of TiAlN.

It was shown that titanium and aluminium clustering is taken place in TiAlN already in the as deposited state [155, 156], so it may be expected that the oxygen distribution is not homogeneous. Based on the atomic distance and density of state data in chapter 3.3.2.2, oxygen is bonded preferably to aluminium in TiAlNO while titanium forms metallic bonds. This may have a similar impact on oxidation as it was discussed for M_2AlC phases: the nucleation of aluminium oxide may be facilitated and formation of otherwise observed titanium oxide [81] may be suppressed.

As already indicated above, the potential of reactive gas gradients for combinatorial thin film deposition was evaluated in order to test the predictions made. N_2 and O_2 gas gradients were used to deposit TiN_x, TiO_y, $TiAlN_x$ and $TiAlN_xO_y$ thin films with varying x and y in a single deposition. It is shown that reactive gas gradients can be used to synthesize films with lateral composition gradients and to study their composition-structure-properties relationship. A new amorphous or nanocrystalline hard TiO_y ($y < 1$) phase is reported as well as an increase of the (200) lattice spacing of $TiAlN_xO_y$ that may indicate interstitial oxygen incorporation.

In the last part of the thesis it is shown how the theoretical bulk modulus of a single phase with layered crystal structure is reliably estimated from calculated bulk moduli data of the constituents adopting the symmetry within the individual layers of the

layered structure. Thus, a high throughput methodology based on a combination of DFT and combinatorial materials science was developed which allows for prediction of the elastic properties of “sub unit-cell” composite materials: a database containing a variety of hypothetical phases which are building blocks of the layered structure was created. Suitable combinations of these building blocks constitute the “sub unit-cell composite”, reducing calculation time by some orders of magnitude. This work is a significant step towards knowledge-based materials design since the elastic properties of “sub unit-cell composite” materials can be predicted based on an efficient high throughput methodology.

These conclusions show how quantum mechanical calculations can enable knowledge-based materials design: Studying the energetics of oxygen incorporation by DFT calculations several interesting implications have been identified, e.g. the potential of oxygen for the design of new TiAlNO based hard coatings or the possible role of interstitial oxygen for the initial oxidation of Cr_2AlC. Now, key experiments can be done to test the predictions made, as it was shown for the case of oxygen incorporation in Cr_2AlC (c.f. chapter 3.1). Further experiments are described in the future work section of this thesis.

With the extended rule of mixture bulk moduli of sub unit-cell composites and solid solutions can be estimated. Hence, lengthy DFT calculations to obtain bulk moduli can be omitted and bulk modulus databases as shown for the MAX phases can be built. Also, this rule may be used to predict unknown or explain experimentally measured elastic modulus data of mixtures by interpolation between two known boundary phases.

5 Future work

Based on the conclusions drawn above, several directions for future work are possible. It has been shown that nitrogen and metal vacancies are present in off-stoichiometric $TiAlN_x$. Hence, the decomposition of $TIAlN_x$ should be studied experimentally for $x < 1$ as well as $x > 1$. For understoichiometric $TiAlN_x$ ($x < 1$), the decomposition pattern has been calculated, however, the influence of off-stoichiometry on decomposition kinetics is still unknown.

It was shown that additional oxygen is incorporated interstitially in $TiAlN_{0.875}O_{0.125}$, at least up to $TiAlN_{0.875}O_{0.25}$. To contribute towards a better understanding of the effect of the defect structure on the phase stability of $TiAlN_{1-x}O_{x+y}$ large ranges of x and y should be studied experimentally. Part of the explanation for the high stability of $TiAlN_{0.875}O_{0.25}$ was based on the number of valence electrons. This argument would predict highest stability for $TiAlN_{1-x}O_{1.5*x}$ as this leads to the same number of metal valance electrons bonded to nitrogen and oxygen as in TiAlN. If $TiAlN_{1-x}O_{x+y}$ in NaCl structure can be formed experimentally, the mechanical properties and thermal stability should be studied to test the materials design concept for hard $TiAlN_{1-x}O_{x+y}$ coatings described in chapter 3.3.3, which is based on proposed decreased diffusivity of the metals due to a solute drag effect, assuming that oxygen hinders diffusion of the metals in $TiAlN_{1-x}O_{x+y}$. Additionally, the oxidation resistance of $TiAlN_{1-x}O_{x+y}$ should be investigated experimentally to determine whether oxygen in the as deposited film changes the oxidation products and thus kinetics. As it was argued in the conclusions, preferential formation of Al-O bonds in the as deposited state may lead to preferential formation of aluminum oxides instead of titanium oxides, thus decreasing the oxidation speed due to lower diffusivities in Al_2O_3 compared to TiO_2.

Initial experimental results [157] indicate the formation of an amorphous oxynitride phase when sputtering Ti and Al in nitrogen and oxygen atmosphere. Therefore, an interesting extension of the calculations reported above would be to study phase stability of an amorphous titanium aluminum oxynitride phase with varying nitrogen to oxygen ratio. DFT calculations of amorphous are possible today [6, 158, 159] and are done according to the following recipe: Annealing an ad hoc structure at temperatures significantly higher than the melting temperature followed by quenching to 0 K and subsequent relaxation [158]. Comparing the energies of formation to the ones obtained for $TiAlN_{1-x}O_{x+y}$, a crossover may be obtained where the amorphous phase is more stable than the crystalline phase in NaCl structure. By comparing this crossover to the composition of the experimentally observed amorphous phase, it may be concluded whether the formation of amorphous titanium aluminum oxynitride is due to energetic or kinetic reasons. If kinetic limitations are dominant for the formation of the amorphous phase, the influence of oxygen on surface diffusivity could be studied by ab initio calculations similar to the ones reported for TiN [160]. Thus, recommendations for changing experimental parameters, e.g. using bias voltage or changing Ar, O_2 and N_2 partial pressures or substrate temperature, could be made.

Oxygen incorporation mechanisms in MAX phases should be studied further to check whether it is a general rule that substitutional oxygen incorporation is connected to formation of M oxides while interstitial oxygen incorporation in the A layer leads to A oxides. If it is a general rule, quantum mechanically guided design of oxidation resistant Ti_2AlC may be possible: Based on ab initio calculations, alloying elements may be identified that reduce the energy of formation of interstitial oxygen or that increase the energy for substitutional oxygen in Ti_2AlC. This alloying scenario may then suppress the formation of TiO_2 during oxidation as Ti-O bonds are avoided in

the MAX phase and thus the oxidation speed may be reduced. Additionally, oxygen incorporation in other well-studied MAX phases as Ti_3SiC_2 or Ti_4AlN_3 should be studied to check whether oxidation resistance can be tuned by incorporation of oxygen in the Al layer.

It is hoped that the extended rule of mixture will in the future be used for prediction of bulk moduli of nanolaminates or solid solutions thus avoiding extensive and time-consuming calculations of these. Thus, the extended rule of mixture may be used to investigate the bulk modulus in the framework of the materials genome project [161].

References

6 References

[1] http://www.rz.rwth-aachen.de/aw/cms/rz/Themen/hochleistungsrechnen/rechnersysteme/~oef/hpc_historie_im_rz/?lang=de. Center for Computing and Communication of RWTH Aachen University, accessed July 7 2012
[2] Jiang KY, Music D, Sarakinos K, Schneider JM. J. Phys.-Condes. Matter 2010;22:505502.
[3] Kolpin H, Music D, Laptyeva G, Ghadimi R, Merget F, Richter S, Mykhaylonka R, Mayer J, Schneider JM. J. Phys.-Condes. Matter 2009;21.
[4] Sarakinos K, Music D, Mraz S, Baben MT, Jiang K, Nahif F, Braun A, Zilkens C, Konstantinidis S, Renaux F, Cossement D, Munnik F, Schneider JM. J. Appl. Phys. 2010;108.
[5] Kolpin H, Music D, Henkelman G, Schneider JM. Phys. Rev. B 2008;78.
[6] Hostert C, Music D, Bednarcik J, Keckes J, Schneider JM. J. Phys.-Condes. Matter 2012;24.
[7] Emmerlich J, Music D, Houben A, Dronskowski R, Schneider JM. Phys. Rev. B 2007;76.
[8] Gebhardt T, Music D, Ekholm M, Abrikosov IA, von Appen J, Dronskowski R, Wagner D, Mayer J, Schneider JM. Acta Mater. 2011;59:1493.
[9] Gebhardt T, Music D, Kossmann D, Ekholm M, Abrikosov IA, Vitos L, Schneider JM. Acta Mater. 2011;59:3145.
[10] Linke BM, Music D, Emmerlich J, Schneider JM. Appl. Phys. Lett. 2011;99:231905.
[11] Music D, Basse FHU, Schneider JM. Crystal Growth & Design 2010;10:4531.
[12] Etsell TH, Flengas SN. Chemical Reviews 1970;70:339.
[13] Karimi A, Morstein M, Cselle T. Surf. Coat. Technol. 2010;204:2716.
[14] Sjölen J, Karlsson L, Braun S, Murdey R, Hörling A, Hultman L. Surface and Coatings Technology 2007;201:6392.
[15] Najafi H, Karimi A, Dessarzin P, Morstein M. Thin Solid Films 2011;520:1597.
[16] Gebhardt T, Music D, Takahashi T, Schneider JM. Thin Solid Films 2012;520:5491.
[17] Barsoum MW, Tzenov N, Procopio A, El-Raghy T, Ali M. J. Electrochem. Soc. 2001;148:C551.
[18] Rao JC, Pei YT, Yang HJ, Song GM, Li SB, De Hosson JTM. Acta Mater.;59:5216.
[19] Wang XH, Zhou YC. J. Mater. Res. 2002;17:2974.
[20] Wang XH, Zhou YC. Oxid. Met. 2003;59:303.
[21] Gupta S, Barsoum MW. J. Electrochem. Soc. 2004;151:D24.
[22] March NH. Advances in Physics 1957;6:1.
[23] Lieb EH. Reviews of Modern Physics 1981;53:603.
[24] Kohn W, Sham LJ. Physical Review 1965;140:1133.
[25] Cramer CJ, Truhlar DG. Physical Chemistry Chemical Physics 2009;11:10757.
[26] Perdew JP. In: Ziesche P, Eschrig H, editors. Electronic structure of solids '91. Berlin: Akademie Verlag, 1991. p.11.
[27] Kresse G, Joubert D. Phys. Rev. B 1999;59:1758.
[28] Monkhorst HJ, Pack JD. Phys. Rev. B 1976;13:5188.
[29] Blochl PE, Jepsen O, Andersen OK. Phys. Rev. B 1994;49:16223.
[30] Birch F. Journal of Geophysical Research 1978;83:1257.
[31] Henkelman G, Arnaldsson A, Jonsson H. Computational Materials Science 2006;36:354.
[32] Sanville E, Kenny SD, Smith R, Henkelman G. Journal of Computational Chemistry 2007;28:899.
[33] Liao T, Wang JY, Li MS, Zhou YC. J. Mater. Res. 2009;24:3190.
[34] Du YL, Sun ZM, Hashimoto H, Barsoum MW. J. Appl. Phys. 2011;109.

[35] Ramzan M, Lebegue S, Ahuja R. Physica Status Solidi-Rapid Research Letters 2011;5:122.
[36] Rohrbach A, Hafner J, Kresse G. Phys. Rev. B 2004;69.
[37] Schneider JM, Sigumonrong DP, Music D, Walter C, Emmerlich J, Iskandar R, Mayer J. Scripta Materialia 2007;57:1137.
[38] Schneider JM, Sun ZM, Mertens R, Uestel F, Ahuja R. Solid State Communications 2004;130:445.
[39] Vocadlo L, Poirer JP, Price GD. American Mineralogist 2000;85:390.
[40] Fast L, Wills JM, Johansson B, Eriksson O. Phys. Rev. B 1995;51:17431.
[41] Mayrhofer PH, Music D, Schneider JM. J. Appl. Phys. 2006;100:5.
[42] Zunger A, Wei SH, Ferreira LG, Bernard JE. Phys. Rev. Lett. 1990;65:353.
[43] Cowley JM. J. Appl. Phys. 1950;21:24.
[44] Abrikosov IA, Niklasson AMN, Simak SI, Johansson B, Ruban AV, Skriver HL. Phys. Rev. Lett. 1996;76:4203.
[45] Abrikosov IA, Simak SI, Johansson B, Ruban AV, Skriver HL. Phys. Rev. B 1997;56:9319.
[46] Oliver WC, Pharr GM. J. Mater. Res. 2004;19:3.
[47] Birkholz M. Thin Film Analysis by X-Ray Scattering. Weinheim: WILEY-VCH, 2006.
[48] Welzel U, Mittemeijer EJ. J. Appl. Phys. 2003;93:9001.
[49] Welzel U, Mittemeijer EJ. Z. Kristall. 2007;222:160.
[50] Wang JY, Zhou YC. Phys. Rev. B 2004;69.
[51] Sun ZM, Li S, Ahuja R, Schneider JM. Solid State Communications 2004;129:589.
[52] Jia GZ, Yang LJ. Physica B-Condensed Matter 2010;405:4561.
[53] Warren BE. X-ray Diffraction. New York: Dover Publications, 1990.
[54] Barsoum MW. Progress in Solid State Chemistry 2000;28:201.
[55] Music D, Schneider JM. Jom 2007;59:60.
[56] Barsoum MW, El-Raghy T. J. Am. Ceram. Soc. 1996;79:1953.
[57] Sigumonrong DP, Zhang J, Zhou Y, Music D, Schneider JM. Journal of Physics D-Applied Physics 2009;42.
[58] Hajas DE, to Baben M, Hallstedt B, Iskandar R, Mayer J, Schneider JM. Surface and Coatings Technology 2011;206:591.
[59] Lin ZJ, Li MS, Wang JY, Zhou YC. Acta Mater. 2007;55:6182.
[60] Wang XH, Zhou YC. Corr. Sci. 2003;45:891.
[61] Lee DB, Park SW. Oxid. Met. 2007;68:211.
[62] Tian WB, Wang PL, Kan YM, Zhang GJ. J. Mater. Sci. 2008;43:2785.
[63] Lee DB, Nguyen TD. J. Alloys Compd. 2008;464:434.
[64] Song GM, Pei YT, Sloof WG, Li SB, De Hosson JTM, van der Zwaag S. Scripta Materialia 2008;58:13.
[65] Yang HJ, Pei YT, Rao JC, De Hosson JTM, Li SB, Song GM. Scripta Materialia;65:135.
[66] Sigumonrong DP, Zhang J, Zhou YC, Music D, Emmerlich J, Mayer J, Schneider JM. Scripta Materialia 2011;64:347.
[67] Schneider JM, Anders A, Hjorvarsson B, Petrov I, Macak K, Helmersson U, Sundgren JE. Appl. Phys. Lett. 1999;74:200.
[68] Rosén J, Persson POA, Ionescu M, Kondyurin A, McKenzie DR, Bilek MMM. Appl. Phys. Lett. 2008;92:3.
[69] Persson POA, Rosén J, McKenzie DR, Bilek MMM. Phys. Rev. B 2009;80:4.
[70] Dahlqvist M, Alling B, Abrikosov IA, Rosén J. Phys. Rev. B 2010;81.
[71] Rosén J, Widenkvist E, Larsson K, Kreissig U, Mráz S, Martinez C, Music D, Schneider JM. Appl. Phys. Lett. 2006;88.
[72] Music D, Kolpin H, Baben MT, Schneider JM. Journal of the European Ceramic Society 2009;29:2885.

[73] Vegard L. Zeitschrift Fur Physik 1921;5:17.
[74] Mertens R, Sun ZM, Music D, Schneider JM. Advanced Engineering Materials 2004;6:903.
[75] Jeitschko W, Nowotny H, Benesovsky F. Monatshefte Fur Chemie 1963;94:672.
[76] Tian WB, Wang PL, Zhang GJ, Kan YM, Li YX, Yan DS. Scripta Materialia 2006;54:841.
[77] Barna PB, Adamik M. Thin Solid Films 1998;317:27.
[78] Pocza JF, Barna A, Barna PB. Journal of Vacuum Science & Technology 1969;6:472.
[79] Knacke O, Kubaschewski, O., Hesselmann, K. Thermochemical Properties of Inorganic Substances. Berlin: Springer, 1991.
[80] Münz WD. J. Vac. Sci. Technol. A-Vac. Surf. Films 1986;4:2717.
[81] McIntyre D, Greene JE, Håkansson G, Sundgren JE, Münz WD. J. Appl. Phys. 1990;67:1542.
[82] Rachbauer R, Massl S, Stergar E, Felfer P, Mayrhofer PH. Surface and Coatings Technology 2010;204:1811.
[83] Oettel H, Wiedemann R, Preissler S. Surface and Coatings Technology 1995;74-5:273.
[84] Bujak J, Walkowicz J, Kusinski J. Surface and Coatings Technology 2004;180:150.
[85] Zhou T, Nie P, Cai X, Chu PK. Vacuum 2009;83:1057.
[86] Alling B, Karimi A, Hultman L, Abrikosov IA. Appl. Phys. Lett. 2008;92:071903.
[87] Shew BY, Huang JL. Surface and Coatings Technology 1995;71:30.
[88] Adibi F, Petrov I, Greene JE, Hultman L, Sundgren JE. J. Appl. Phys. 1993;73:8580.
[89] Kimura A, Hasegawa H, Yamada K, Suzuki T. Surf. Coat. Technol. 1999;120:438.
[90] Håkansson G, Sundgren JE, McIntyre D, Greene JE, Münz WD. Thin Solid Films 1987;153:55.
[91] Mayrhofer PH, Hörling A, Karlsson L, Sjölen J, Larsson T, Mitterer C, Hultman L. Appl. Phys. Lett. 2003;83:2049.
[92] Reeswinkel T, Music D, Schneider JM. J. Phys.-Condes. Matter 2009;21:145404.
[93] Gassner G, Mayrhofer PH, Kutschej K, Mitterer C, Kathrein M. Surface and Coatings Technology 2006;201:3335.
[94] Erdemir A. Tribol. Lett. 2000;8:97.
[95] Luthier R, Levy F. J. Vac. Sci. Technol. A-Vac. Surf. Films 1991;9:102.
[96] Tönshoff K, Karpuschewski B, Mohlfeld A, Leyendecker T, Erkens G, Fuss HG, Wenke R. Surface and Coatings Technology 1998;108:535.
[97] Kawata K, Sugimura H, Takai O. Thin Solid Films 2001;390:64.
[98] Fabreguette F, Imhoff L, Guillot J, Domenichini B, de Lucas MC, Sibillot P, Bourgeois S, Sacilotti M. Surface and Coatings Technology 2000;125:396.
[99] Guillot J, Jouaiti A, Imhoff L, Domenichini B, Heintz O, Zerkout S, Mosser A, Bourgeois S. Surf. Interface Anal. 2002;33:577.
[100] Graciani J, Hamad S, Sanz JF. Phys. Rev. B 2009;80:184112.
[101] Porter DA, Easterling KE, Sherif MY. Phase Transformations in Metals and Alloys: CRC Press, 2009.
[102] Kittel C. Introduction to Solid State Physics: Wiley, 2005.
[103] Tsetseris L, Kalfagiannis N, Logothetidis S, Pantelides ST. Phys. Rev. B 2008;78:094111.
[104] Sugiyama K, Takeuchi Y. Z. Kristall. 1991;194:305.
[105] Mayrhofer PH, Mitterer C, Hultman L, Clemens H. Prog. Mater. Sci. 2006;51:1032.
[106] Cahn JW. Acta Metall. 1962;10:789.
[107] Hyett G, Parkin IP. Surf. Coat. Technol. 2007;201:8966.
[108] Hyett G, Green MA, Parkin IP. Journal of the American Chemical Society 2007;129:15541.
[109] Kafizas A, Hyett G, Parkin IP. Journal of Materials Chemistry 2009;19:1399.
[110] Kafizas A, Parkin IP. Journal of the American Chemical Society 2011;133:20458.

[111] Van Zon J, Rijpers JCN. J. Vac. Sci. Technol. A-Vac. Surf. Films 1989;7:144.
[112] Vossen JL, Krommenhoek S, Koss VA. J. Vac. Sci. Technol. A-Vac. Surf. Films 1991;9:600.
[113] Niwa T, Saito T, Kinbara A. J. Vac. Sci. Technol. A-Vac. Surf. Films 1993;11:2790.
[114] Roquiny P, Bodart F, Terwagne G. Surf. Coat. Technol. 1999;116:278.
[115] Deniz D, Harper JME. J. Appl. Phys. 2008;104.
[116] Zhao ZB, Rek ZU, Yalisove SM, Bilello JC. Surf. Coat. Technol. 2004;185:329.
[117] Audronis M, Matthews A, Leyland A. Journal of Physics D-Applied Physics 2008;41:10.
[118] Pedersen K, Bottiger J, Sridharan M, Sillassen M, Eklund P. Thin Solid Films 2010;518:4294.
[119] Zhang S, Sun D, Fu YQ, Du HJ. Surf. Coat. Technol. 2003;167:113.
[120] Riedel R. Advanced Materials 1994;6:549.
[121] Falter C, Zierau W. J. Appl. Phys. 1980;51:2070.
[122] Fine ME, Brown LD, Marcus HL. Scripta Metallurgica 1984;18:951.
[123] Narain S. Physica Status Solidi B-Basic Research 1994;182:273.
[124] Cohen ML. Phys. Rev. B 1985;32:7988.
[125] Zhang S, Li H, Li H, Zhou S, Cao X. Journal of Physical Chemistry B 2007;111:1304.
[126] Kumar V, Prasad GM, Chetal AR, Chandra D. Journal of Physics and Chemistry of Solids 1996;57:503.
[127] Eriksson O. Electronic structure calculations of phase stability: cohesive and elastic properties. Encyclopedia of Materials: Science and technology. Elsevier, 2006. p.1.
[128] Music D, Sun ZM, Ahuja R, Schneider JM. Phys. Rev. B 2006;73.
[129] Kooi BJ, Poppen RJ, Carvalho NJM, De Hosson JTM, Barsoum MW. Acta Mater. 2003;51:2859.
[130] Sun ZM, Music D, Ahuja R, Schneider JM. Phys. Rev. B 2005;71.
[131] Fang CM, Ahuja R, Eriksson O, Li S, Jansson U, Wilhelmsson O, Hultman L. Phys. Rev. B 2006;74.
[132] He LF, Lin ZJ, Wang JY, Bao YW, Zhou YC. Scripta Materialia 2008;58:679.
[133] Liao T, Wang J, Zhou Y. Phys. Rev. B 2006;74.
[134] Jones LH, Penneman RA. Journal of Chemical Physics 1954;22:965.
[135] Jakubinek MB, Samarasekera CJ, White MA. J. Mater. Res. 2006;21:287.
[136] Li GQ, Zhao Y, Pang SS, Li YQ. Cement and Concrete Research 1999;29:1455.
[137] Chawla KK. Composite Materials: Science and Engineering. New York: Springer, 2011.
[138] Kim JO, Achenbach JD, Mirkarimi PB, Barnett SA. Phys. Rev. B 1993;48:1726.
[139] Bao WX, Zhu CC, Cui WZ. Physica B-Condensed Matter 2004;352:156.
[140] Hernandez E, Goze C, Bernier P, Rubio A. Phys. Rev. Lett. 1998;80:4502.
[141] Music D, Sun ZM, Schneider JM. Solid State Communications 2005;133:381.
[142] Isaev EI, Simak SI, Abrikosov IA, Ahuja R, Vekilov YK, Katsnelson MI, Lichtenstein AI, Johansson B. J. Appl. Phys. 2007;101.
[143] Cover MF, Warschkow O, Bilek MMM, McKenize DR. J. Phys.-Condes. Matter 2009;21.
[144] Cover MF, Warschkow O, Bilek MMM, McKenzie DR. Advanced Engineering Materials 2008;10:935.
[145] Du YL, Sun ZM, Hashimoto H, Tian WB. Physica Status Solidi B-Basic Solid State Physics 2009;246:1039.
[146] Music D, Schneider JM. J. Phys.-Condes. Matter 2008;20.
[147] Music D, Emmerlich J, Schneider JM. J. Phys.-Condes. Matter 2007;19.
[148] Hug G. Phys. Rev. B 2006;74.

[149] Palmquist JP, Li S, Persson POA, Emmerlich J, Wilhelmsson O, Hogberg H, Katsnelson MI, Johansson B, Ahuja R, Eriksson O, Hultman L, Jansson U. Phys. Rev. B 2004;70.
[150] Sun ZM, Music D, Ahuja R, Li S, Schneider JM. Phys. Rev. B 2004;70:092102.
[151] Sun ZM, Music D, Ahuja R, Schneider JM. J. Phys.-Condes. Matter 2005;17:7169.
[152] He XD, Bai YL, Zhu CC, Sun Y, Li MW, Barsoum MW. Computational Materials Science 2010;49:691.
[153] Wang JY, Wang JM, Zhou YC, Lin ZJ, Hu CF. Scripta Materialia 2008;58:1043.
[154] Sun ZM, Ahuja R, Schneider JM. Phys. Rev. B 2003;68.
[155] Johnson LJS, Thuvander M, Stiller K, Oden M, Hultman L. Thin Solid Films 2012;520:4362.
[156] Rachbauer R, Stergar E, Massl S, Moser M, Mayrhofer PH. Scripta Materialia 2009;61:725.
[157] Hans M. Effect of oxygen on structure, mechanical properties and stability of the material system Ti-Al-N-O, Bachelor of Science Thesis (2011);Materials Chemistry, RWTH Aachen University, supervised by to Baben M.
[158] Music D, Schneider JM. J. Phys.-Condes. Matter 2008;20.
[159] Hostert C, Music D, Bednarcik J, Keckes J, Kapaklis V, Hjorvarsson B, Schneider JM. J. Phys.-Condes. Matter 2011;23.
[160] Gall D, Kodambaka S, Wall MA, Petrov I, Greene JE. J. Appl. Phys. 2003;93:9086.
[161] www.whitehouse.gov/mgi. The White House, accessed January 6 2013

Lebenslauf Moritz to Baben

Persönliche Angaben:

Geburtsdatum	10.02.1984
Geburtsort	Eutin
Nationalität	deutsch
Adresse	Templergraben 52, 52062 Aachen

Ausbildung:

Seit 11/2007	Doktorand am Lehrstuhl für Werkstoffchemie, RWTH Aachen
10/2007	Abschluss als Diplom-Ingenieur (Note 1,6)
10/2003 - 10/2007	Studium Metallurgie und Werkstofftechnik, RWTH Aachen
06/2003	Abitur (Note 1,8), St. Ursula Gymnasium, Brühl

Auszeichnungen und Stipendien:

09/2012	Best-Paper-Award des Forums Materialwissenschaft und Werkstofftechnik an der RWTH Aachen
04/2012	Graduate Student Award in Bronze der International Conference on Metallurgical Coatings and Thin Films (ICMCTF)
07/2008 - 06/2011	Promotionsstipendium der RWTÜV-Stiftung mit dem Titel “Nanolaminate für die Energieumwandlung mit erhöhtem Wirkungsgrad”
11/2008	Otto Junker Preis für hervorragende Studienleistungen

Lehre:

Seit 2011	Leitung des Praktikums Werkstoffchemie I
2007 - 2011	Übungsleitung Werkstoffchemie II
2006 - 2011	Betreuung im Praktikum Werkstoffchemie I

Engagement:

06/2010	Teilnahme an der Summer School “Responsible Engineering in a Warming World“ an der TU Delft und der Konferenz “Ethics, Energy and the Future; Technology for a Sustainable Society’” in Delft
08/2009	Teilnahme an der Summer School “Responsibility and Engineers of the Future” an der TU Delft
Seit 2008	Beisitzer im SPD Ortsverein Aachen-Mitte und der Arbeitsgemeinschaft für Bildungsfragen
11/2005 - 06/2007	Ehrenamtliche Hausaufgabenbetreuung in der Kindertagesstätte Rokoko, Aachen, im Rahmen vom Projekt „Studis helfen Kids“